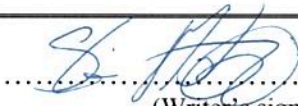




University of
Stavanger

Faculty of Science and Technology

MASTER'S THESIS

Study program/ Specialization: Petroleum Technology / Reservoir Engineering	Spring semester, 2011 <u>Open</u> / Restricted access
Writer: Stian Molvik	 (Writer's signature)
Faculty supervisor: Steinar Evje External supervisor(s): -	
Title of thesis: A Study of Two-Phase Drift-Flux Modeling in Wells and Corresponding Slip Relations	
Credits (ECTS): 30	
Key words: Drift-flux, slip, vertical, two-phase, hyperbolic, transient, steady-state, counter- current, mixed-momentum, mass conservation, dissipation, flux splitting, FVS, AUSMV, Taylor-bubble, slug flow.	Pages: 67 + enclosure: 17 Stavanger, 14.06.2011 Date/year

A Study of Two-Phase Drift-Flux Modeling in Wells and Corresponding Slip Relations

Stian Molvik

14.06.2011

A Thesis
Submitted to the Department of
Petroleum Engineering
of University of Stavanger
in Fulfillment of the Requirements
for the Degree of
Master of Science



Abstract

It was desired to investigate the two-phase drift-flux model's behavior in both steady-state and transient settings and shed some light on required slip relations. A numerical MATLAB model of the one-dimensional two-phase drift-flux model developed by Dr. Steinar Evje has been used to simulate gas-liquid flow in a vertical pipe. Different slip parameters have been tested, compliant with the general formulation from Zuber and Findlay [22]. Optimized slip parameters from Shi et al. [15] have been implemented in the numerical model, and simulation runs for both steady-state and transient conditions are included. Ten steady-state simulations have been carried out, matching the experimental holdup data very well with a root-mean square error of only 0.039.

The optimized slip parameters have then been directly applied in a transient setting, in which a 17.8 dm³ slug is put at the bottom of a 10.9 m, 15.24 cm diameter pipe and allowed to migrate towards the closed outlet, similar to what would happen in a kicking well. It is observed that the optimized slip is not able to reproduce the typical Taylor bubble flow expected to occur in such a setting, as the gas distribution of the slug was seen to spread over the length of the pipe. As the gas is seen to accumulate at top, unphysical behavior is observed, and it is believed that the slip model from Shi et al. causes the drift-flux model failing to remain hyperbolic. This has given way for a desire to implement different slip parameters able to reproduce more typical Taylor-bubble behavior.

Basic slip parameters for slug flow and parameters for Taylor bubbles from Hibiki and Ishii [6] have been implemented. Although the complexity of the Taylor bubble slip far outweighs that of the simple slug flow slip, the results were found to be in good agreement with each other with regards to gas distribution in the pipe. The slug flow slip was able to let the gas slug maintain a maximum average gas volume fraction of a $\alpha_{g,max} \approx 0.79$, while the Taylor bubble slip gave a respectable average gas fraction of $\alpha_{g,max} \approx 0.82$. Also, the Taylor-bubble-slip proved to increase the overall rise velocity of the slug, allowing it to traverse the pipe at a somewhat higher velocity than when using slug flow slip

Acknowledgments

I would like to extend my sincere gratitude to my supervisor Steinar Evje for his dedication and support throughout writing this thesis. Many hours were spent in his office discussing heavily on my reported findings. Gratitude is also extended to previous professors of mine, Paul Papatzacos and Rune Time, for shedding light on certain problems when in times of need. Gratitude is also extended to the University of Stavanger for allowing me to make use of their Unix workstations when conducting numerical simulations. I am also grateful for my great friend and fellow student, Harald Litlehamar, for providing a different perspective when hardships were encountered.

A key motivational aspect for me, electing to write a thesis on the drift-flux model, was to get a better understanding of the mathematics behind such a model as well as being able to better utilize MATLAB in a future working environment. As I prior to this assignment had little or no experience with the software from before, I saw this as a challenge I would gladly take on. In retrospect, much of my time spent agonizing when MATLAB would not output the results I was after, or when documents were not compiling correctly in L^AT_EX, have made me much more competent using both of these as scientific tools. Thanks are also given to my loving girlfriend Karema and our French bulldog, Mozart.

Thank you.

Contents

I	Overview	1
1	Introduction	1
2	Application	2
3	Multiphase Flow Concepts	2
4	General Slip Law	3
5	Vertical Two-Phase Flow	4
5.1	Dispersed Bubble Flow	4
5.2	Slug Flow	5
5.3	Churn Flow	5
5.4	Annular Flow	5
II	Flow Model	5
6	Conservation Laws	6
6.1	Conservation of Mass	6
6.2	Conservation of Momentum	7
7	Drift-Flux Model	8
7.1	Introduction	8
7.2	General	9
7.3	Hyperbolicity	10
7.3.1	Hyperbolicity With No-Slip Conditions	11
7.3.2	Computing Flux Terms from Conserved Variables	16
8	Numerical Schemes	17
8.1	Flux Splitting	18
8.2	FVS	19
8.2.1	Convective Flux	19
8.2.2	Pressure Flux	20
8.3	AUSMV	21
8.4	Dissipation for Different Schemes at Contact Discontinuities	22
8.4.1	FVS	22
8.4.2	AUSMV	22
8.4.3	Discontinuity Case	23
III	Numerical Model Simulations	25

9	Matlab Model	25
9.1	Work Flow	25
9.2	Grid	26
10	Shi Slip Relation	27
10.1	General	27
10.2	Sensitivity Analysis	29
10.3	Steady State Simulations	31
10.3.1	Steady State Boundary Conditions	33
10.3.2	Simulation Run	34
11	Transient Simulations	41
11.1	Short Pipe	41
12	Transient Simulations with Simple Slip	41
13	Transient Simulations with SHI Slip	45
13.1	Objective Function	49
13.2	Simulation Node Comparison	50
13.3	Long Pipe	51
13.4	Slip Describing Taylor Bubble Flow	52
13.4.1	Slug Flow Slip	53
13.4.2	Taylor Bubble Slip	54
14	Conclusions and Further Work	56
	Nomenclature	57
	References	61
A	MATLAB Model Files	63
A.1	SHIslip2.m	63
A.2	customslip2.m	65
A.3	vsplit_plot.m	66
A.4	vsplit_chi.m	67
A.5	sound_velocity.m	68
A.6	c1_c2.m	70
A.7	holdup_results.m	71
A.8	SHI_c1_c2_ex.m	73
A.9	SHIslip2_sens.m	76
A.10	p_u1_u2.m	78

Part I

Overview

1 Introduction

The motivation behind electing to write a thesis on the one-dimensional drift-flux model, lies within the many ways fluid models are useful in petroleum engineering contexts. Being able to model multiphase flows in a wellbore is of great importance in the petroleum industry as it allows for a better management and interaction between the reservoir and the well bore. As a reservoir simulator might give a good estimation of what volume rates of reservoir fluid the reservoir can deliver, this does not translate directly to the well being able to produce an equivalent rate. Without a fluid model in place, describing effects that may arise within a well bore over time to impair or improve production are immensely difficult. Two-phase models are also extremely viable in drilling processes.

The fluid model this thesis will focus on is the one-dimensional two-phase drift-flux model, its use in computational fluid dynamics and its behavior when implementing different slip parameters. Slip parameters are used to allow the phases to flow at unequal phase velocities, and is a requirement due to the drift-flux model consisting of a single mixed-momentum equation. Some of the more intricate slip relations that are to be implemented have been presented in [15, 6]. A numerical MATLAB model developed by Dr. Steinar Evje provides a numerical solution of the drift-flux model, and it is this model that is to be used in steady state- and transient simulations to come. The underlying constituents of the model, namely the mass- and momentum conservation equations, are to be derived on non-conservative form so the average reader can have a better understanding of the model. Energy conservation however is not to be considered as iso-thermal conditions are assumed throughout. When the conservation equations are discretized and applied in the numerical model, splitting of the fluxes is a necessity, and FVS (flux vector splitting) and AUSMV (advective upwind splitting method) is presented. It is to be shown why AUSMV is far superior with regards to dissipation over discontinuities in fluid fractions when compared with FVS, and as such it is AUSMV that is used within the numerical model. The set of equations making up the drift-flux model is to be shown to be hyperbolic in the case of no-slip flowing conditions, thus the solution of the system will propagate at finite velocities.

It is desired to shed some light on how different slip relations affect the numerical solution, what restrictions apply and what instability issues occur. Sub-routines need to be added to the MATLAB model to allow for the effect of different slip relations being modeled. The slip model presented in [15, 16] is in fact the same slip used within the multi-segment well module within the Eclipse Reservoir Simulator, where it has been dubbed “drift-flux slip”. Steady-state simulations are to be matched with experimental data from [15] to better validate the slip model, before applying it in transient gas migration simulations.

The sole purpose of Part I is to develop a general outline for further reading. At first, a section describing some of the applicable areas fluid models can have in a petroleum engineering contexts is included, where it is to be emphasized some of the useful settings in which such models are deemed viable tools. In the following section, basic terms related to multiphase flow are to be declared with basis in the general slip formulation. This is done to better familiarize the reader with the slip, as well as easing him/her into elementary concepts related to multiphase flow. A section dedicated to the slip law is then included, where it is emphasized some properties the slip parameter will have to exhibit. Lastly some of the most common flow patterns encountered in vertical flow are to be presented as well as some conditions that may lead to the transition from one flow pattern to another.

In Part II the mass- and momentum equations on non-conservative flow are to be derived. This is done to allow for a better understanding of the foundation of the subsequent drift-flux model. The model itself is then introduced, and some mathematical derivations are to be included to highlight some of the properties within the model. A section describing flux splitting techniques is then included, and a mathematical derivation on dissipation is included to show how the AUSMV scheme will outperform the FVS scheme.

Part III will include all the simulation results in this thesis. It is to be shown how the numerical model operates before an entire section dedicated to giving an overview of the slip parameters from [15] is included. Steady state simulations with the new set of slip parameters are to be carried out before transient simulations with this and a simpler slip are compared. Conclusions will seek to follow, along with an Appendix incorporating some of the developed MATLAB model files that have been used.

2 Application

A good example of a multiphase flow model being paired with a reservoir simulator is the Multi-Segment-Well module being implemented in Eclipse reservoir simulator. See [7, 14, 13]. This allows for better determination of the pressure distribution within the well, as hydrostatic- frictional- and accelerational pressure drops are all accounted for. Having a multiphase flow model in place makes it also possible to model effects such as phase segregation within slow moving fluids of different densities as well as cross-flow of production from one perforation to another. Better estimation of production rates and optimization scenarios are only some of the benefits reaped. For more information on the Multi-Segment-Well module within Eclipse look for keywords WSEGFMOD and WSEGDFMD within [13, 14].

In the drilling phase of a new well it is also important to be able to accurately predict pressure distribution in the well and ultimately the downhole pressure. This means better control of the downhole pressure when drilling formation sections where the pore pressure gradient is close to the fracturing pressure gradient. A fluid model in place which in real-time is fed the wellhead pressure as well as the pump rate of mud would be able to continuously determine the pressure gradient in the well.

When designing a well, two-phase fluid models can be used to estimate worst case scenarios with regards to pressure distribution, i.e pressure in gas kick situations at casing shoe, and thus allow for better determination of what material strength is required. As most manual calculations of such conditions will tend to over-estimate the pressures, it can be quite cost effective having better control of what realistic conditions may occur.

3 Multiphase Flow Concepts

The drift-flux model is appreciated for its relative simplicity as well as its ability to model fluids traveling at different velocities (the slip). It is therefore also capable of modeling counter-current flow which would be present when fluids of different densities are moving slowly, i.e in a gas kick situation during drilling or phase-segregation during shut-in.

Instead of heading straight into the more theoretical aspects of the model, it seems necessary to define some of the basic concepts related to multiphase flow. A key element making up the drift-flux model, namely the slip, is now to be presented to allow for further explanations of terms related to it

and multiphase flow in general. The general slip law that is used throughout this thesis was introduced by Zuber & Findlay in [22] and takes the following form

$$v_g = C_o v_m + v_d, \quad (1)$$

where v_g is the gas velocity and v_m the mixture velocity. Parameters C_o and v_d are slip parameters defining the difference in velocity between the involved fluids. It is these parameters effect on the numerical model that will be further analyzed in sections to come. The real velocity of the gas, v_g , often referred to as the phase velocity, is defined by

$$v_g = \frac{Q_g}{A_g}$$

with Q_g being the volume rate of gas and A_g the pipe crosssectional area of the pipe available for gas to flow in. This area will in multiphase flow settings be smaller than total area A due to other fluids occupying some of the same cross-sectional pipe area. Mixture velocity v_m is defined as a sum of superficial velocities

$$v_m = v_{gs} + v_{ls}$$

in which the v_{gs} and v_{ls} are the velocities each corresponding fluid would have if all of the pipe crosssectional area were available for the fluids to flow in. This means that $v_{gs} = \frac{Q_g}{A}$ and $v_{ls} = \frac{Q_l}{A}$ and as such the relation between superficial and phase velocities are had to be

$$v_{gs} = \alpha_g v_g, \quad v_{ls} = \alpha_l v_l \quad (2)$$

with $\alpha_g = \frac{A_g}{A}$ and $\alpha_l = \frac{A_l}{A}$. The condition of $\alpha_g + \alpha_l = 1$ follows naturally.

Remark. It is important to note that all velocity terms derived in this section are in fact cross-sectional averages and should be treated as such. They are therefore ideally suited to be used in one-dimensional fluid models.

4 General Slip Law

In the general slip formulation of [22], slip is described as a function of two mechanisms. One mechanism is a direct result of the local mixture concentration being larger in the center of the pipe than at the walls, thus making the gas concentration greater at the center. Integrating the gas velocity over the pipe area gives a higher average velocity for the gas than for the liquid. The other mechanism is a result of gas being the lighter of the two in a gas-liquid mixture, giving the gas an extra velocity due to buoyancy.

A formulation for slip combining both of these effects is given in equation (1) for gas-liquid flow with liquid being the continuous phase. Figure 4.1 illustrates the elements making up the general slip relation in which the velocity profile is related to v_m and the gas concentration profile is related to C_o . The local relative velocity is the added velocity of the gas when compared with the surrounding fluid, namely the drift velocity v_d .

Concentration profile parameter C_o will tend to be dependent on the reigning flow pattern within the pipe. For high mixture velocities, fluid mixtures tend to become more and more homogeneous. This causes the concentration profile from Figure 4.1 to flatten out as phases are more evenly distributed in an area cross-section of the pipe and thus C_o approaches unity for a homogeneous mixture whereas there will be no slip between the phases.

Correspondingly to coincide with no-slip conditions for homogeneous mixtures, v_d must reduce to zero as C_o approaches unity. This is evident when looking at the the general slip formulation of 1.

The slip parameters originally introduced in [22] are for small diameter pipes, are not sufficient to effectively describe multiphase flow in pipes of larger diameter, as would be desirable in a petroleum engineering context. In recent years, experiments with multiphase flow in larger diameter pipes have been performed, and it is of interest to see what impact slip parameters based on these will have in a numerical solution of the drift-flux model.

Such experiments have been performed in [10] and [15]. This paper will use the latter as an evaluation point when evaluating and implementing slip relations into the numerical drift-flux model. The experiments make use of a 15.24 cm diameter pipe of 10.9 m in length when estimating slip parameters for water-gas, oil-water and oil-water-gas flow.

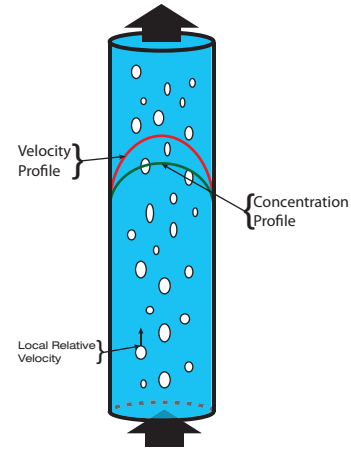


Figure 4.1: Pipe cross-section indicating velocity profile for the mixture and concentration profile for the gas. Drawn using Adobe Illustrator CS5.

5 Vertical Two-Phase Flow

Vertical two-phase flows are seen to exhibit very different flow patterns depending on the reigning flowing conditions. This causes the fluid distribution within the pipe to vary significantly, which then can cause major differences with regards to pressures and transport of fluids (heat transfer is also of concern, but will not be further discussed throughout this thesis as iso-thermal conditions are already assumed).

From the literature, vertical two-phase flow patterns for gas-liquid flows can in general be divided into four or five different flow regimes. Dispersed bubble-, slug-, churn- and annular flow (wispy annular). I.e see [1]. The most common vertical flow patterns are illustrated in Figure 5.1. What flow regimes are encountered can be seen to depend on the velocity and volume fraction of the phases present. As such, superficial velocities are generally used in predicting what flow pattern can be expected. For instance see [18] where flow regime maps consists of v_{gs} plotted against v_{ls} on log-log scale depicting the transition between respective flow patterns.

5.1 Dispersed Bubble Flow

Dispersed bubble flow is quantitatively viewed as gas bubbles being homogeneously distributed within a pipe cross-sectional area, with liquid being the continuous phase and gas appearing as bubbles of varying diameter and shape. This flow pattern is mostly present when the gas volume fraction is low, as for high gas volume fractions the bubbles will tend to coalesce and form slug bubbles, also known as Taylor bubbles. When the flow velocity is somewhat higher, turbulent flowing conditions will tend to break bubbles apart causing the dispersed flow regime to be present for even higher volume fractions of gas.

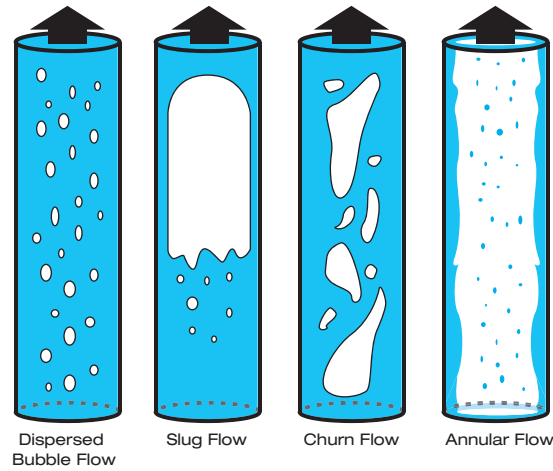


Figure 5.1: Flow patterns occurring in vertical two-phase flow. Drawn using Adobe Illustrator CS5.

5.2 Slug Flow

Slug flow is a result of even higher gas volume rates, increasing the contact frequency of the bubbles, causing them to coalesce and eventually form larger bubbles of diameter size equivalent to pipe diameter. See Figure 5.1 for an illustration of such a slug bubble. These bubbles are often referred to as Taylor bubbles and will tend to have shapes similar to that of bullets. As they are so large in diameter, they will to a larger extent be affected by the wall friction within the pipe and thus move at a lower velocity than bubbles of smaller size. Smaller bubbles will then catch up and coalesce with the Taylor bubble in front of it. When the Taylor bubble moves upwards, it forces a thin liquid film to flow downwards around it. Slug flow appears as alternating sections of slug bubbles and pure liquid regions.

5.3 Churn Flow

Churn flow occurs when velocity is so high that turbulent forces tend to break the slug bubbles apart. This makes it out to be a very chaotic flow pattern to effectively describe.

5.4 Annular Flow

When sufficient amounts of gas is present and gas velocity becomes high enough to push liquid onto the pipe wall without it falling back onto the gas, the annular flow regime is initiated. Differences in phase velocities are often seen to be very high in annular flow.

Part II

Flow Model

6 Conservation Laws

The flow models described in this paper all make use of the conservation laws for mass and momentum. Energy conservation is not to be considered, as iso-thermal conditions are assumed throughout. Section 6.1 and 6.2 are included in this paper to give the reader an opportunity to familiarize himself with the basic conservation laws used in describing fluids in motion. This will thus hopefully allow for a better understanding of the subsequent drift-flux model. For more on the derivation of the conservation equations, see [11].

After the drift-flux model is sufficiently described, a section dedicated to the numerical scheme of it is included. This section will describe some of the elementary discretization being used as well as techniques used in splitting the fluxes of the system.

6.1 Conservation of Mass

For a single-phase fluid where mass is to be conserved, it is known that net-change in mass within a control volume $V(t)$ equals what is added/subtracted from said volume. For such a system, the following relation for mass conservation must hold

$$\frac{d}{dt} \int_{V(t)} \rho(\mathbf{x}, t) dV = \int_{V(t)} \Gamma(\mathbf{x}, t) dV, \quad (3)$$

where $V(t)$ is an arbitrarily chosen volume, $\rho(\mathbf{x}, t)$ is the density of the fluid, $\Gamma(\mathbf{x}, t)$ is the change in mass over time per unit volume (source/sink term) and $\mathbf{x} = \mathbf{x}(x_1, \dots, x_n)$ is a spatial vector. With respect to the drift-flux model, it is deemed convenient to derive the mass conservation equation in non-conservative form. In order to accomplish this it is necessary to introduce Reynold's Transport Theorem.

Theorem 1 (Reynolds Transport Theorem). *For a medium in motion with a control volume $V(t)$ and corresponding control surface $S(t)$ following the movement of fluid particles, for an arbitrary property of the fluid $N(\mathbf{x}, t)$ that*

$$\frac{d}{dt} \int_{V(t)} N(\mathbf{x}, t) dV = \int_{V(t)} [\partial_t N + \nabla \cdot (N\mathbf{v})] dV$$

with $\mathbf{v}(\mathbf{x}, t)$ being the velocity field of the fluid.

Making use of Theorem 1 with equation (3), it can be rewritten

$$\int_{V(t)} [\partial_t \rho + \nabla \cdot (\rho\mathbf{v}) - \Gamma] dV = 0 \quad (4)$$

The last part in deriving the commonly known equation of mass conservation on non-conservative form is making use of the Du Bois-Reymond Lemma from.

Lemma (Du Bois-Reymond Lemma). *Assume a space V with n dimensions and a continuous function $f(x)$ where the spatial vector \mathbf{x} has components x_1, x_2, \dots, x_n . If D is an arbitrary region in V and if*

$$\int_D f(x) d^n x = 0$$

then $f(x) \equiv 0$.

Applying the Du Bois-Reymond lemma with eq. (4), the conventional equation of mass conservation in three dimensions is given

$$\partial_t \rho + \nabla \cdot (\rho \mathbf{v}) = \Gamma. \quad (5)$$

For a one-dimensional model, equation (5) translates to

$$\partial_t \rho + \partial_x (\rho v) = \Gamma.$$

Remark. If all mass is conserved, i.e no mass is to be added/subtracted from the system, then $\Gamma = 0$. For a system consisting of several mass conservation equations Γ will typically represent the transfer of mass from one phase to another, analogous to what would happen in most oil and gas flows.

6.2 Conservation of Momentum

The basis in deriving the equation of momentum conservation is applying Newton's second law of motion on a fluid element. For a volume segment dV within a control volume $V(t)$ with surrounding control surface $S(t)$ the following force balance holds in the i' th direction¹

$$\frac{d}{dt} \int_{V(t)} \rho v_{i'} dV = \int_{V(t)} f_{i'} dV + \int_{S(t)} t_{i'} dS, \quad i' = 1, \dots, k \quad (6)$$

where it is stated that the net change in momentum within a control volume equals the sum of volume- and surface forces acted upon said volume. Parameter $f_{i'}$ is the volume force per unit volume and $t_{i'}$ is the stress vector (surface tension). In order to transform the surface integral on the RHS of (6) to a volume integral, it is first necessary to introduce Cauchy's Theorem to redefine the stress vector. See [17].

Theorem 2 (Cauchy's Stress Theorem). *If the stress vectors acting across three mutually perpendicular planes at any given point are known, then all stress vectors at that point can be determined by equation*

$$\mathbf{t} = \boldsymbol{\sigma} \cdot \hat{\mathbf{n}}.$$

¹Index i' is not to be confused with the node coordinate i that is introduced in Section 8.

The surface tension can then be expressed in tensor form by $t_{i'} = n_j \sigma_{ji'}$ where n_j is the unit normal vector and $\sigma_{ji'}$ the stress tensor. The tensor notation used is that $\mathbf{a} \cdot \mathbf{b} = a_{i'} b_{i'}$ where an index appearing twice in the same term indicates it should be summed over, i.e $n_j \sigma_{ji'} = n_1 \sigma_{1j} + \dots + n_k \sigma_{kj}$ with $i' = 1, \dots, k$. Both i' and j will be used to indicate directions in space. Equation 6 can now be written

$$\frac{d}{dt} \int_{V(t)} \rho v_{i'} dV = \int_{V(t)} f_{i'} dV + \int_{S(t)} n_j \sigma_{ji'} dS, \quad j, i' = 1, \dots, k. \quad (7)$$

Applying Reynolds transport theorem to LHS of equation (7), where notation is that $\nabla \cdot (N\mathbf{v}) = \partial_j (Nv_j)$, it can be written

$$\int_{V(t)} [\partial_t (\rho v_{i'}) + \partial_j (\rho v_{i'} v_j)] dV = \int_{V(t)} f_{i'} dV + \int_{S(t)} n_j \sigma_{ji'} dS \quad j, i' = 1, \dots, k. \quad (8)$$

All that now is left is transforming the surface integral on the LHS of equation (8) to a volume integral by making use of the divergence theorem.

Theorem 3 (Divergence Theorem). *If \mathbf{N} is continuously differentiable vector field within a finite volume V in \mathbb{R}^3 , with a piecewise smooth outer boundary S then*

$$\int_{S(t)} \mathbf{N} \cdot \hat{\mathbf{n}} dS = \int_{V(t)} \nabla \cdot \mathbf{N} dV$$

or in tensor notation

$$\int_{S(t)} N_j n_j dS = \int_{V(t)} \partial_j N_j dV, \quad j = 1, 2, 3.$$

Applying the divergence theorem to the surface integral of equation 8 and adding the volume integrals, it is now written

$$\int_{V(t)} [\partial_t (\rho v_{i'}) + \partial_j (\rho v_{i'} v_j) - f_{i'} - \partial_j \sigma_{ji'}] dV = 0 \quad j, i' = 1, 2, 3'.$$

The final part in concluding with the conservation of momentum on non-conservative form is applying the du Bois-Reymond lemma so that

$$\partial_t (\rho v_i) + \partial_j (\rho v_i v_j - \sigma_{ji'}) = f_{i'} \quad j, i' = 1, 2, 3. \quad (9)$$

For a one-dimensional application, equation (9) reduces to

$$\partial_t (\rho v) + \partial_x (\rho v^2 - \sigma) = f.$$

7 Drift-Flux Model

7.1 Introduction

For describing multiphase flow in pipes in a petroleum engineering context, either empirical correlations, mechanistic models or homogeneous models are most commonly used. This thesis will focus on the latter.

While mechanistic models incorporate a range of different slip relations as well as corresponding fluid models based on which flow regime is predicted to be present, homogeneous models assume the properties of fluids involved can be represented by mixture properties, thus making the mixture susceptible to single-phase flow techniques. In these models a slip can be forced onto the phases, allowing phases to flow at different velocities. Homogeneous models which account for slip are also known as drift-flux models. See [15].

Some of the main advantages of drift-flux models are that they are simple, continuous and differentiable, making them ideal candidates to be used in simulators. It is also noted that the drift-flux model is best suited representing flow in the bubble- or slug flow regime. Based on what numerical scheme is used within the model, it should be able to handle the transition from single-phase to two-phase flow as well as the transition from co-current to counter-current flows.

7.2 General

Drift-flux models are simple yet powerful models which accounts for the difference in velocities between the phases flowing. For an isothermal system with no mass transfer between the phases, the one-dimensional drift-flux model is made up of mass balance equations for each phase and a combined momentum equation for the mixture

$$\begin{aligned}\partial_t (\alpha_l \rho_l) + \partial_x (\alpha_l \rho_l v_l) &= 0, \\ \partial_t (\alpha_g \rho_g) + \partial_x (\alpha_g \rho_g v_g) &= 0, \\ \partial_t (\alpha_l \rho_l v_l + \alpha_g \rho_g v_g) + \partial_x (\alpha_l \rho_l v_l^2 + \alpha_g \rho_g v_g^2 + p) &= -q,\end{aligned}\tag{10}$$

where $\alpha_{l,g}$ is volume fraction, $\rho_{l,g}$ is density, $v_{l,g}$ is velocity, p is common pressure and q is a source/sink term. Subscripts g and l denotes gas and liquid respectively. The source term, q , of the momentum equation is within the numerical model a sum of gravitational and viscous forces per unit volume through the relation

$$q = F_w + F_g = \frac{32v_m\mu_m}{d^2} + (\alpha_l\rho_l + \alpha_g\rho_g)g\cos\theta.\tag{11}$$

Mixture properties are given by $\mu_m = \alpha_l\mu_l + \alpha_g\mu_g$ and $v_m = \alpha_g v_g + \alpha_l v_l$, while g is the gravitational constant and θ is the deviation angle from vertical. This is in accordance with what is presented in [2]. The frictional term F_w is derived from the Darcy-Weisbach equation of frictional pressure drop on the form $F_w = \frac{1}{d}f\frac{1}{2}\rho v|v|$ with $f = \frac{64}{Re}$ being the Darcy friction factor for laminar flow in pipes. It is noted that the pressure drop due to acceleration is neglected as this paper will focus on vertical flow with no change in inner pipe diameter.

For future work it is suggested to implement a more advanced frictional pressure drop relation in order to also account for turbulent flow. A varying inner diameter of the pipe could also be implemented to allow the fluid to experience flow restrictions. It then falls naturally that the accelerational pressure drop is also included.

Remark. What sets the drift-flux model aside from the commonly known two-fluid model, is its combined momentum equation and corresponding slip relation. The two-fluid model consists of two separate momentum balance equations, one for each phase, thus eliminating the need for a slip relation to relate phase velocities to one another.

For the set of equations making up the drift-flux model in (10), the volume fractions α_l, α_g , the densities ρ_l, ρ_g , the velocities v_l, v_g and p are all unknowns. There are altogether 7 unknowns and 3 equations. Additional constraints are therefore needed in order to have a soluble system:

1. Volume fractions satisfy the condition

$$\alpha_l + \alpha_g = 1. \quad (12)$$

2. Analytical expressions for densities as functions of pressure have been derived through thermodynamical derivations²

$$\rho_l = \rho_{l,0} + \frac{p - p_{l,0}}{a_l^2}, \quad (13)$$

$$\rho_g = \frac{p}{a_g^2}, \quad (14)$$

in which a_l , a_g are sound velocities of the respective phase, $\rho_{l,0}$ is a reference liquid density with corresponding reference liquid pressure $p_{l,0}$.

3. The general slip law relating the phase velocities to each other has been given by

$$v_g = C_o v_m + v_d, \quad (15)$$

where v_g , v_m and v_d denotes gas-, mixture- and drift- velocity respectively. C_o is a profile parameter describing the effect of velocity and concentration profiles within the mixture. It is the parameters C_o and v_d that will be paid special attention to in Part III. It is because the the model consists only of one momentum equation that the slip law of (15) is needed. The slip parameters making up the closure law will for different values represent different flow regimes. Initial determination of such slip parameters were performed in [22] where it was experimented with gas-liquid flow in small diameter pipes.

Table 7.1 lists the constant parameters used in equations (11)-(14).

Table 7.1: Parameters used in numerical computations of the drift-flux model.

Parameter	Value	Description
$\rho_{l,0}$	1000kg/m ³	Reference density liquid
$p_{l,0}$	10 ⁵ Pa	Reference pressure liquid
a_l	1000m/s	Sound velocity in liquid phase
a_g	316.22m/s	Sound velocity in gas phase
μ_l	5 · 10 ⁻² Pa · s	Liquid viscosity
μ_g	5 · 10 ⁻⁶ Pa · s	Gas viscosity

7.3 Hyperbolicity

A hyperbolic system of PDE's is said to exhibit wave-like characteristics in the solution with finite propagation velocities. As it is to be expected that the solution of the drift-flux model exhibits these characteristics both in pressure and mass transport, it might be of interest for the average reader to see and verify that the system of PDE's making up the drift-flux model in Section 7 is in fact hyperbolic. The following proof has been derived.

²For the gas, an approximation to the sound velocity can be obtained from the gas law $pV = ZnRT$, solving for $a_g = \sqrt{\frac{p}{\rho_g}} = \sqrt{\frac{ZRT}{M}}$

The set of equations making up the drift-flux model in equation (10) can be expressed as

$$\partial_t U + \partial_x F(U) = G(U), \quad (16)$$

in which

$$U = \begin{pmatrix} \alpha_l \rho_l \\ \alpha_g \rho_g \\ \alpha_l \rho_l v_l + \alpha_g \rho_g v_g \end{pmatrix}, \quad F(U) = \begin{pmatrix} \alpha_l \rho_l v_l \\ \alpha_g \rho_g v_g \\ \alpha_l \rho_l v_l^2 + \alpha_g \rho_g v_g^2 + p \end{pmatrix}, \quad G(U) = \begin{pmatrix} 0 \\ 0 \\ -q \end{pmatrix},$$

with $u_1 = \alpha_l \rho_l$, $u_2 = \alpha_g \rho_g$ and $u_3 = \alpha_l \rho_l v_l + \alpha_g \rho_g v_g$. Defining the flux vector $F(U) = (f_1 \ f_2 \ f_3)^T$, elements f_1 , f_2 and f_3 can be expressed in terms of the conservative variables in U and equation (16) can be expanded to

$$\partial_t \begin{pmatrix} u_1 \\ u_2 \\ u_3 \end{pmatrix} + \partial_x \begin{pmatrix} u_1 v_l \\ u_2 v_g \\ u_1 v_l^2 + u_2 v_g^2 + p(u_1, u_2) \end{pmatrix} = \begin{pmatrix} 0 \\ 0 \\ -q \end{pmatrix}. \quad (17)$$

The equation set given in (17) is said to be hyperbolic if the Jacobian for the flux term has only real eigenvalues. This is what will be examined further in Section 7.3.1 for a case of no-slip conditions. With regards to the flux term in eq. (17), the reader is reminded of the definition of the Jacobian matrix

$$J = \begin{pmatrix} \frac{\partial f_1}{\partial u_1} & \frac{\partial f_1}{\partial u_2} & \frac{\partial f_1}{\partial u_3} \\ \frac{\partial f_2}{\partial u_1} & \frac{\partial f_2}{\partial u_2} & \frac{\partial f_2}{\partial u_3} \\ \frac{\partial f_3}{\partial u_1} & \frac{\partial f_3}{\partial u_2} & \frac{\partial f_3}{\partial u_3} \end{pmatrix}. \quad (18)$$

Remark. Hyperbolicity is generally dependent on what slip is in effect, thus making it more difficult to determine the Jacobian of (18).

7.3.1 Hyperbolicity With No-Slip Conditions

For a case of no-slip condition, $v_g = v_l = v$, thus making $C_o = 1$ and $v_d = 0$ in equation (15). The common velocity v can be expressed in terms of the conserved variables through $v(U) = \frac{u_3}{u_1 + u_2}$. Substituting this expression into (17)

$$\partial_t \begin{pmatrix} u_1 \\ u_2 \\ u_3 \end{pmatrix} + \partial_x \begin{pmatrix} \frac{u_1 u_3}{u_1 + u_2} \\ \frac{u_2 u_3}{u_1 + u_2} \\ \frac{u_1 u_3^2}{(u_1 + u_2)^2} + \frac{u_2 u_3^2}{(u_1 + u_2)^2} + p(u_1, u_2) \end{pmatrix} = \begin{pmatrix} 0 \\ 0 \\ -q \end{pmatrix},$$

it is seen that all that is needed in order to determine the Jacobian for the flux term is an expression for $p(u_1, u_2)$. By using the definitions of u_1 and u_2 , where $u_1 = \alpha_l \rho_l$ and $u_2 = \alpha_g \rho_g$, equation (12) can be expressed in terms of ρ and u through

$$\frac{u_1}{\rho_l(p)} + \frac{u_2}{\rho_g(p)} = 1. \quad (19)$$

Simple correlations used for the phase densities $\rho_{l,g}(p)$ are given in equation (13) and (14). Substituting respective densities into equation (19), it is rewritten

$$\frac{u_1}{\rho_{l,0} + \frac{p - p_{l,0}}{a_l^2}} + \frac{u_2 a_g^2}{p} = 1.$$

Rearranging this equation with respect to pressure p yields a common second order polynomial of the type

$$p^2 + Bp + C = 0,$$

in which $B = a_l^2 \left(\rho_{l,0} - \frac{p_{l,0}}{a_l^2} - u_1 - \left(\frac{a_g}{a_l} \right)^2 u_2 \right)$ and $C = u_2 (a_g a_l)^2 \left(\frac{p_{l,0}}{a_l^2} - \rho_{l,0} \right)$. When solving for pressure p , only the positive root proves to be a real solution as the negative root yields negative pressures for all u_1 and u_2 . The pressure is then given by

$$p(u_1, u_2) = \frac{-B + \sqrt{B^2 - 4C}}{2}. \quad (20)$$

A three-dimensional plot of $p(u_1, u_2)$ is included in Figure 7.1, where it noted from the plots when $u_2 = 0$, that

$$p(u_1, 0) = \begin{cases} 0 & , u_1 < \rho_{l,0} - \frac{p_{l,0}}{a_l^2} \\ -B & , u_1 \geq \rho_{l,0} - \frac{p_{l,0}}{a_l^2} \end{cases}.$$

The Jacobian of the flux term in equation (17) can now be expressed as

$$J = \begin{pmatrix} \frac{u_2}{u_1+u_2}v & -\frac{u_1}{u_1+u_2}v & \frac{u_1}{u_1+u_2} \\ -\frac{u_2}{u_1+u_2}v & \frac{u_1}{u_1+u_2}v & \frac{u_2}{u_1+u_2} \\ -v^2 + \frac{\partial p}{\partial u_1} & -v^2 + \frac{\partial p}{\partial u_2} & 2v \end{pmatrix}, \quad (21)$$

where it is further assumed that $\alpha_g \rho_g \ll \alpha_l \rho_l$, i.e $u_2 \ll u_1$, transforming the Jacobian of (18) to

$$J = \begin{pmatrix} 0 & -v & 1 \\ 0 & v & 0 \\ -v^2 + \frac{\partial p}{\partial u_1} & -v^2 + \frac{\partial p}{\partial u_2} & 2v \end{pmatrix}.$$

The eigenvalues of the Jacobian matrix can be found through the relation $|J - \lambda I| = 0$, thus

$$\lambda_1 = v - \omega, \quad \lambda_2 = v \quad \lambda_3 = v + \omega, \quad (22)$$

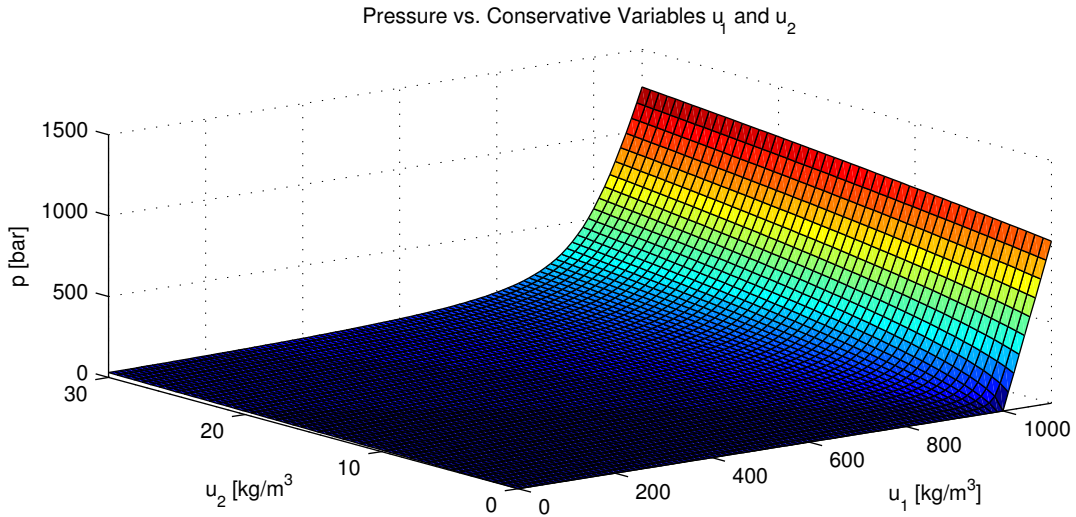
where λ designates the different eigenvalues. λ_1 and λ_3 are seen to represent the velocity of pressure pulses traveling in opposite directions while λ_2 represents the velocity of the moving fluid. Note that $\omega = \sqrt{\frac{\partial p}{\partial u_1}}$ in equation (22).

With the assumptions of $\alpha_g \rho_g \ll \alpha_l \rho_l$ and $\rho_l \approx \text{constant}$ the following ‘‘approximate sound velocity’’ can be obtained from $\omega^2 = \frac{\partial p}{\partial u_1}$. See [2].

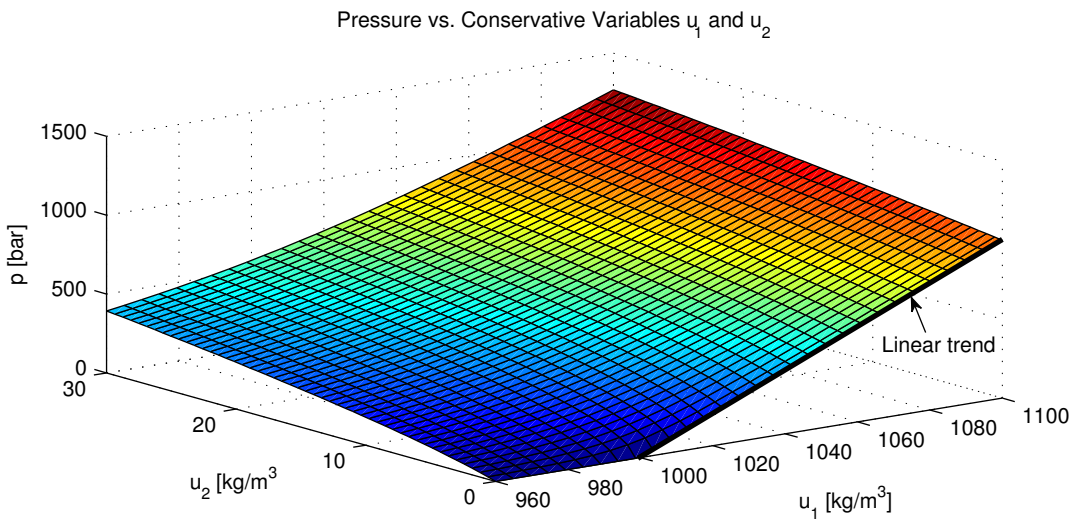
$$\omega^2 = \frac{p}{\alpha_g \rho_l (1 - C_o \alpha_g)}. \quad (23)$$

For simplicity, it is the approximate sound velocity from equation (23) that will be used when splitting the fluxes in Section 8.2 and 8.3 as it does not rely continuous computation of the Jacobian. See also [12] where a similar yet more compacted proof of hyperbolicity has been derived.

Remark. As it would be desirable to inspect how the sound velocity changes for different mixtures of gas and liquid, it would not be sufficient to base further analysis on the eigenvalues given in (22), as the assumption $\alpha_g \rho_g \ll \alpha_l \rho_l$ has already been made. At best it would be possible to study a range in which the previous assumption would be thought to hold.



a)



b)

Figure 7.1: Pressure versus the conserved variables u_1 and u_2 . Figure b) gives a closer view of the linear trend in a) when $u_1 > 999.9$ kg/m³ for $u_2 = 0$ kg/m³. Drawn using `p_u1_u2.m` in Appendix A.10.

On the other hand, if the system of fluids were thought of as to be in a stand-still setting, i.e $v = 0$ m/s, the Jacobian of (18) simply reduces to

$$J = \begin{pmatrix} 0 & 0 & \frac{u_1}{u_1+u_2} \\ 0 & 0 & \frac{u_2}{u_1+u_2} \\ \frac{\partial p}{\partial u_1} & \frac{\partial p}{\partial u_2} & 0 \end{pmatrix}$$

which would lead to the eigenvalues being easily computed from

$$\begin{vmatrix} -\lambda & 0 & \frac{u_1}{u_1+u_2} \\ 0 & -\lambda & \frac{u_2}{u_1+u_2} \\ \frac{\partial p}{\partial u_1} & \frac{\partial p}{\partial u_2} & -\lambda \end{vmatrix} = 0$$

making

$$\lambda_1 = -\sqrt{\frac{1}{u_1+u_2} \left(u_2 \frac{\partial p}{\partial u_2} + u_1 \frac{\partial p}{\partial u_1} \right)}, \quad \lambda_2 = 0, \quad \lambda_3 = \sqrt{\frac{1}{u_1+u_2} \left(u_2 \frac{\partial p}{\partial u_2} + u_1 \frac{\partial p}{\partial u_1} \right)}. \quad (24)$$

It is easy to see from (24) that λ_2 is the mixture velocity of the stagnant fluid with λ_1 and λ_3 being the velocities of opposite directions traveling pressure pulses. The positive root of (24) has been plotted in Figure 7.2 for a data case given in Table 7.1 with atmospheric pressure $p = 10^5$ Pa, and will from now on be referred to as the “real sound velocity”. This would correspond to the fluid mixture being in a horizontal setting under atmospheric conditions. It is to be noted from the figure that the sound velocity is much lower when the fluids are mixed than when they appear as single phases.

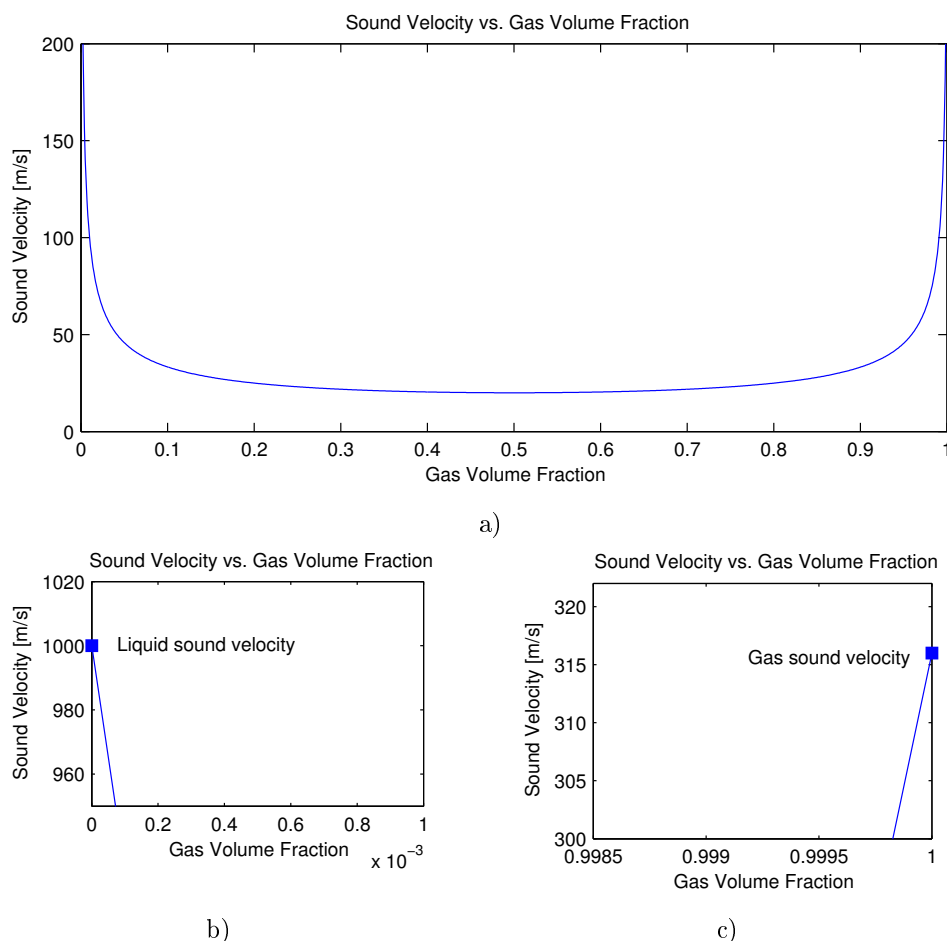


Figure 7.2: Sound velocity for a stagnant fluid under atmospheric conditions as a function of gas volume fraction in a). Zoomed in on limiting sound velocities in b) and c). Drawn using `sound_velocity.m` in Appendix A.5.

In reality, the sound velocity for a two-phase mixture will depend on the reigning flow regime and as such the corresponding slip relation. As it is the approximate sound velocity from equation (23) that will be used further, a plot comparing the “approximate sound velocity” with the “real sound velocity” from equation (24) is included in Figure 7.3. It is observed from the figure that the approximate sound velocity over-estimates the sound velocity for high gas volume fractions, the reason being that the assumption of $\alpha_g \rho_g \ll \alpha_l \rho_l$ made in deriving the approximate sound velocity may no longer be valid. For sake of convenience, it is mentioned that the “approximate sound velocity” roughly coincides with the “real sound velocity” for lower gas volume fractions, except when $\alpha_g \rightarrow 0$. The approximation of sound velocity does not contain within it any information about sound velocity when in single-phase regions ($\alpha_g = 0, 1$) and thus this is enforced by implementing limiting boundaries in equation (37).

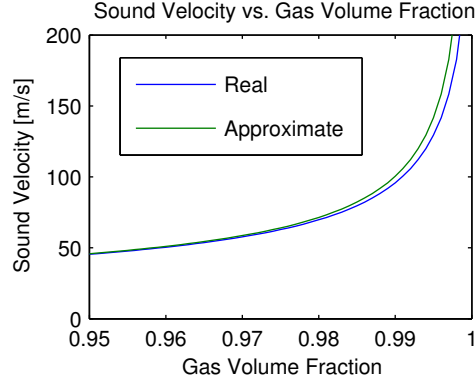


Figure 7.3: Comparison of “approximate” sound velocity from eq. (24) with “real” sound velocity from eq. (23) as functions of gas volume fraction. Drawn using `sound_velocity.m` in Appendix A.5.

7.3.2 Computing Flux Terms from Conserved Variables

This section is included to emphasize how the flux term, F^n , of equation (30) is computed from the conserved variables u_1 , u_2 and u_3 . In order to be able to update U_i^{n+1} in the previously mentioned equation, both U_i^n and the flux terms F^n need to be determined. For the previous time-step, U_i^n are known through initial conditions, however F^n is not. For computation of F^n the primitive variables $(\alpha_l, \alpha_g, \rho_l, \rho_g, v_l, v_g, p)^n$ needs to be determined.

1. First off, the pressure $p(u_1, u_2)$ is determined directly from equation (20) as both u_1 and u_2 are known for the given time-step.
2. Once $p(u_1, u_2)$ is known, the densities are determined directly from equation (13) and (14).
3. From the definitions of u_1 and u_2 given in Section 7.3.1, the volume fractions are determined from

$$\alpha_l = \frac{u_1}{\rho_l}, \quad \alpha_g = \frac{u_2}{\rho_g}.$$

4. Lastly, the velocities needs determining. The reader is reminded of the definition of u_3 in Section 7.3.1, $u_3 = \alpha_l \rho_l v_l + \alpha_g \rho_g v_g$, which now is rewritten

$$u_1 v_l + u_2 v_g = u_3. \quad (25)$$

Substituting the definition of mixture velocity into the general slip formulation yields

$$-C_o \alpha_l v_l + (1 - C_o \alpha_g) v_g = v_d. \quad (26)$$

As can be seen from equation (25) and (26), it is a system of linear equations with only two unknowns, namely v_l and v_g . The system can then be expressed in matrix form

$$\begin{pmatrix} u_1 & u_2 \\ w_1 & w_2 \end{pmatrix} \begin{pmatrix} v_l \\ v_g \end{pmatrix} = \begin{pmatrix} u_3 \\ v_d \end{pmatrix},$$

where $w_1 = -C_o\alpha_l$ and $w_2 = 1 - C_o\alpha_g$. It is with ease solved for v_l and v_g using Gaussian elimination, and thus

$$v_l = \frac{u_3w_2 - u_2v_d}{u_1w_2 - u_2w_1} \Rightarrow \frac{u_3(1 - C_o\alpha_g) - u_2v_d}{u_1(1 - C_o\alpha_g) + u_2C_o\alpha_l} \quad (27)$$

and

$$v_g = \frac{u_1v_d - u_3w_1}{u_1w_2 - u_2w_1} \Rightarrow \frac{u_1v_d + u_3C_o\alpha_l}{u_1(1 - C_o\alpha_g) + u_2C_o\alpha_l}. \quad (28)$$

The slip parameters C_o and V_d bear with them the ability to be reduced to 1 and 0 respectively for a case of pure gas region. This way there will be no difficulties with having a continuous phase velocity profile even though the phase itself is not present in a given region. An important feature when velocities are determined is to be able to calculate the velocities when only a single-phase is present. When having single-phase flows, it is seen from equation (27) and (28) that they reduce to

$$v_l(\alpha_g = 0) = \frac{u_3}{u_1}, \quad v_l(\alpha_g = 1) = \lim_{\alpha_g \rightarrow 1} \frac{u_2v_g(1 - C_o\alpha_g) - u_2v_d}{u_2C_o(1 - \alpha_g)} = v_g \quad (29)$$

and

$$v_g(\alpha_g = 0) = C_ov_l + v_d, \quad v_g(\alpha_g = 1) = \lim_{\alpha_g \rightarrow 1} \frac{u_3C_o(1 - \alpha_g)}{u_2C_o(1 - \alpha_g)} = \frac{u_3}{u_2}.$$

Remark. Had not C_o and v_d reduced to 1 and 0 respectively for $\alpha_g = 1$, the expression for $v_l(\alpha_g = 1)$ in equation (29) would diverge without some restriction in $\frac{\partial(\alpha_g C_o)}{\partial \alpha_g}$ and $\frac{\partial v_d}{\partial \alpha_g}$.

8 Numerical Schemes

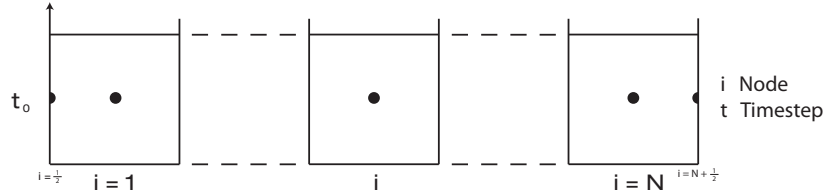


Figure 8.1: Illustration of the computational grid used in Matlab when computing a numerical solution of the drift-flux model. Drawn using Adobe Illustrator CS5.

In order to find a solution in space and time for the set of equations making up the drift-flux model in (10), the set is to be solved numerically. The first step in doing this is to properly design a time- and space grid in which the model equations will be applied. To get a feel for the grid being used as well as notation, Figure 8.1 is included. A proper discretization of the equation set is then needed to relate it to the grid in which it is desirable to find a solution. To aid the reader in further understanding flux splitting techniques, as the MATLAB model is explicit in time, a general introduction into explicit discretization is included before divulging into upwind discretization and flux-splitting techniques.

Applying an explicit discretization to the general conservation law given in equation (16)

$$\frac{U_i^{n+1} - U_i^n}{\Delta t} = \frac{1}{\Delta x} \left(F_{i-\frac{1}{2}}^n - F_{i+\frac{1}{2}}^n \right) + G(U_i^n)$$

where i is the coordinate, n the time-step and $F_{i\pm\frac{1}{2}}^n$ is flux at either node boundaries. Rearranging this expression with regards to the time updating of U_i^{n+1}

$$U_i^{n+1} = U_i^n + \gamma \left(F_{i-\frac{1}{2}}^n - F_{i+\frac{1}{2}}^n \right) + G(U_i^n) \Delta t \quad (30)$$

where $\gamma = \frac{\Delta t}{\Delta x}$.

It is the approximation of the flux term $F_{i\pm\frac{1}{2}}^n$ which yields difficulties in the numerical representation of the system. The flux along node boundaries will vary with time and should ideally approximate the timed average $F_{i\pm\frac{1}{2}}^n \approx \frac{1}{\Delta t} \int_{t_n}^{t_{n+1}} f \left(U_{i\pm\frac{1}{2}}(t) \right) dt$.

For hyperbolic problems it is known that the solutions propagate at finite speeds as shown in Section 7.3. Bearing this in mind, it is reasonable to assume that the flux at an interface can be given as a function of the neighboring blocks, i.e $F_{i-\frac{1}{2}}^n = \mathcal{F}(U_{i-1}^n, U_i^n)$ and $F_{i+\frac{1}{2}}^n = \mathcal{F}(U_i^n, U_{i+1}^n)$. See also [8]. When applying this to (30), the general explicit formulation is written

$$U_i^{n+1} = U_i^n + \gamma \left(\mathcal{F}(U_{i-1}^n, U_i^n) - \mathcal{F}(U_i^n, U_{i+1}^n) \right) + G(U_i^n) \Delta t.$$

So to not confuse the reader in further reading, he/she is made aware of an alternate notation used to replace the node coordinates i and $i + 1$. Sub-notes L and R are respectively used to replace the node coordinates whereas the idea is that L represents the node to the left of an interface and R represents the node to the right.

8.1 Flux Splitting

The flux term F of equation (16) is split into a convective and a pressure term via

$$F = F_c + F_p = \begin{pmatrix} \alpha_l \rho_l v_l \\ \alpha_g \rho_g v_g \\ \alpha_l \rho_l v_l^2 + \alpha_g \rho_g v_g^2 \end{pmatrix} + \begin{pmatrix} 0 \\ 0 \\ p \end{pmatrix} \quad (31)$$

where the convective flux is further split for liquid and gas through

$$F_c = \alpha_l \rho_l v_l \begin{pmatrix} 1 \\ 0 \\ v_l \end{pmatrix} + \alpha_g \rho_g v_g \begin{pmatrix} 0 \\ 1 \\ v_g \end{pmatrix}. \quad (32)$$

Following in the ways of [2], where $\Phi_l = (1, 0, v_l)^T$ and $\Phi_g = (0, 1, v_g)^T$, the discretization of the flux at the interface $F_{i+\frac{1}{2}}$ is given as

$$F_{i+\frac{1}{2}} = \frac{1}{2} \left[(\alpha_l \rho_l v_l)_{i+\frac{1}{2}} (\Phi_{l,L} + \Phi_{l,R}) - \left| (\alpha_l \rho_l v_l)_{i+\frac{1}{2}} \right| (\Phi_{l,R} - \Phi_{l,L}) \right] + \frac{1}{2} \left[(\alpha_g \rho_g v_g)_{i+\frac{1}{2}} (\Phi_{g,L} + \Phi_{g,R}) - \left| (\alpha_g \rho_g v_g)_{i+\frac{1}{2}} \right| (\Phi_{g,R} - \Phi_{g,L}) \right] + (F_p)_{i+\frac{1}{2}}, \quad (33)$$

in which sub notes L and R are used to indicate i and $i + 1$ respectively as mentioned earlier. Various methods in handling the mass flux at an interface, $(\alpha_k \rho_k v_k)_{i+\frac{1}{2}}$, is what gives life to the splitting schemes described in Section 8.4.1 and 8.3.

Remark. The discretization of the flux in (33) is done in such a way to ensure the direction of the flux will come out correctly. I.e for a case of counter current flow, $(\alpha_l \rho_l v_l)_{i+\frac{1}{2}} < 0$ and $(\alpha_g \rho_g v_g)_{i+\frac{1}{2}} > 0$, then

$$F_{i+\frac{1}{2}} = (\alpha_l \rho_l v_l)_{i+\frac{1}{2}} \Phi_{l,R} + (\alpha_g \rho_g v_g)_{i+\frac{1}{2}} \Phi_{g,L} + (F_p)_{i+\frac{1}{2}}.$$

8.2 FVS

The discretization scheme implemented in the model in Part III, in which further simulations are based upon, is of the AUSMV type. This splitting method is further described in Section 8.3. Flux vector splitting, or FVS, is included in this paper as it lays the foundation for AUSMV, and as such, the only difference between the two is a slight modification done in the velocity splitting term. Flux vector splitting is generally better equipped to capture fast propagating pressure pulses while introducing excessive dissipation at slower moving discontinuous volume fractions. This excessive dissipation for the FVS scheme is derived in Section 8.4.3.

Still following in the ways of [2], the inter facial mass flux $(\alpha_k \rho_k v_k)_{i+\frac{1}{2}}$ that enters into (33) is for an FVS type scheme written

$$(\alpha_k \rho_k v_k)_{i+\frac{1}{2}}^{FVS} = (\alpha_k \rho_k)_L V^+ \left(v_L, c_{i+\frac{1}{2}} \right) + (\alpha_k \rho_k)_R V^- \left(v_R, c_{i+\frac{1}{2}} \right), \quad k = l, g \quad (34)$$

where V^\pm is given in (36). The general flux expression from equation (33) can then be written

$$F_{i+\frac{1}{2}} = (\alpha_l \rho_l)_L \Psi_{l,L}^+ + (\alpha_l \rho_l)_R \Psi_{l,R}^- + (\alpha_g \rho_g)_L \Psi_{g,L}^+ + (\alpha_g \rho_g)_R \Psi_{g,R}^- + (F_p)_{i+\frac{1}{2}}, \quad (35)$$

where the pressure flux $(F_p)_{i+\frac{1}{2}} = (0, 0, p_{i+\frac{1}{2}})^T$. Parameter Ψ which is used in defining the convective flux is defined in Section 8.2.1.

8.2.1 Convective Flux

Below is an overview of the splitting parameters used in properly defining the convective flux of equation (35) for liquid

$$\begin{aligned} \Psi_{l,L}^+ &= \Psi_l^+ \left(v_{l,L}, c_{i+\frac{1}{2}} \right) & \Psi_{l,R}^- &= \Psi_l^- \left(v_{l,R}, c_{i+\frac{1}{2}} \right) \\ &\uparrow & &\uparrow \\ \Psi_l^+ (v, c) &= V^+ (v, c) \begin{pmatrix} 1 \\ 0 \\ v \end{pmatrix} & \Psi_l^- &= V^- (v, c) \begin{pmatrix} 1 \\ 0 \\ v \end{pmatrix} \end{aligned}$$

and for gas

$$\begin{aligned} \Psi_{g,L}^+ &= \Psi_g^+ \left(v_{g,L}, c_{i+\frac{1}{2}} \right) & \Psi_{g,R}^- &= \Psi_g^- \left(v_{g,R}, c_{i+\frac{1}{2}} \right) \\ &\uparrow & &\uparrow \\ \Psi_g^+ (v, c) &= V^+ (v, c) \begin{pmatrix} 0 \\ 1 \\ v \end{pmatrix} & \Psi_g^- &= V^- (v, c) \begin{pmatrix} 0 \\ 1 \\ v \end{pmatrix}. \end{aligned}$$

The velocity splitting V^\pm is used for both liquid- and gas phase and is defined as

$$V^\pm(v, c) = \begin{cases} \pm \frac{1}{4c} (v \pm c)^2, & |v| \leq c \\ \frac{1}{2} (v \pm |v|), & \text{otherwise} \end{cases} \quad (36)$$

with c being the sound velocity for the mixture. It is noted for supersonic flows, $|v| > c$ that $V = 0$ m/s for opposite directions of v , as should be expected³. A handy view when looking at the velocity splitting function is to see it as a way of weighting the velocities v_L and v_R in order to describe the interfacial flux in a good way. For illustrational purposes, relative velocity split $\frac{V^\pm}{c}$ (also known as the mach split M^\pm) has been plotted in Figure 8.2 as a function of relative velocity $\frac{v}{c}$ (also known as the mach number, M). This is done by dividing both sides of eq. (36) by c to conceal the splitting functions dependence on sound velocity.

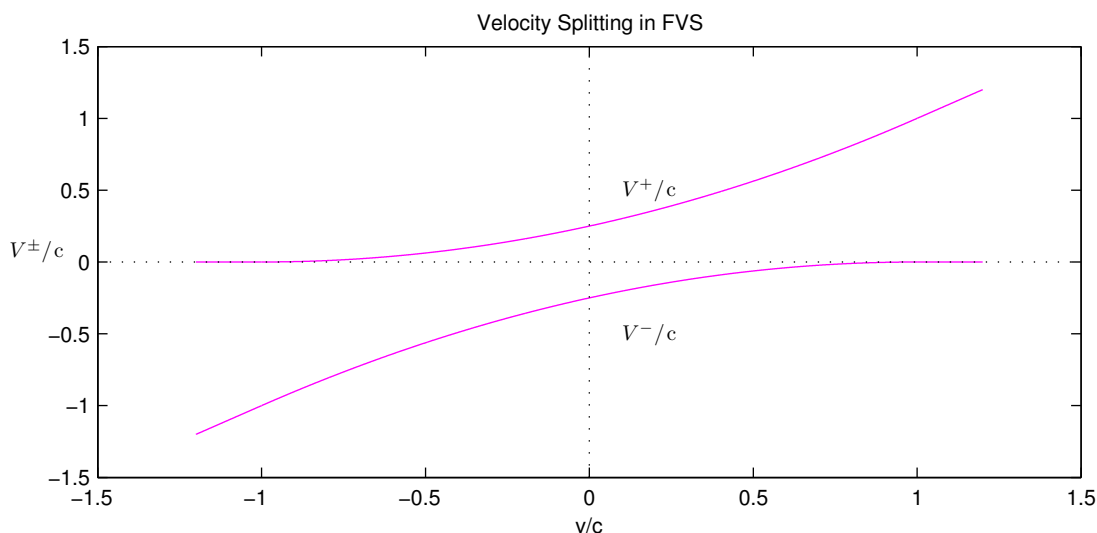


Figure 8.2: Mach splitting function versus mach number used in FVS. Drawn using vsplit_plot.m in Appendix A.3.

The overall sound velocity c to be used in the velocity splitting function is determined by

$$c(\alpha_g) = \begin{cases} a_l, & \alpha_g < \epsilon \\ \omega, & \epsilon \leq \alpha_g \leq 1 - \epsilon \\ a_g, & \alpha_g > 1 - \epsilon \end{cases} \quad (37)$$

where the “approximate sound velocity”, ω , is given by equation (23) on page 12.

8.2.2 Pressure Flux

As the convective flux of equation (35) is now properly defined, it is necessary to also define the interfacial pressure flux $p_{i+\frac{1}{2}}$ that enters into the expression of $(F_p)_{i+\frac{1}{2}}$ from eq. (35). This pressure flux is defined via a pressure splitting function weighting the pressures p_L and p_R through

³It is also worth noting from the velocity splitting function that $V^+ + V^- = v$.

$$p_{i+\frac{1}{2}} = P^+ (v_L, c_{i+\frac{1}{2}}) p_L + P^- (v_R, c_{i+\frac{1}{2}}) p_R$$

where the splitting function used is defined by

$$P^\pm = V^\pm (v, c) \cdot \begin{cases} \frac{1}{c} (\pm 2 - \frac{v}{c}), & |v| \leq c \\ \frac{1}{v}, & \textit{otherwise} \end{cases}.$$

As pressure is common for both phases, mixture velocity v_m has been deemed a suitable velocity to be used in the expression for P^\pm in order to properly define the interfacial pressure flux.

8.3 AUSMV

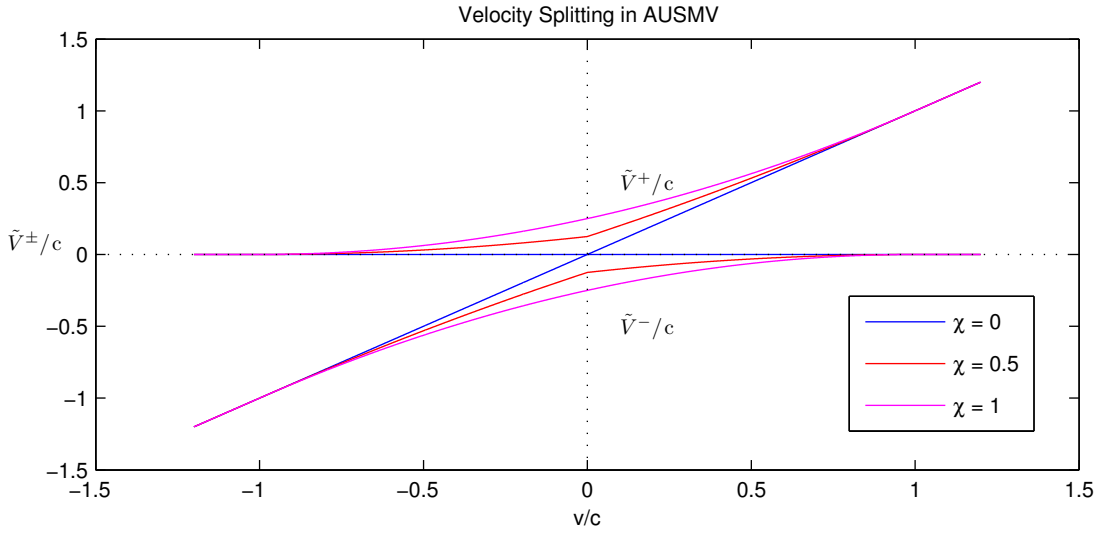


Figure 8.3: Mach split used in AUSMV versus Mach number. Drawn using vsplit_plot.m in Appendix A.3.

The method of combining the attractive features of flux vector splitting (FVS) with the attractive features of flux difference splitting (FDS) was first introduced by Liou and Steffen in [9]. This method is known as an advective upwind splitting method, or AUSM. In later years, several modifications to AUSM has been derived, where AUSMV is one of these and will be presented here.

AUSMV was first proposed in [19] and is similar to FVS except the V^\pm term in equation (36) is modified with a parameter χ to better adhere with discontinuities in slower moving volume fractions and avoid the excess dissipation present in FVS.

$$\tilde{V}^\pm (v, c, \chi) = \begin{cases} \chi V^\pm (v, c) + (1 - \chi) \frac{v \pm |v|}{2}, & |v| \leq c \\ \frac{1}{2} (v \pm |v|), & \textit{otherwise} \end{cases}$$

in which χ is chosen such that the condition $\chi_R \alpha_R - \chi_L \alpha_L = 0$ holds. See AUSM part of Section 8.4.3 where this condition for χ is derived. Although χ can be chosen in many ways and still uphold

the previous condition, one way is to set $\chi_R = \alpha_L$ and $\chi_L = \alpha_R$. This what is implemented in the model further numerical simulations will be based on. Relative mach split $\tilde{M}^\pm = \frac{\tilde{V}^\pm}{c}$ as a function the mach number $M = \frac{v}{c}$ is plotted in Figure 8.3 for a given set of χ parameters⁴ $\chi = [0 \quad 0.5 \quad 1]$.

8.4 Dissipation for Different Schemes at Contact Discontinuities

At an interface, the mass flux term $(\alpha_k \rho_k v_k)_{i+\frac{1}{2}}$ can be seen as an arithmetic average between node L and R and a dissipative term $d_{k,i+\frac{1}{2}}$ through the relation

$$(\alpha_k \rho_k v_k)_{i+\frac{1}{2}} = \frac{(\alpha_k \rho_k v_k)_L + (\alpha_k \rho_k v_k)_R}{2} - \frac{1}{2} d_{k,i+\frac{1}{2}}, \quad k = l, g. \quad (38)$$

This dissipative term is what causes the ‘‘smearing’’ effect that can be seen for different schemes when encountering discontinuities. Ideally $d_{k,i+\frac{1}{2}} \rightarrow 0$ for a scheme handling discontinuities well. In Section 8.4.3 it is to be proven that $d_{k,i+\frac{1}{2}}^{AUSMV} \rightarrow 0$ for a stationary discontinuity while $d_{k,i+\frac{1}{2}}^{FVS}$ does not. Similar derivations are also done in [2].

8.4.1 FVS

The mass flux term of equation (38) is to be derived for an FVS-type scheme along with its dissipative term $d_{k,i+\frac{1}{2}}^{FVS}$. The reader is reminded of the condition $V^+ + V^- = v$, thus when substituted into (34) yields

$$(\alpha_k \rho_k v_k)_{i+\frac{1}{2}}^{FVS} = (\alpha_k \rho_k)_L (v_{k,L} - V_{k,L}^-) + (\alpha_k \rho_k)_R (v_{k,R} - V_{k,R}^+), \quad k = l, g.$$

Adding the above expression with (34), it is easy to rearrange the expression and the resulting form of (38) is obtained through

$$(\alpha_k \rho_k v_k)_{i+\frac{1}{2}}^{FVS} = \frac{(\alpha_k \rho_k v_k)_L + (\alpha_k \rho_k v_k)_R}{2} - \frac{1}{2} d_{k,i+\frac{1}{2}}^{FVS}, \quad k = l, g,$$

in which $d_{k,i+\frac{1}{2}}^{FVS} = (\alpha_k \rho_k)_L (V_{k,L}^- - V_{k,L}^+) + (\alpha_k \rho_k)_R (V_{k,R}^+ - V_{k,R}^-)$.

8.4.2 AUSMV

As only the velocity splitting terms differ between the FVS and AUSM schemes, it translates directly that

$$(\alpha_k \rho_k v_k)_{i+\frac{1}{2}}^{AUSMV} = \frac{(\alpha_k \rho_k v_k)_L + (\alpha_k \rho_k v_k)_R}{2} - \frac{1}{2} d_{k,i+\frac{1}{2}}^{AUSMV}, \quad k = l, g$$

with $d_{k,i+\frac{1}{2}}^{AUSMV} = (\alpha_k \rho_k)_L (\tilde{V}_{k,L}^- - \tilde{V}_{k,L}^+) + (\alpha_k \rho_k)_R (\tilde{V}_{k,R}^+ - \tilde{V}_{k,R}^-)$.

⁴Since χ is to be determined from volume fractions, it is bound by the lower- and upper limit 0 and 1.

8.4.3 Discontinuity Case

At first it is to be observed the behavior of $d_{k,i+\frac{1}{2}}^{FVS}$ and $d_{k,i+\frac{1}{2}}^{AUSMV}$ for a case of a moving discontinuous phase fraction $\alpha_{k,L} \neq \alpha_{k,R}$. Both node pressures and velocities are for this case study set constant, thus

$$p_L = p_R = p, \quad v_{k,L} = v_{k,R} = v_k, \quad |v_k| < c.$$

- For the FVS scheme:

From definitions of velocity splitting defined in (36), the following relations proves to be helpful in coming derivations

$$\begin{aligned} |V_{k,L}| &= V_{k,L}^+ - V_{k,L}^- \Rightarrow \frac{1}{4c_{i+\frac{1}{2}}} \left[\left(v_{k,L} + c_{i+\frac{1}{2}} \right)^2 + \left(v_{k,L} - c_{i+\frac{1}{2}} \right)^2 \right] \\ |V_{k,R}| &= V_{k,R}^+ - V_{k,R}^- \Rightarrow \frac{1}{4c_{i+\frac{1}{2}}} \left[\left(v_{k,R} + c_{i+\frac{1}{2}} \right)^2 + \left(v_{k,R} - c_{i+\frac{1}{2}} \right)^2 \right] \end{aligned}$$

which when substituted into $d_{k,i+\frac{1}{2}}^{FVS}$ from Section 8.4.1 gives

$$d_{k,i+\frac{1}{2}}^{FVS} = (\alpha_k \rho_k)_L (-|V_{k,L}|) + (\alpha_k \rho_k)_R |V_{k,R}|. \quad (39)$$

It is noted for a case of constant phase velocity that $|V_{k,L}| = |V_{k,R}| = |V_k|$, thus substituting for $|V_{k,L}|$ and $|V_{k,R}|$ and expanding the terms yields

$$d_{k,i+\frac{1}{2}}^{FVS} = \frac{(\alpha_k \rho_k)_R - (\alpha_k \rho_k)_L}{4c_{i+\frac{1}{2}}} \left[\left(v_k + c_{i+\frac{1}{2}} \right)^2 + \left(v_k - c_{i+\frac{1}{2}} \right)^2 \right].$$

From this expression the general form of the dissipation term for FVS for a moving discontinuity is found to be

$$d_{k,i+\frac{1}{2}}^{FVS} = \frac{[(\alpha_k \rho_k)_R - (\alpha_k \rho_k)_L] \left(v_k^2 + c_{i+\frac{1}{2}}^2 \right)}{2c_{i+\frac{1}{2}}}. \quad (40)$$

For a case of constant pressure $\rho_L = \rho_R = \rho_k$ and $v = 0$ (stationary discontinuity) it is easy to see from (40) that the dissipative term does not vanish as desired, and the inter-facial term comes out

$$(\alpha_k \rho_k v_k)_{i+\frac{1}{2}}^{FVS} = -\rho_k \frac{\alpha_{k,R} - \alpha_{k,L}}{4} c_{i+\frac{1}{2}} \neq 0$$

where it is noted that the mixture sound velocity, c , is a major contributor to the numerical dissipation for the FVS scheme. The reader is reminded of Figure 7.2 where “real sound velocity” is plotted against α_g , to give an indication of how the dissipation will vary with $c(\alpha)$. In transitions from single- to two-phase the dissipative term of FVS is seen to be very significant.

- For the AUSMV scheme:

It proves convenient to introduce similar expressions as for FVS to be used in forthcoming derivations in which

$$\begin{aligned} \left| \tilde{V}_{k,L} \right| &= \tilde{V}_{k,L}^+ - \tilde{V}_{k,L}^- \Rightarrow \chi_L |V_{k,L}| + (1 - \chi_L) |v| \\ \left| \tilde{V}_{k,R} \right| &= \tilde{V}_{k,R}^+ - \tilde{V}_{k,R}^- \Rightarrow \chi_R |V_{k,R}| + (1 - \chi_R) |v| \end{aligned} \quad k = l, g$$

which when inserted into the dissipative term for FVS from (39) yields

$$d_{k,i+\frac{1}{2}}^{AUSMV} = (\alpha\rho)_{k,L} (-\chi_L |V_{k,L}| - (1 - \chi_L) |v_k|) + (\alpha\rho)_{k,R} (\chi_R |V_{k,R}| + (1 - \chi_R) |v_k|).$$

which for a case of constant pressure, $\rho_{k,L} = \rho_{k,R} = \rho_k$ reduces to

$$d_{k,i+\frac{1}{2}}^{AUSMV} = |V_k| \rho_k (\chi_R \alpha_R - \chi_L \alpha_L) + |v| \rho_k [(1 - \chi_R) \alpha_R - (1 - \chi_L) \alpha_L]. \quad (41)$$

If the moving discontinuity defined earlier is said to be stationary instead, i.e $v = 0$, then the dissipation term simply reduces to

$$d_{k,i+\frac{1}{2}}^{AUSMV} = |V_k| \rho_k (\chi_R \alpha_R - \chi_L \alpha_L),$$

where χ_R and χ_L is chosen so that the condition $\chi_R \alpha_R - \chi_L \alpha_L = 0$ is upheld and $d_{k,i+\frac{1}{2}}^{AUSMV} \rightarrow 0$ for a stationary discontinuity. Once the condition for $\chi_{R,L}$ is obtained, this can then be implemented in the general dissipation term for a moving discontinuity in (41) and thus

$$d_{k,i+\frac{1}{2}}^{AUSMV} = |v_k| \rho_k (\alpha_R - \alpha_L).$$

The inter-facial term for a moving subsonic discontinuity then becomes

$$(\alpha_k \rho_k v_k)_{i+\frac{1}{2}}^{AUSMV} = \rho_k v_k \frac{\alpha_{k,L} + \alpha_{k,R}}{2} - \frac{1}{2} |v_k| \rho_k (\alpha_R - \alpha_L) = \begin{cases} \alpha_{k,R} \rho_k v_k, & -|c| < v_k < 0 \\ 0, & v_k = 0 \\ \alpha_{k,L} \rho_k v_k, & 0 < v_k < |c| \end{cases}.$$

This means that the mass flux at an interface for a moving discontinuity is computed using the parameters for the node at which the mass is flowing from.

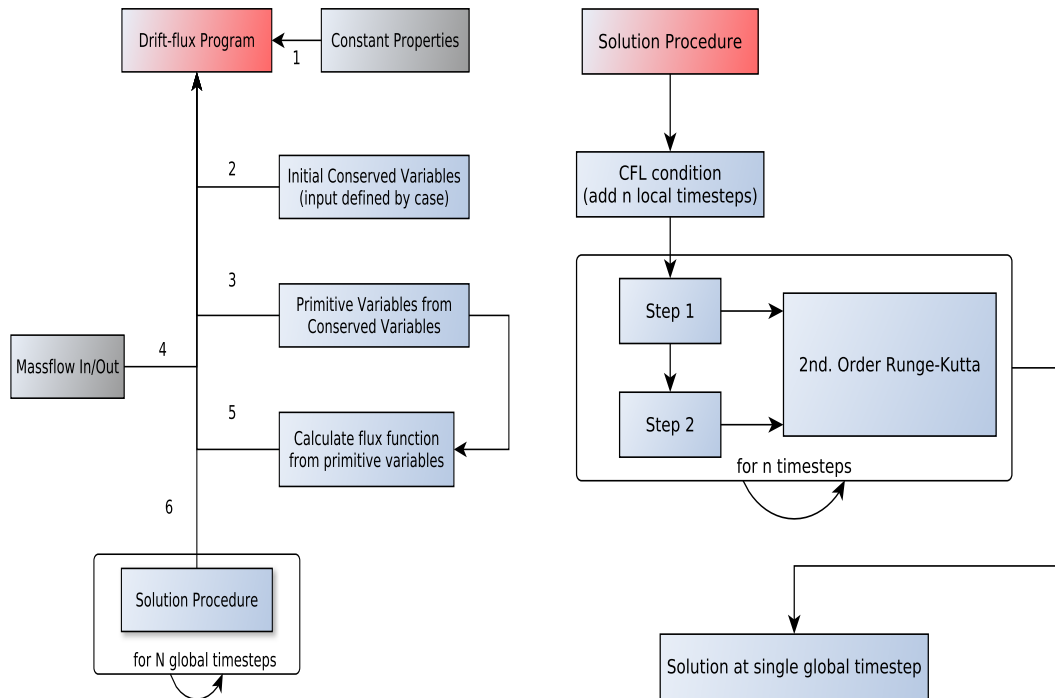


Figure 9.1: Flowcharts describing the work flow in which the MATLAB model operates.

Part III

Numerical Model Simulations

9 Matlab Model

9.1 Work Flow

The numerically adapted drift-flux model is in fact quite comprehensive, and a thorough breakdown of the model is deemed unnecessary and is therefore not included. However, a more general overview of the model and some of the more important subroutines can be seen in Figure 9.1. The following section will elaborate on the grid that is being used in further simulations. The slip relation from Shi et al. [15] is then paid notice, before steady-state and transient simulations are to be presented. All simulations carried out in this thesis will be included in this Part.

9.2 Grid

An illustration of the grid used in Matlab simulations is given in Figure 8.1, in which i denotes the spatial variable and t the time step. Full circles indicate computational nodes and half circles indicate boundary nodes. Initial conditions supply the variables for all nodes at $t = 0$ s while boundary conditions supply the boundary nodes with variables for all times. This is required in order to have a soluble set of partial differential equations. Initial- and boundary conditions will change depending on which simulation case is to be run.

The spatial domain is divided into N computational nodes, making $i = 1, \dots, N$ and correspondingly constant node thickness $\Delta x = \frac{L}{N}$ where L is the pipe length. Total time T for simulations to run is made up of individual time steps of length $\Delta t = \frac{T}{nsteps}$ with $nsteps$ being the total number of time steps.

Since the drift-flux model is solved explicitly in time, see eq. (30), the number of time steps are adjusted so that the CFL condition for stability is always upheld regardless of what Δx is in use. It might be convenient for the average reader to recall the one-dimensional CFL (Courant–Friedrichs–Lewy) condition for hyperbolic partial differential equations as

$$v \frac{\Delta t}{\Delta x} \leq CFL$$

where the CFL condition will vary depending on which set of equation it is to be applied for, v being the velocity. This condition ensures that the solution does not manage to travel through the length of a node, Δx , in the corresponding time step length Δt . Making use of this stability criterion in the drift-flux model, it can be expressed as a condition for determining time-step length Δt as a function of Δx

$$\Delta t = \frac{CFL}{\max(|\lambda_1|, |\lambda_2|, |\lambda_3|)} \Delta x$$

in which $CFL = 0.75$ and the velocity is now whichever eigenvalue of the Jacobian being the highest. In this study the highest sound velocity of the Jacobian will be that of the sound velocity in liquid, 1000 m/s. As the time-step length is determined using the CFL condition, total number of time steps required is easily determined from $nsteps = \frac{T}{\Delta t}$. In order to save time in computations, the numerical model does not store the solution for all $nsteps$, instead a fixed number of steps declared by $NSTEPS$ is stored. The time step-length stored within the model is given by

$$\Delta T = \frac{T}{NSTEPS} = \frac{nsteps}{NSTEPS} \Delta t.$$

To determine pressure at boundary nodes $i = \frac{1}{2}$ and $i = N + \frac{1}{2}$ simple extrapolation of the pressure in the two closest nodes to the boundary is performed by

$$p_{i=\frac{1}{2}} = \frac{3p_1 - p_2}{2}$$

and

$$p_{N+\frac{1}{2}} = \frac{3p_N - p_{N-1}}{2}$$

10 Shi Slip Relation

What will from now on be referred to as the ‘‘SHI slip’’ is the model for determining slip parameters C_o and v_d from Shi et al. [15]. An overview of this slip model is further described in Section 10.1. This is the same slip model implemented in the Multi-Segment well module of Eclipse 2010.

10.1 General

Determination of slip parameters C_o and v_d are not as simple as in Section 12 where the parameters only depended on the volume fraction of gas. These slip parameters will now in addition to the volume fraction also depend on the mixture velocity v_m , densities $\rho_{l,g}$, diameter D and the interfacial tension σ_{gl} . For all further purposes, parameters D and σ_{gl} are set constant. A compact description of this slip model for vertical gas-liquid flow is included here to be in accordance with what is presented by Shi et al.. To determine the concentration profile parameter C_o , the following expressions are included

$$C_o = \frac{A}{1 - (A - 1)\gamma^2} \quad \gamma = \frac{\beta - B}{1 - B}, \quad 0 \leq \gamma \leq 1 \quad \beta = \max\left(\alpha_g, F_v \frac{\alpha_g |v_m|}{v_{gsf}}\right) \quad (42)$$

in which

$$v_{gsf} = K_u (\hat{D}) \sqrt{\frac{\rho_l}{\rho_g}} V_c, \quad V_c = \left(\frac{\sigma_{gl} g (\rho_l - \rho_g)}{\rho_l^2}\right)^{\frac{1}{4}}. \quad (43)$$

where A , B , F_v are tuning parameters, K_u is the critical Kutateladze number. F_v is a tuning parameter for the concentration profile parameter’s dependence on the superficial flooding velocity, v_{gsf} .

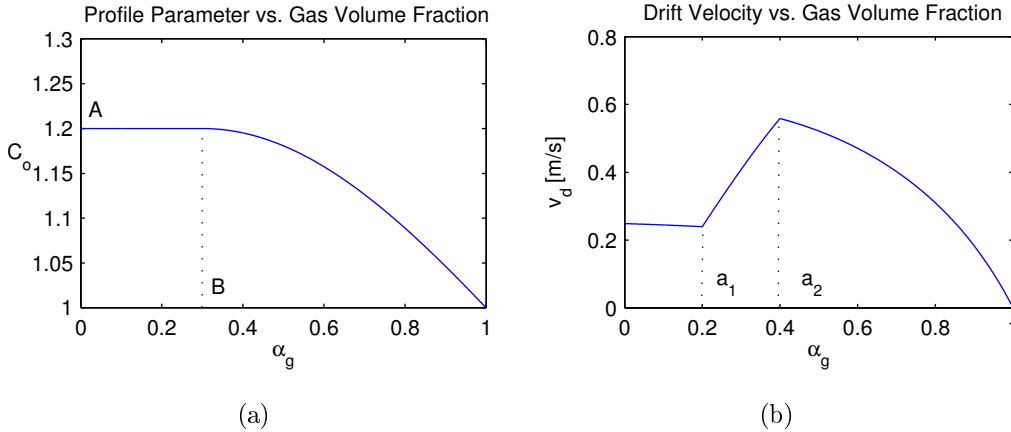


Figure 10.1: Plot of slip parameters C_o and V_d as functions of gas volume fraction for parameters given in Table 10.2. Drawn using `c1_c2.m` in Appendix A.6.

Figure 10.1 a) illustrates C_o as a function of the gas volume fraction for a default set of parameters given in Table 10.2. From the same figure it is seen that parameter A controls what constant value C_o should have when $\alpha_g \leq B$ and B controls when C_o should stop remaining constant and start approaching unity through the relation $C_o = \frac{A}{1 - (A - 1)\gamma^2}$. The reason for C_o remaining constant when

$\alpha_g < B$ is due to γ being bound by the limits 0 and 1, and will attain those limiting values when out of bounds.

The superficial flooding velocity of gas, v_{gsf} , is the gas velocity needed to support a thin liquid film against the pipe wall and prevent it from falling back onto the gas, thus marking the entrance into the annular flow regime. This phenomenon is often referred to in literature as the hanging film phenomenon, and is further described in [21].

Default values for the tunable parameters A , B , a_1 , a_2 and F_v are given in Table 10.2. The critical Kutateladze number used in determining the superficial gas flooding velocity in (43) is a function of dimensionless diameter, given by

$$\hat{D} = \sqrt{\frac{g(\rho_l - \rho_g)}{\sigma_{gl}}} D.$$

Using linear interpolation, the corresponding critical Kutateladze number can be found from Table 10.1.

Once the concentration profile parameter C_o is known, the drift velocity v_d can be determined.

The drift velocity is derived using data for the limits of counter current flow, where it is interpolated between these extrema to have a continuous slip definition.

For low values of the gas volume fraction, $\alpha_g \rightarrow 0$, the bubble rise velocity from [4] is used where $v_{g,rise} = 1.53V_c$, with the characteristic velocity v_c being given in (43). For high values of the volume fraction, $\alpha_g \rightarrow 1$, the flooding velocity v_{gsf} from (43) is used. Between these two extrema the flooding curve from Wallis [20] is normalized and implemented to fit the bubble rise velocity when $\alpha_g \rightarrow 0$ and the flooding velocity when $\alpha_g \rightarrow 1$. As the flooding curve does not by itself fit both these extrema, interpolation between them are necessary. It is this interpolation range that is governed by parameters a_1 and a_2 . See [15, 16]. The drift velocity is then obtainable through the relation

$$v_d = \frac{(1 - \alpha_g C_o) C_o K(\alpha_g) v_c}{\alpha_g C_o \sqrt{\frac{\rho_g}{\rho_l}} + 1 - \alpha_g C_o} \quad (44)$$

in which

$$K(\alpha_g) = \begin{cases} \frac{1.53}{C_o}, & \alpha_g < a_1 \\ K_u(\hat{D}), & \alpha_g \geq a_2 \end{cases}.$$

\hat{D}	K_u
≤ 2	0
4	1.0
10	2.1
14	2.5
20	2.8
28	3.0
≥ 50	3.2

Table 10.1: Critical Kutateladze number K_u as a function of dimensionless pipe diameter \hat{D} .

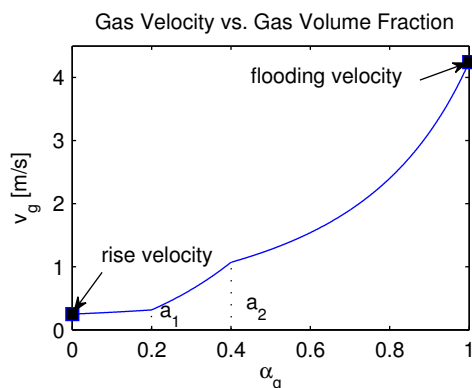


Figure 10.2: Gas velocity vs. volume fraction of gas for zero liquid velocity using SHI slip. Drawn using c1_c2.m in Appendix A.6.

It can be verified from the expression for v_d in (44) that the drift velocity equals the bubble rise velocity when $\alpha_g = 0$ and correspondingly the gas flooding velocity when $\alpha_g = 1$. Figure 10.2 depicts the limit for counter current flow as gas velocity is plotted against gas volume fraction. This limiting gas velocity is determined substituting the drift velocity from (44) into the general slip relation of (1) for when $v_l = 0$ m/s, thus $v_g = \frac{V_d}{1 - C_o \alpha_g}$.

For the numerical representation of this slip relation, please refer to Appendix A.1.

Remark. The slip model could be modified to handle deviated flows through the deviation factor $m(\theta) = \sqrt{\cos(\theta)} (1 + \sin(\theta))^n$, where $\theta = 0$ for vertical flow. The drift velocity is then corrected via $v_{d\theta} = m(\theta) V_{d0}$, where v_{d0} is the drift velocity determined for vertical flow. Hasan and Kabir showed in [5] that the deviation exponent n would take value 1.2 for slug flow in water-air systems.

10.2 Sensitivity Analysis

As the slip model now contains several tunable parameter that can be tuned to fit observations, it is deemed necessary to perform a sensitivity analysis on the different parameters to get a better understanding of how the slip parameters will behave as functions of these. Analysis is based on the base case given in Table 10.2, where sensitivity runs are based on varying a single parameter at a time. Sensitivity runs for C_o and V_d as functions of A , B , a_1 , and a_2 are shown in Figure 10.3. It was also tried running a sensitivity test when varying $F_v = 0.8, 1.0, 1.2$, but this proved to give no variation as mixture velocity was set so low.

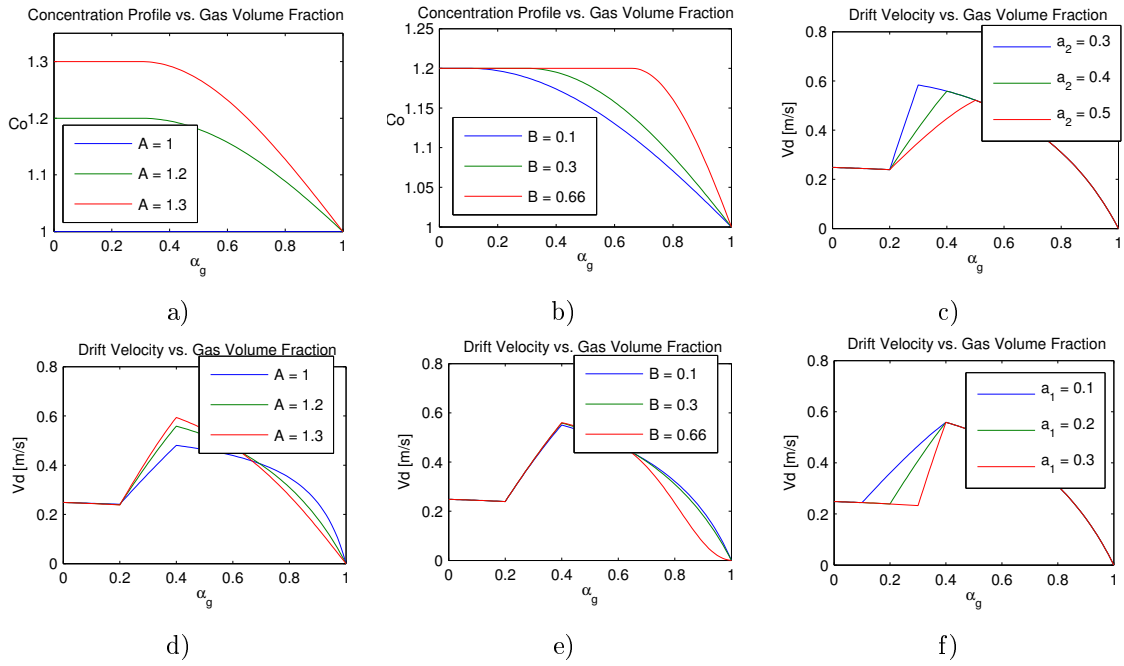


Figure 10.3: Sensitivity runs on profile parameter and drift velocity as functions of gas volume fraction, with basis in base case from Table 10.2. In a) it is noted that $C_o(A = 1) = 1$ for all α_g . Drawn using SHI_c1_c2_ex.m in Appendix A.8.

Table 10.2: Base case used as basis for sensitivity analysis.

Parameter	Value	Description
L	10.9	Length [m]
D	0.1524	Pipe diameter [m]
Δx	0.218	Segment length [m]
ρ_l	1000	Liquid density [kg/m ³]
ρ_g	15	Gas density [kg/m ³]
v_m	1	Mixture velocity [m/s]
σ_{gl}	0.072	Inter-facial tension gas/liquid [kg/s ²]
F_v	1	Tuning Multiplier
A	1.2	Concentration profile parameter
B	0.3	Tuning parameter
a_1	0.2	Start of linear interpolation
a_2	0.4	End of linear interpolation

10.3 Steady State Simulations

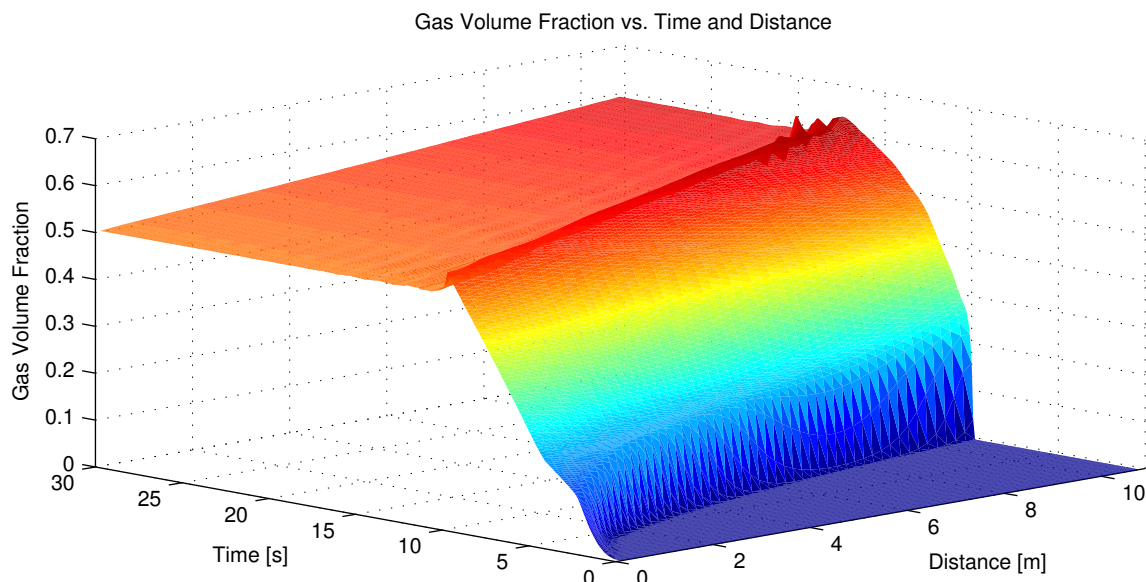


Figure 10.4: 3D plot of gas volume fraction vs. time and distance for flooding and steady state conditions using SHI slip with $Q_g = 61$ [m³/hr] and $WC = 0.04$.

The tunable parameters A , B , a_1 , a_2 and F_v from 10.2 are in [15] optimized to match experimental data from steady-state flows. These experiments are performed in an initially liquid filled pipe in which a set gas- and water volume rate is supplied at the bottom inlet. Equipment located along the flow line determines when steady-state is presents present, the flow is then shut-in and allowed to settle. The

Table 10.3: Experimental and simulated steady-state holdup in vertical gas-liquid flow.

Experimental Values						
Q_g	m^3/hr	WC	$\alpha_{w,exp}$	$\alpha_{g,exp}$	$\alpha_{g,simM}$	$\alpha_{g,simQ}$
12		0.150	0.82	0.18	0.25	0.22
12		0.48	0.83	0.17	0.21	0.19
12		0.78	0.88	0.12	0.15	0.14
12		0.89	0.90	0.10	0.10	0.09
30		0.06	0.68	0.32	0.45	0.40
30		0.26	0.71	0.29	0.40	0.35
30		0.58	0.78	0.22	0.28	0.25
61		0.04	0.49	0.51	0.63	0.55
61		0.15	0.51	0.49	0.58	0.50
61		0.42	0.60	0.40	0.43	0.40

gas- and liquid holdup can then be visibly measured for the given set of inlet flow rates. Simulations using the numerical model is carried out to match the data from experimental holdup, to get better confidence from the model being used.

The experimental setup in [15] is a 10.9 m long 15.24 cm diameter flow loop with instruments along the flow direction flow capable of determining when steady state conditions are met. Nitrogen gas and tap water is being supplied at the bottom inlet via constant volume rates flowing against atmospheric pressure at the top. Once steady state is achieved, fast-acting valves were used to shut the flow loop at top and bottom, and fluids were allowed to settle within the pipe. Volume of nitrogen gas and water are then easily measured, and it is this fractional volume that will be referred to as steady-state holdup.

Experiments were performed for varying injected gas rates at bottom with corresponding varying water cuts. For a given gas volume rate, corresponding water rate is determined using the following definition of water cut

$$WC = \frac{Q_w}{Q_w + Q_g}$$

and thus

$$Q_w = Q_g \frac{WC}{1 - WC}.$$

As these experimental values are only included graphically on page 6 of [15], graphical estimates of these are used in matching simulations to come. The graphical estimates of the experimental values are included in Table 10.3. The optimized drift-flux parameters to be used are $A = 1.4$, $B = 0.0$, $a_1 = 0.1$ and $a_2 = 0.18$. A three-dimensional visualization of gas volume fraction as function of time and distance in a steady state simulation is given in Figure 10.4, where distance is measured from the bottom and up.

Remark (Optimizing tunable parameters). From [15], the tunable parameters are optimized in the following way. Gas holdup is calculated as a function of the tunable parameters by substituting the

definition of superficial gas velocity from (2) into the general slip formulation of (1), so that

$$\alpha_{g,calc} = \frac{v_{sg}}{C_o(\alpha_{g,calc}, A, B, m) + v_d(\alpha_{g,calc}, A, B, a_1, a_2, m)}.$$

As $\alpha_{g,calc}$ is a recursive function, an iterative procedure is used to match experimental data, where the initial guess of $\alpha_{g,calc}$ is the experimental value $\alpha_{g,exp}$.

10.3.1 Steady State Boundary Conditions

For steady state conditions to be applied in the numerical model, the boundary conditions have to be altered. Pressure at the outlet ($i = N + \frac{1}{2}$) is set to atmospheric pressure, allowing fluids to exit the flow loop at the top. At the inlet end, ($i = \frac{1}{2}$), mass flow rates are set to correspond with constant volume rates from experiments.

Since it is the mass flow rates that are entered into the numerical model as a boundary condition, these inlet mass flow rates would depend on pressure in an iso-thermal setting and would consequently vary with time in order to maintain a constant volume rate at inlet. The mass flow rates to be used in simulations are to be defined as

$$\dot{m}_l(p) = \rho_l(p) Q_{l,exp}, \quad \dot{m}_g(p) = \rho_g(p) Q_{g,exp} \quad (45)$$

with corresponding liquid- and gas densities being given by equation (13) and (14).

It turns out that this variance in inlet boundary conditions brought to life some propagating instabilities after gas has broken through the outlet end. To avoid this instability, the mass influx of gas and water was first made invariant of the inlet pressure by assuming constant hydrostatic pressure through $p = p_0 + \rho_{l,0}gh$. Results using this assumption are compared with experimental data in Figure 10.5, where data points landing on the 1 : 1 line indicates a perfect match between simulated and experimental data.

The reader should bear in mind the error that goes with assuming constant mass flow rates would lead to over estimating the inlet volume rates over time (as inlet pressure in reality would decrease as more gas is injected), and subsequently over estimating the steady state holdup of gas. When looking Figure 10.5, it is noted that the points deviating the most from the 1 : 1 line are for simulations with high Q_g and low corresponding WC . This is also seen from Table 10.3.

As it is believed that the assumption of constant mass influx will tend to over estimate the gas holdup in simulations when comparing with physical experiments. It is therefore desirable to be able to have a varying mass influx of the phases to maintain a constant volume rate and better adhere with experiments. To achieve this, it proved that multiplying the frictional term of equation (11) by a factor of 3 dampened the pressure oscillations after breakthrough and thus led to more stable simulations. Implementing this modification prevents pressure oscillations at outlet from affecting the inlet pressure in such a degree as to cause instabilities. See Figure 10.9 where both inlet and outlet pressure is plotted over time for three different cases in order to determine how to best avoid instabilities in solution. Multiplying the friction term by a factor of 3 is what is used when comparing simulated results with experiments in Figure 10.6.

From Figure 10.6 it appears the model is able to reproduce experimental steady state results fairly well with a root mean square error of only 0.039. It is important to remember that the model only uses the most basic of pressure- and friction relations and is still able to produce reliable results. This provides a better confidence of the slip model as well as a viable starting point for applying the same slip relations in transient (non-steady state) simulations in Section 11.

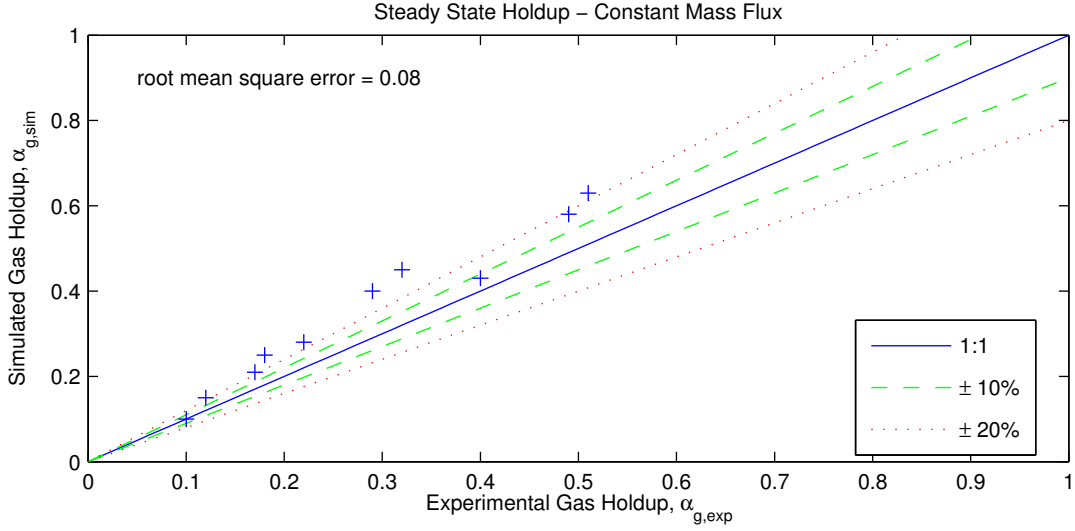


Figure 10.5: Simulated steady state holdup data versus experimental data from H. Shi et al., [15]. Slip parameters used are $A = 1.4$, $B = 0.0$, $a_1 = 0.1$ and $a_2 = 0.18$. The figure is plotted using `holdup_results.m` in Appendix A.7.

It must be remembered that the frictional pressure drop calculations determined within the numerical model is originally to be used for laminar flow only. It is suspected that turbulent flows may occur at high gas volume rates and as such, the determination of frictional pressure drop should account for this possibility and therefore be a function of dimensionless Reynolds number to quantify the transition from laminar to turbulent flow.

I.e for one of the three cases with high gas volume rates, $Q_g = 61 \text{ m}^3/\text{hr}$ and $WC = 0.04$, the simulation run is shown in Figures 10.7 and 10.8. A quick calculation of the Reynolds number at the end node for $t = 30\text{s}$ yields $Re = \frac{\rho_m v_m D}{\mu_m} = 4366$, indicating turbulent flowing conditions. When transitioning from laminar to turbulent flow, the friction factor is decreased (i.e see the Moody friction factor chart of [3]). As it is not transparent what will happen with the phase velocities when transitioning into turbulent flow, it is not a given what would happen to the the frictional pressure drop as the friction factor decreases. The reader is reminded of the Darcy-Weisbach relation used in determining frictional pressure drop $F_w = \frac{1}{d} f \frac{1}{2} \rho v |v|$. It is expected that accounting for turbulent flows would affect the simulation runs for high gas rates, i.e the points deviating the most from the 1 : 1 line of Figure 10.6, and should be investigated further.

Remark. Instead of multiplying the friction term by a factor to get rid of the oscillations after breakthrough, an equivalent method would be to either increase the length of the pipe or reduce the diameter, thus increasing the total frictional pressure drop which also would lead to dampened effect on pressure oscillations. This would however not coincide with the physical experiment.

10.3.2 Simulation Run

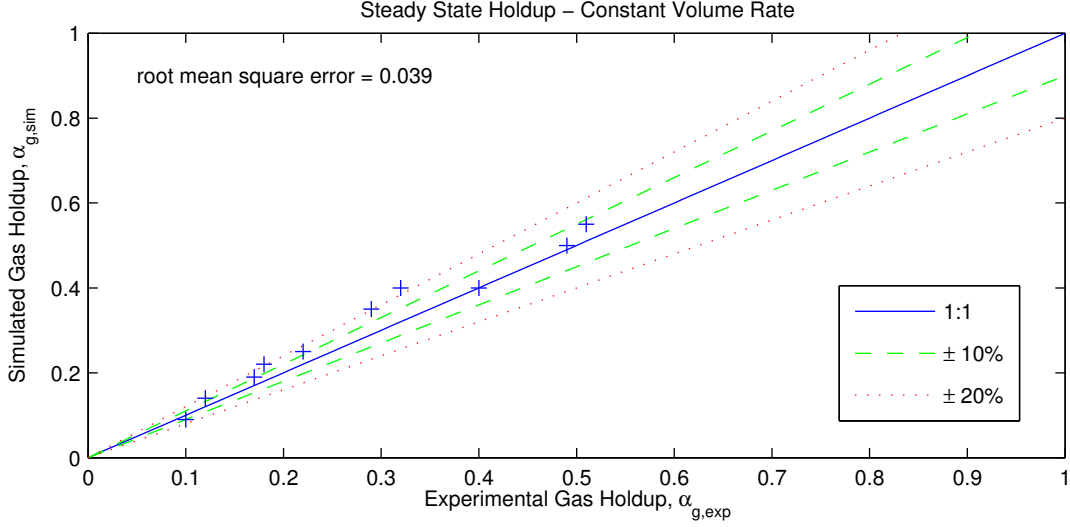


Figure 10.6: Simulated steady state holdup data versus experimental data from H. Shi et al., [15]. Slip parameters used are $A = 1.4$, $B = 0.0$, $a_1 = 0.1$ and $a_2 = 0.18$. The figure is plotted using MATLAB routine holdup_results.m.

A simulation run when flowing an initially liquid filled pipe with $Q_g = 61 \text{ m}^3/\text{hr}$ and $WC = 0.04$ is given in Figures 10.7 and 10.8. To maintain a constant volume rate at inlet, the mass flow rates are determined from (45). The mass rates are allowed to be ramped up within the first 10 seconds via a ramping function y bearing the properties $y(t = 0) = 0$ and $y(t = 10) = 1$. From Figure 10.7 it is seen how the gas is distributed over the pipe length for the flooding process until steady-state has been achieved for $t = 30 \text{ s}$. From Figure 10.7 the effect of gas expansion is clearly seen when $t = 30 \text{ s}$ as $\alpha_g(\text{node1}) \approx 0.50$ and $\alpha_g(\text{nodeN}) \approx 0.60$. The corresponding steady-state gas holdup is then calculated by numerical integration of the volume fraction via

$$\alpha_{g,sim} = \frac{1}{L} \sum_{i=1}^N \alpha_{g,i} \Delta x_i.$$

Figure 10.8 a) illustrates the pressure distribution within the pipe for the same set of times. From the figure it is easy to distinguish the pressure gradient of liquid from that of the mixture for times 6 and 8 seconds. After the gas has broken through on top for times 10 and 30 seconds, only the mixture pressure gradient is present.

Liquid velocities in Figure 10.8 b) shows that the liquid velocities are steadily increasing the first ten seconds before stabilizing at steady-state velocity at $t = 30 \text{ s}$. This increase/decrease effect is related to the inlet volume rates still being ramped up. For times $t = 6, 8 \text{ s}$ it is also observed that the liquid velocity is lower in the two-phase region than in single-phase liquid. This can be explained by the effect of how both the injected gas and liquid will tend to drive forward the liquid initially in place and thus give it an added velocity coming from the gas. The overall frictional pressure gradient is also decreased as the initial liquid is expelled. Velocities determined at $t = 30 \text{ s}$ can be verified to be in agreement with steady state conditions by assuming constant mass flow rate, $\dot{m}_{in} = \dot{m}_{out}$ when

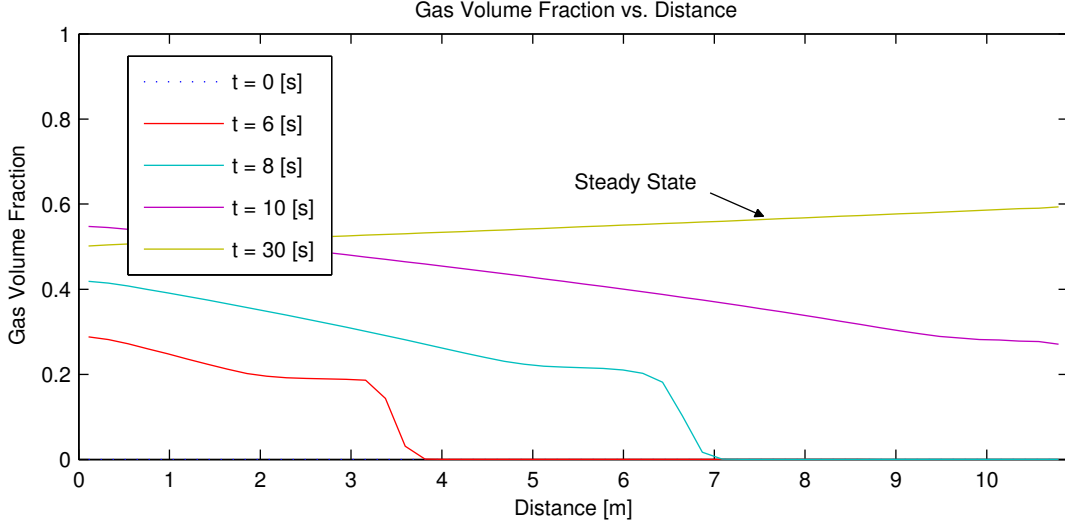


Figure 10.7: Gas volume fraction versus distance for steady state simulations with inlet gas volume rate $Q_g = 61 \text{ m}^3/\text{hr}$ and water cut $WC = 0.04$ using SHI slip relation.

knowing the fluid distribution, the pipe area and the pressure along the pipe.

From Figure 10.8 the gas velocities are shown as functions of distance. Remembering that gas velocity is determined from equation (28), it is not unexpected that gas velocities are determined regardless of whether or not the phase is present. For times 6 and 8 seconds it is seen from Figure 10.8 c) that there is a sudden decrease in velocity profile as $\alpha_g \rightarrow 0$ and $v_g(\alpha_g \rightarrow 0) \approx C_o v_l + v_d$. It is observed that the gas velocity decreases when going from ten to thirty seconds.

When comparing the fluid velocities with the slip parameters before breakthrough from Figure 10.8 d) and e), there seems to be a distinct coupling between the gas- and drift velocity as well as with the liquid velocity and the concentration profile parameter. The reason for this is easier to see when remembering that velocities are determined from

$$v_l = \frac{u_3(1 - C_o\alpha_g) - u_2v_d}{u_1(1 - C_o\alpha_g) + u_2C_o\alpha_l}, \quad v_g = \frac{u_1v_d + u_3C_o\alpha_l}{u_1(1 - C_o\alpha_g) + u_2C_o\alpha_l}.$$

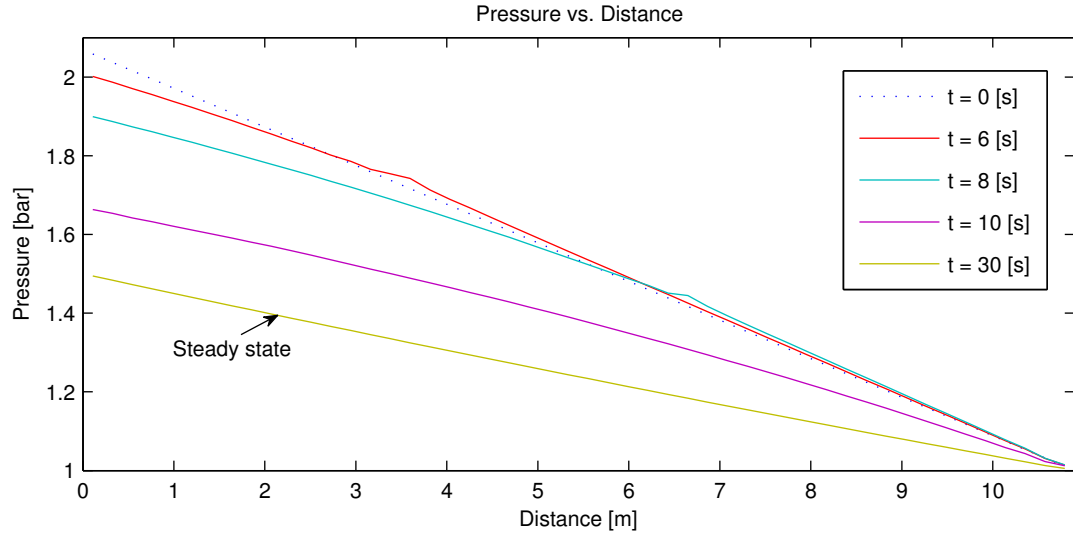
For times when the slug is visible within the pipe, i.e not broken through the outlet end, the term $u_3(1 - C_o\alpha_g)$ will tend to be much greater than u_2v_d in the numerator for liquid velocity. Correspondingly for gas, the numerator term u_1v_d will be much greater than $u_3C_o\alpha_l$. This gives rise to v_l having a stronger connection with C_o while v_g has a stronger connection with v_d . This coupling between velocities and slip parameters is even more distinct when simulating the migration of a gas slug in Section 12 and 13.

Source of Instability in Steady State Simulations

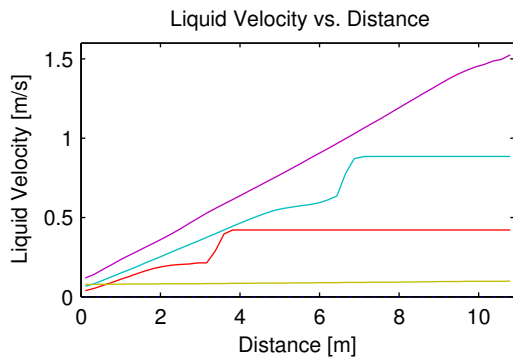
This section is included to further study the instabilities encountered in steady-state simulations when not modifying the frictional pressure drop. From Figure 10.9 it is seen a major oscillation in pressure

at the top node when gas is breaking through at the top. The inlet pressure does not seem to notice this pressure surge until a bit later. This is to be expected as the sound velocity for the mixture should average about ≈ 20 m/s and thus the pressure pulses should travel from top to bottom of the 10.9 m flow line in about 0.5 s. One can see from the figure that the pressure at the top node stabilizes at a lower pressure than before gas has broken through. This is caused by the fact that when gas has managed to surpass all liquid in front of it, the frictional pressure drop is greatly decreased and thus the pressure at the top node is much closer to outlet pressure 1 bar at $i = N + \frac{1}{2}$. Three cases dubbed “1fric”, “1fric constmassflux” and “3fric” are introduced. The case “1fric” will represent the default case with normal friction term and varying mass flow rates at inlet to accommodate for constant volume rates. Case “1fric constmassflux” has the friction term remain unchanged, but the inlet mass flow rates has been made invariant of pressure. “3fric” is identical to “1fric” except the frictional term has been multiplied by a factor of 3.

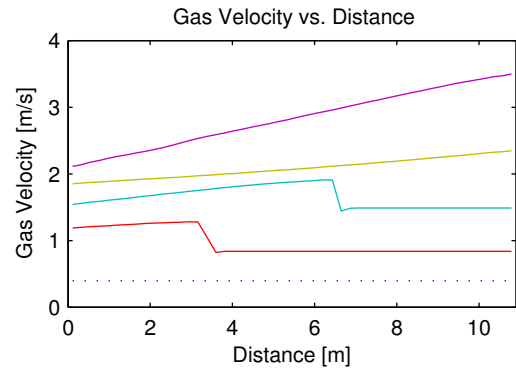
For a total set of 50 nodes, node 30 has been selected to see how the liquid- and gas mass flow rates vary with time. Center of the node is situated about 6.431 m from bottom with node thickness of $\Delta x = 0.218$ m. The fact that more liquid and gas is injected when assuming constant mass flow rate is easily seen from Figure 10.10 b).



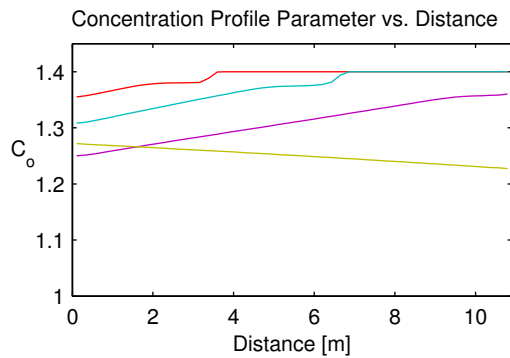
a)



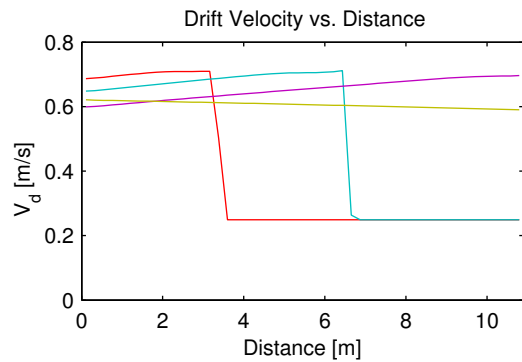
b)



c)

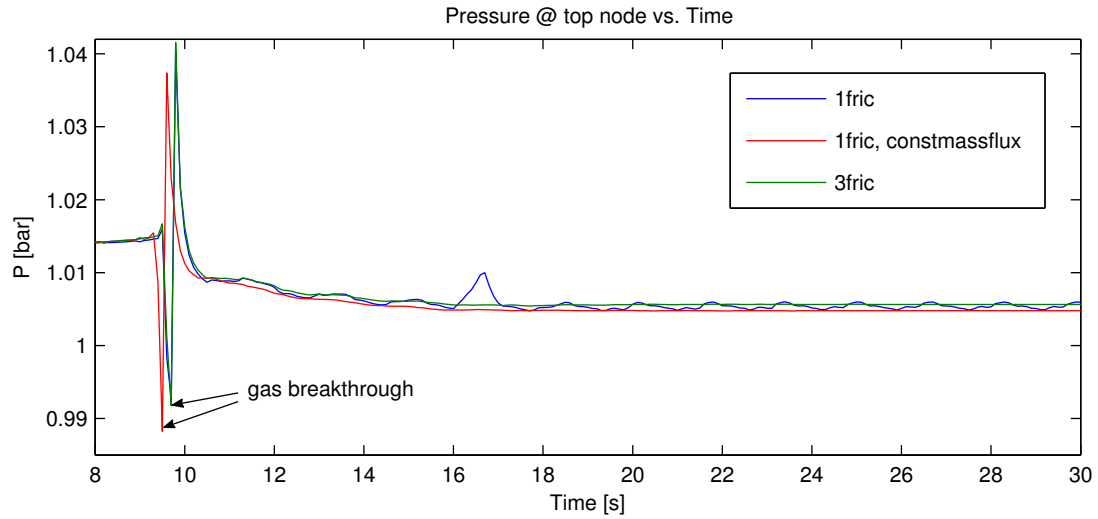


d)

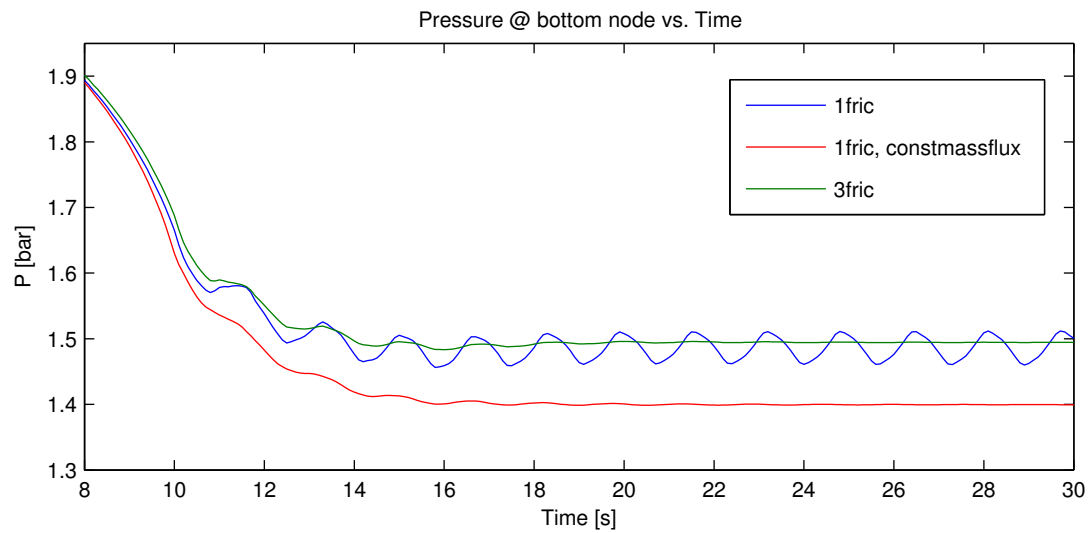


e)

Figure 10.8: Simulation run for steady state simulations with inlet gas volume rate $Q_g = 61 \text{ m}^3/\text{hr}$ and water cut $WC = 0.04$ using SHI slip relation for times $t = 0, 6, 8, 10, 30 \text{ s}$.

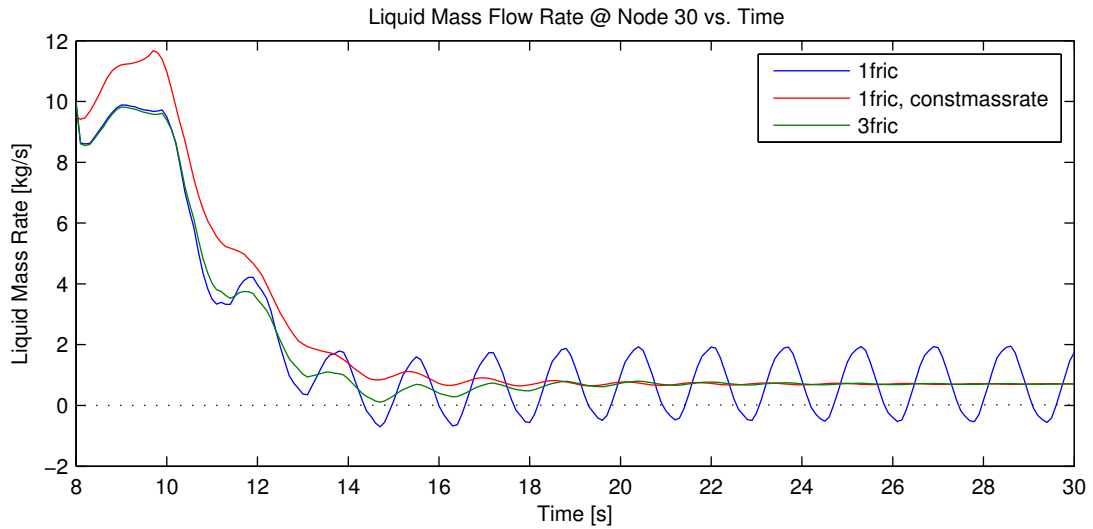


a)

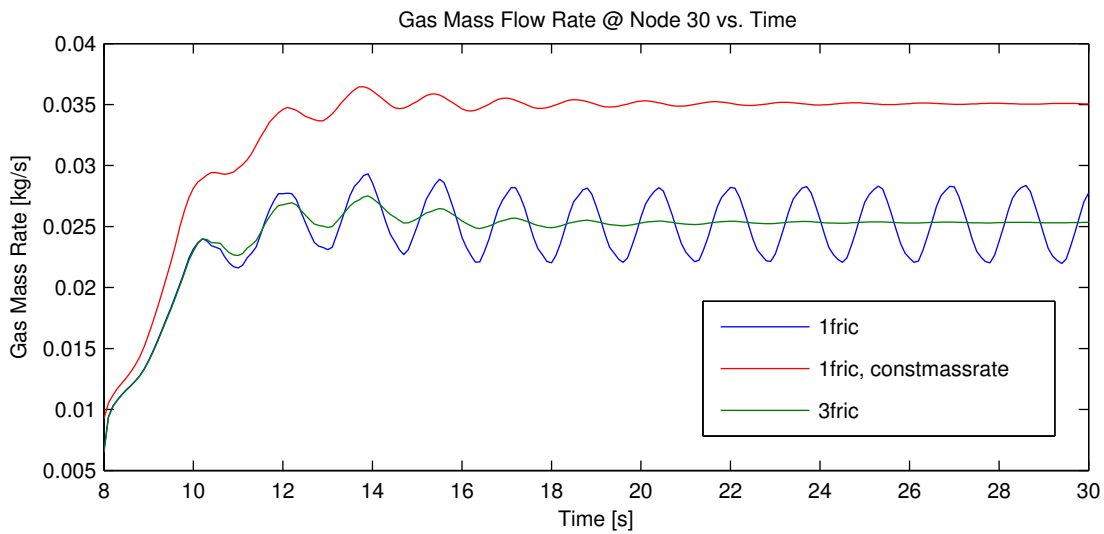


b)

Figure 10.9: Case study of pressure vs. time for three cases. Case of standard friction term and varying mass rates (1fric), case of 3 times the standard friction term and varying mass rates (3fric), and case of standard friction term and constant mass rates (1fric, constmassflux).



a)



b)

Figure 10.10: Case study of mass flow rates vs. time in steady-state simulations for three cases. Case of standard friction term and varying mass rates (1fric), case of 3 times the standard friction term and varying mass rates (3fric), and case of standard friction term and constant mass rates (1fric, constmassflux).

11 Transient Simulations

To limit the expected flow patterns to a minimum, a gas slug is placed near the bottom of a 10.9 m pipe and allowed to migrate to the closed top solely due to buoyancy. This makes it reasonable to expect that the gas will flow similar to that of slug flow. The initial gas slug is placed between 1 and 2 m from the bottom while the pipe is shut at the top, and given an initial gas volume fraction of $\alpha_{g,0} = 0.99$. Besides the gas slug, the pipe is initially filled with liquid and initial shut-in pressure at top equals atmospheric pressure, 1.0 bar. The slug is set free as simulation starts. As the slug migrates towards the top it will be constrained from expanding and the overall pressure within the pipe will gradually increase until the gas has sufficiently accumulated and settled at the top.

Initial slip parameters $C_{o,0}$ and $v_{d,0}$ are the same that are being used in Section 12 with zero initial liquid velocity throughout the pipe. Initial gas velocity is then determined to be compliant with the general slip law, thus

$$v_{g,0} = \frac{v_d}{1 - C_{o,0}\alpha_{g,0}}.$$

11.1 Short Pipe

Short pipe simulations will be performed in accordance with physical experiments in Section 10.3 in which a pipe of length 10.9 m and 15.24 cm diameter has been used.

12 Transient Simulations with Simple Slip

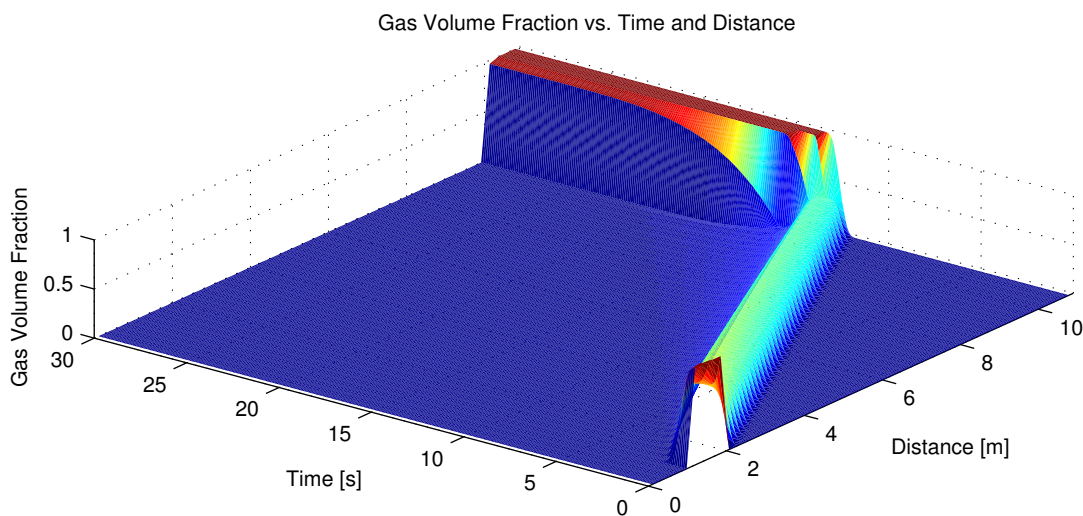


Figure 12.1: 3D plot of gas volume fraction versus time and distance for a migrating gas slug using the simple slip relation.

These simulations are included to have something to evaluate the SHI slip simulations in Section 13 against. Figure 12.1 shows how the gas is distributed as functions of time and distance when the

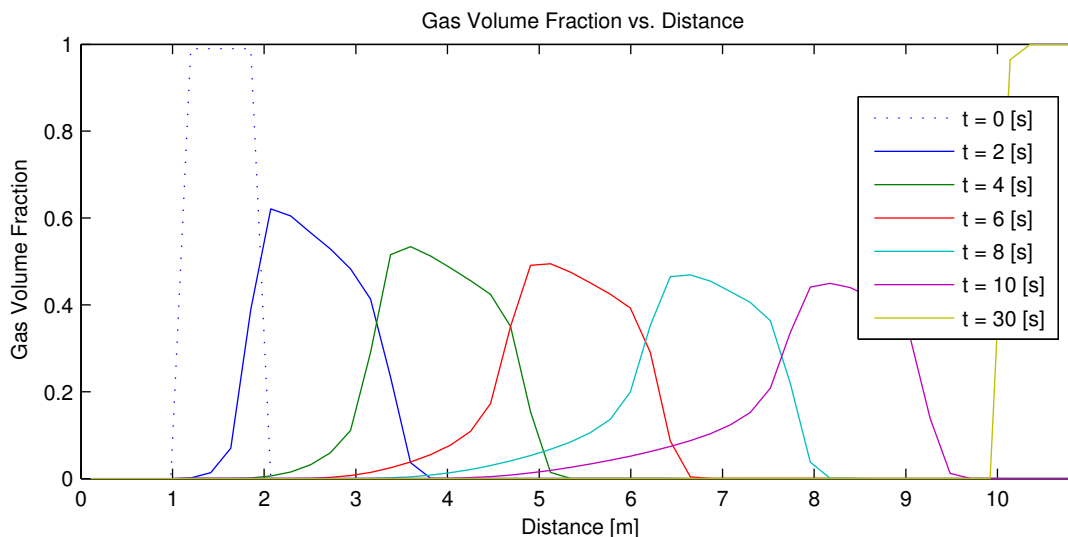


Figure 12.2: Gas volume fraction versus distance in a transient simulation of a migrating gas slug using the simple slip relation.

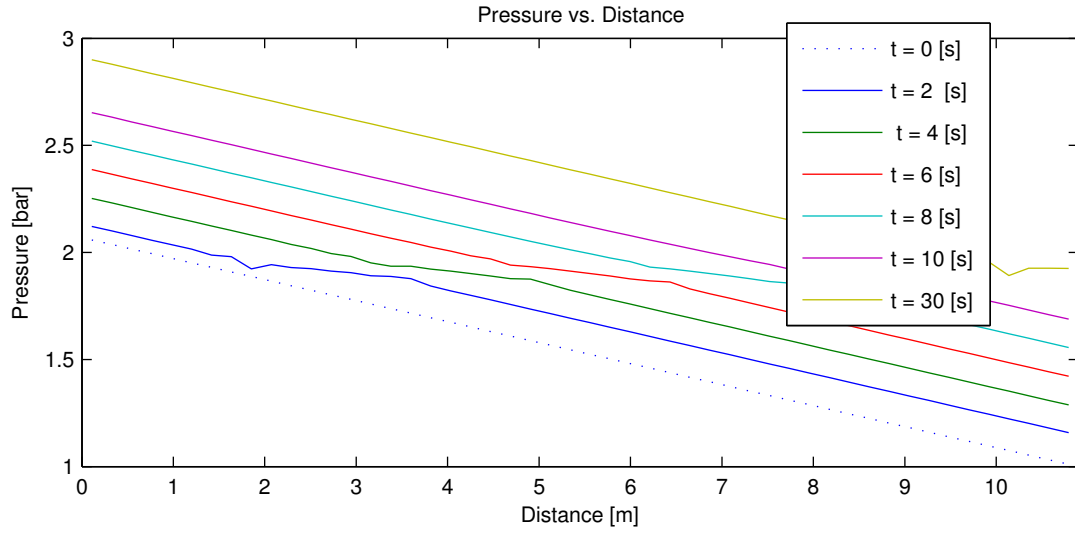
gas slug migrates towards a closed outlet. Distance is measured from the bottom and up. The reader is reminded of the slip parameters relation to velocities through equation (1). What will from now on be referred to as the simple slip, is the slip parameters given by

$$\begin{aligned} C_o(\alpha_g) &= 1.2 - 0.2\alpha_g \\ V_d(\alpha_g) &= 2(\alpha_g + 0.2)(1 - \alpha_g) \end{aligned} \quad (46)$$

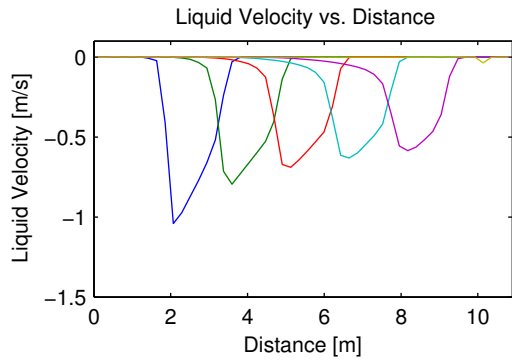
These slip parameters are designed so that $C_o(\alpha_g \rightarrow 1) = 1.0$ and $V_d(\alpha_g \rightarrow 1) = 0$ m/s to coincide with no-slip single-phase flowing conditions without the need for interpolation when $\alpha_g \rightarrow 1$. Even though these parameters are not directly based on experimental observations, they are designed to operate within a reasonable range for such parameters and not give way for unphysical behavior.

It is seen from Figure 12.2 what happens with the gas as it migrates towards the top of the pipe for times $t = 0, \dots, 30$ s. The gas slug seems to be leaving a growing trail of gas behind it, making it reasonable to think that the slug is moving faster than trail of gas behind it, which otherwise would have caught up with the slug. This seems to not be analogous with how a typical Taylor bubble would ascend the pipe, as it would to a large extent form one big bubble with a little trail of bubbles behind it traveling at a higher velocity and eventually catching up with it. It is however to be noted that the gas volume fraction gives no direct information about what flow regime is present, only the phase distribution is given.

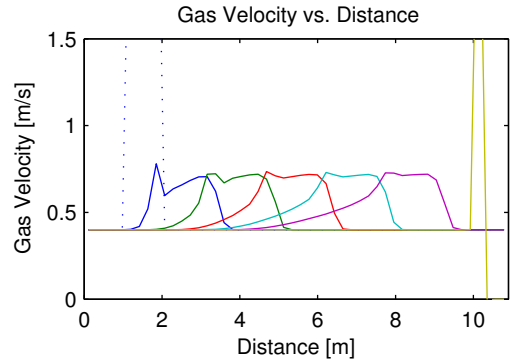
From Figure 12.3 a), the corresponding pressure gradient versus distance is given. For times $t = 2, 4, 6, 8$ s it is easy to see where the gas is present from the figure, as the pressure gradient seen to be less steep in this region. Overall the pressure is seen to increase steadily throughout the pipe until all gas has settled at the top.



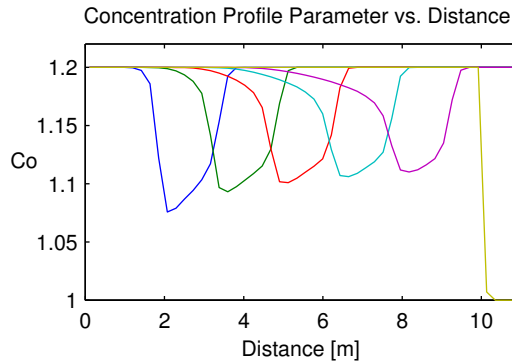
a)



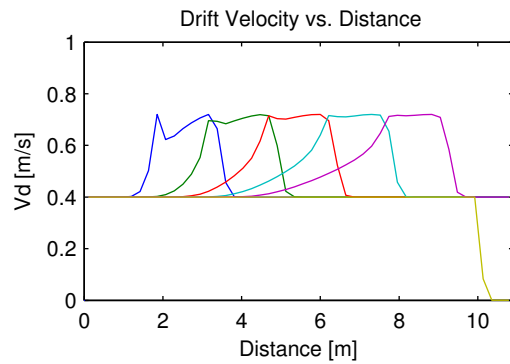
b)



c)



d)



e)

Figure 12.3: Simulation parameters for a migrating gas slug using the simple slip relation. It is the times $t = 0, 6, 8, 10, 30$ s that have been shown.

Liquid velocities were found to be either zero or negative for all positions within the pipe during the simulations as can be seen in Figure 12.3 b). This is related to the liquid initially being still when the slug is released, and thus forced to flow in the negative direction to allow the gas to pass. As the gas slug diminishes over time, the decrease in liquid velocity is expected. Comparing the concentration profile parameter in Figure 12.3 d) with the liquid velocity there seems to be a strong coupling between them. The evolution of C_o for different times resembles the liquid velocity at corresponding times quite a bit.

Gas velocities in Figure 12.3 c) are higher in the front than at the trailing end, consistent with what was concluded from watching the gas volume fractions development along the pipe. Even though the gas volume fraction in front seen to diminish over time, the front velocities are seen to remain fairly constant, and are only a bit higher than the drift velocity throughout. As was said previously about the coupling between the profile parameter and the liquid velocity, can also be said about the drift velocity and the gas velocity. Looking at Figure 12.3 c) and e) the coupling between them is even more pronounced than for liquid velocity and C_o . It should be noted for further reference that at low gas velocities, v_g will tend to be more a function of v_d as v_l will be of C_o .

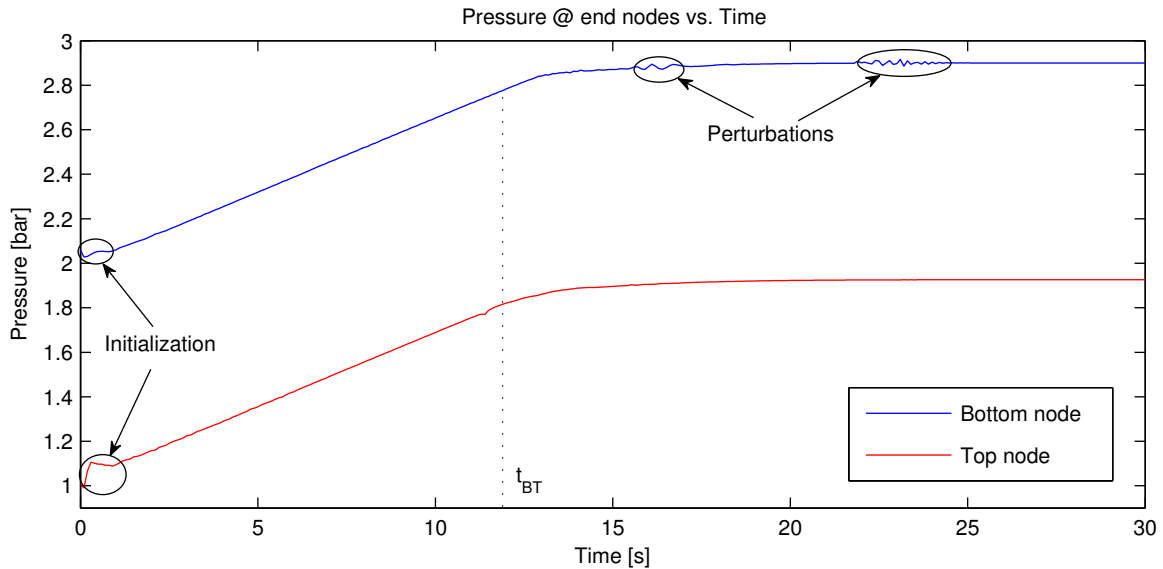


Figure 12.4: Pressure at the end nodes versus time in a transient simulation of a migrating gas slug, where the simple slip relation has been used.

Figure 12.4 shows how the top- and bottom node pressures changes over time. The pressure is seen to increase linearly with time until some time after the gas breaks through on top at $t_{BT} = 11.9$ s, when this steady increase comes to a halt and the pressure eventually flattens out. At early times, some inconsistencies can be seen in the end node pressures, identified by “initialization” in figure. This pressure response is solely related to the system not being quite at equilibrium with itself from the initial conditions. Some perturbations are visible in the bottom node pressure at $t \approx 16$ s and $t \approx 23$

s. It is believed that these pressure perturbations might originate from the gas-liquid interface moving downwards as more gas is accumulating on top. Increasing the number of nodes to 100 proved to have little or no effect on the end-node pressures. Similar perturbations are also visible when using the SHI slip of Section 13, although the magnitude is seen to be quite different. Had incompressible liquid been assumed, the end node pressures should have increased by $\Delta p = 1.059$ bar. Instead, the end node pressure now converges towards $p_{top} = 1.926$ bar and $p_{bot} = 2.900$ bar, thus a differential pressure of $\Delta p = 0.974$ bar is obtained.

13 Transient Simulations with SHI Slip

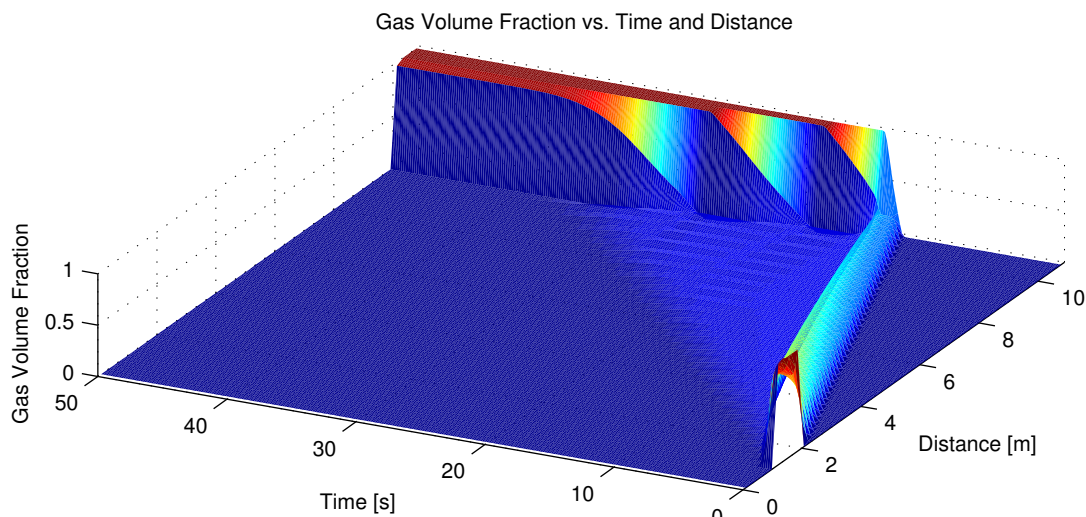


Figure 13.1: Three-dimensional plot of gas volume fraction versus time and distance for a migrating gas slug towards a closed outlet, where the SHI slip relation has been used.

As transient gas migration simulations using the simple slip was concluded, similar simulations needed to be carried out using the SHI slip from Section 10. In order for all the gas to properly settle on top, simulations needed to run for 50 seconds instead of 30 as for the simple slip. The three-dimensional plot of the gas volume fraction versus time and distance in Figure 13.1 shows how the gas is distributed in the pipe.

When viewing gas volume fraction versus distance in Figure 13.2 it is seen that the gas slug starts to develop a tail early on which keeps growing until the gas breaks through at top. Subsequently the gas volume fraction of the gas front experiences a considerable decline. This development of a tail is suspected to be directly related to the interpolation parameters a_1 and a_2 described in Section 10. The position of the gas front from Figure 13.2 seems to correspond well with Figure 12.2 when using the simple slip, and as such breaks through on top only 0.93 s later. What takes considerable time for simulations to conclude is waiting for the developed gas trail behind the front to sufficiently accumulate on top.

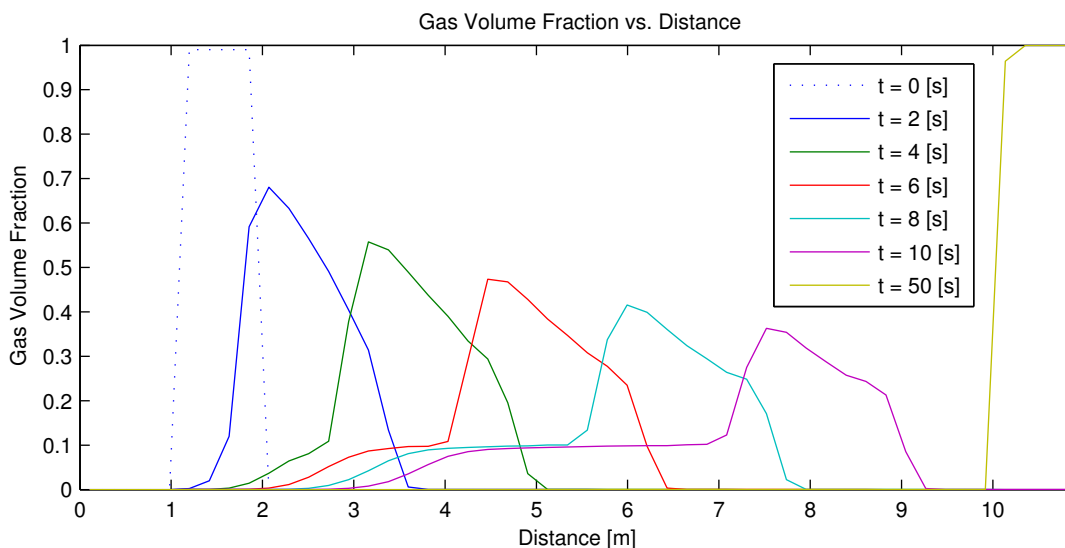


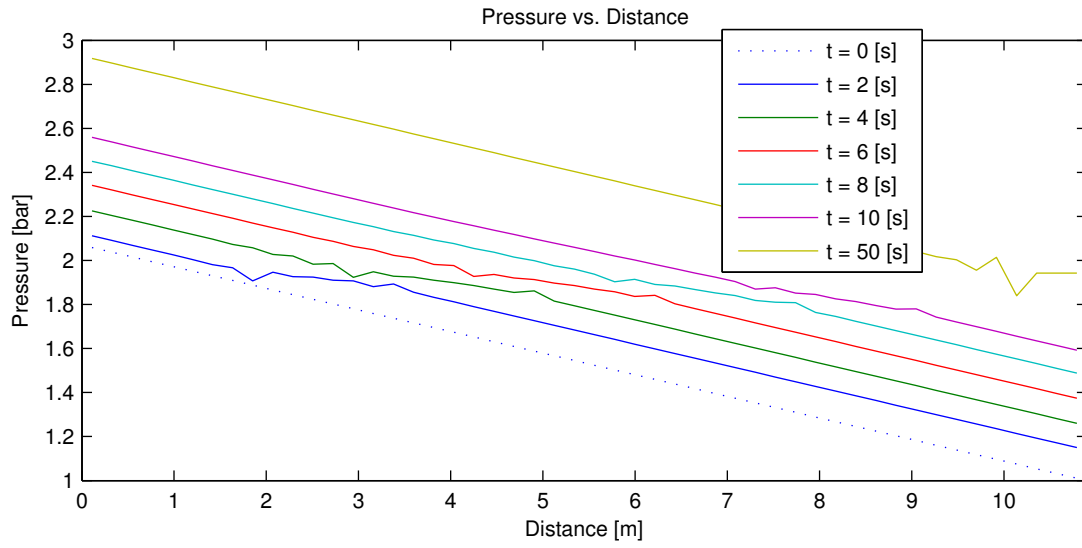
Figure 13.2: Gas volume fraction versus distance for a migrating gas slug using SHI slip relation.

Figure 13.3 a) shows the pressure gradient within the pipe. As for the simulation run using the simple slip, it is easy to see when and where the mixture gradient is present for times $t = 2, \dots, 10$ s. The mixture gradient is seen to be steeper for most times as the gas is more evenly distributed along the pipe.

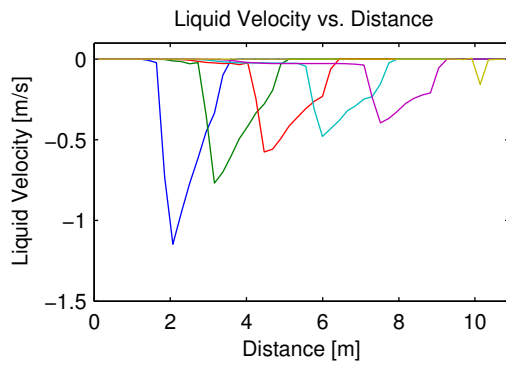
Distinct shapes in the velocity profiles for liquid and gas from Figure 13.3 b) and c) is also seen in the corresponding slip parameters in d) and e). Having knowledge of the velocities dependence on respective slip parameters, seems to be an excellent starting point if a transient slip is to be designed based on transient experimental data in future work.

End node pressures over time are given in Figure 13.4 where the end node pressures using the simple slip from Figure 12.4 are also included. As for the simple slip, pressure incline is seen to remain fairly linear until a bit after breakthrough at $t_{BT} = 12.83$ s on top when the incline comes to a halt and the pressures flatten out. Pressure perturbations are also seen here as for the simple slip, however the magnitude is seen to have increased. Slight perturbations are also seen in top node pressure. When comparing pressures using the simple slip with those of the SHI slip in Figure 13.4, the simple slip is seen to have a much steeper incline in pressure. This is a direct effect of the gas fraction when using the simple not being spread out as much over the pipe length, thus more gas is situated at the front trying to expand against the nearly incompressible liquid leading to an added increase in pressure at the given time.

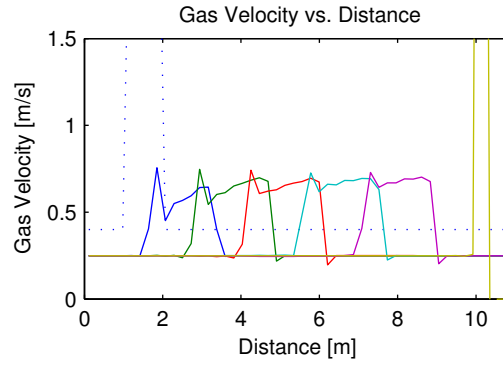
Remark. It is to be noted for simulations that the model faired with some numerical difficulties as the gas was starting to accumulate at the top. This difficulty is especially evident when looking at gas volume fraction for times $t = 14, \dots, 25$ s in Figure 13.5. The gas fraction is seen to start oscillating after $t = 14$ s when the gas-liquid interface starts moving downwards. It is believed that some of the pressure perturbations seen within the end nodes in Figure 13.4 is related to the numerical issues happening when gas is accumulating at top. A further study of this is included in Section 13.2 where the same simulation is run for 25 and 100 nodes.



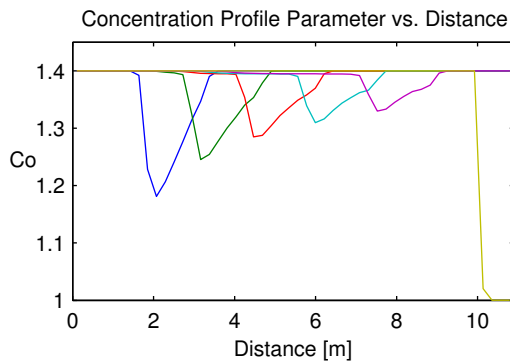
a)



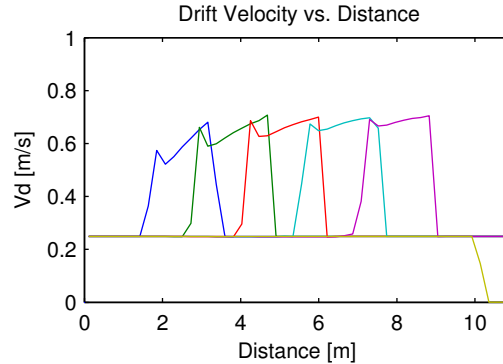
b)



c)



d)



e)

Figure 13.3: Simulation parameters for a migrating gas slug using SHI slip relation. The times $t = 0, 2, 4, 6, 8, 10, 50$ s are shown.

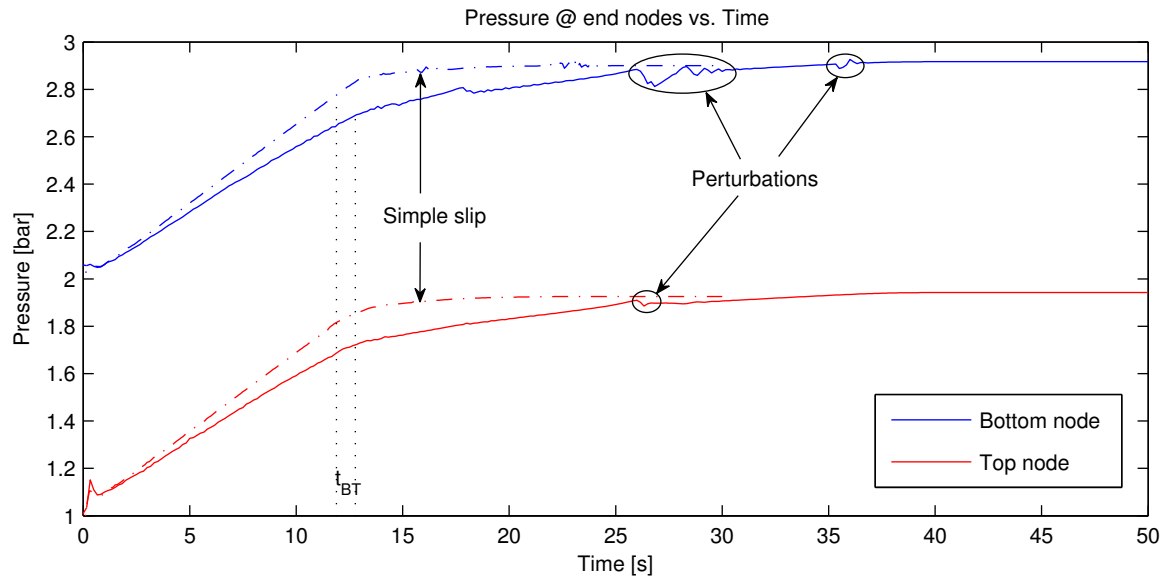


Figure 13.4: Pressure at top- and bottom node versus distance for transient gas migration simulation using SHI slip relation.

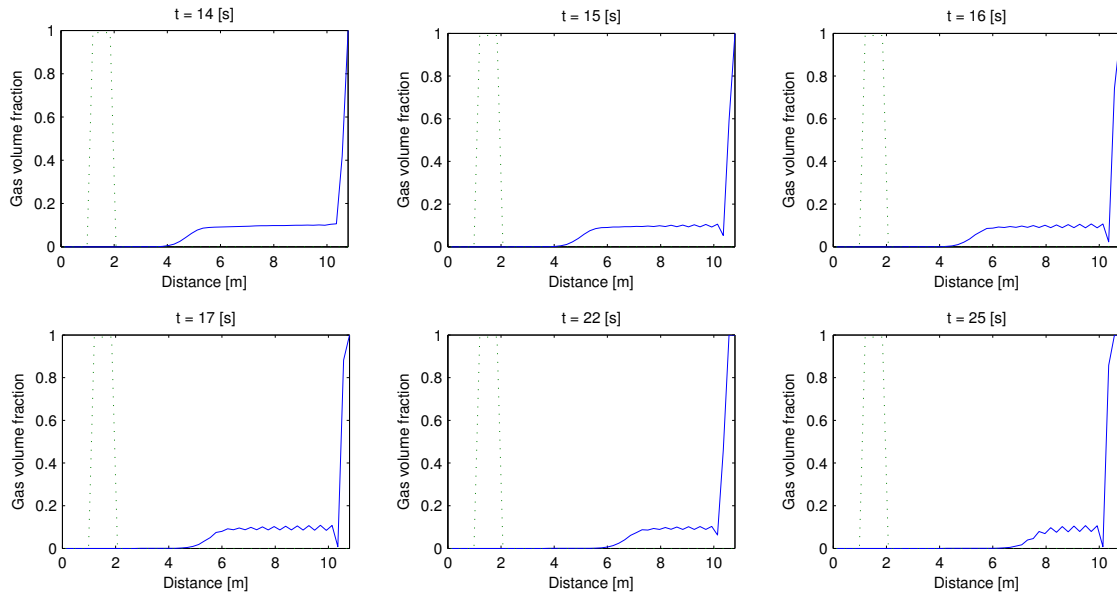


Figure 13.5: Gas volume fraction versus distance in a transient simulation with the SHI slip relation. Illustration of an unphysical behavior using SHI slip as increasing amounts of gas is accumulating at the top, where times $t = 14, 15, 16, 17, 22, 25$ s have been selected for this purpose.

13.1 Objective Function

The tuning parameters for SHI slip implemented in Section 10.3 and 13, $A = 1.4$, $B = 0.0$, $a_1 = 0.1$ and $a_2 = 0.18$, are not unique in the sense that these parameters are the only ones minimizing the objective function, i.e the difference between theoretical and experimental results in [15]. Here it is reported that a different set of parameters for vertical flow of $A = 1.2$, $B = 0.6$, $m = 1.28$, $a_1 = 0.05$ and $a_2 = 0.13$ also gives a minimum in the objective function, thus approximately the same steady-state holdup results. The keen reader may notice that the deviation factor m is included even though the flow is vertical. This multiplier of the drift velocity is now set constant, no longer a function of the deviation angle θ from vertical (as that would give $m = 1$). A simulation run identical to the one done previously is carried out using this new set of tuning parameters.

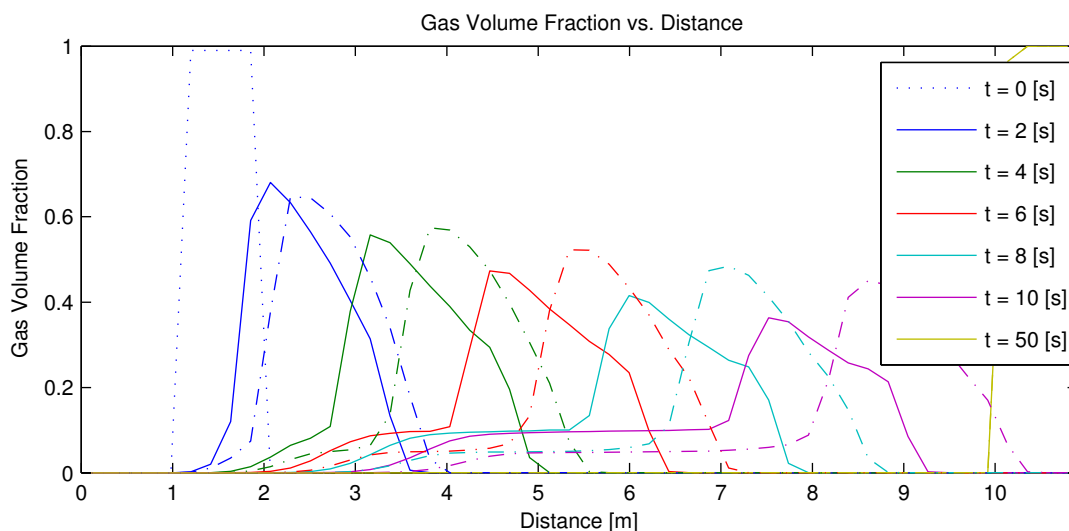


Figure 13.6: Comparison of gas volume fraction versus distance at different times for different set of SHI slip tuning parameters. Solid lines have $A = 1.4$, $B = 0.0$, $m = 1.0$, $a_1 = 0.1$ and $a_2 = 0.18$ while dashed lines have $A = 1.2$, $B = 0.6$, $m = 1.28$, $a_1 = 0.05$ and $a_2 = 0.13$,

A comparison of volume fractions from Figure 13.2 with the ones obtained in the latest simulation is included in Figure 13.6. From the figure it is seen that this new set of tuning parameters causes the gas volume fraction of the front to maintain a higher value over time, while the trailing gas is kept at a lower value. Breakthrough time is also decreased with the new set of tuning parameters, an effect originating in the drift velocity being multiplied by a factor of $m = 1.28$. Tuning parameter a_1 seems to have a major impact on the gas volume fraction trailing behind the gas front. This is evident from Figure 13.6 where both $a_1 = 0.05$ and $a_1 = 0.10$ have been used, and it is seen for the respective set of tuning parameters that the gas volume fraction of the trailing gas roughly equals the value assigned to a_1 .

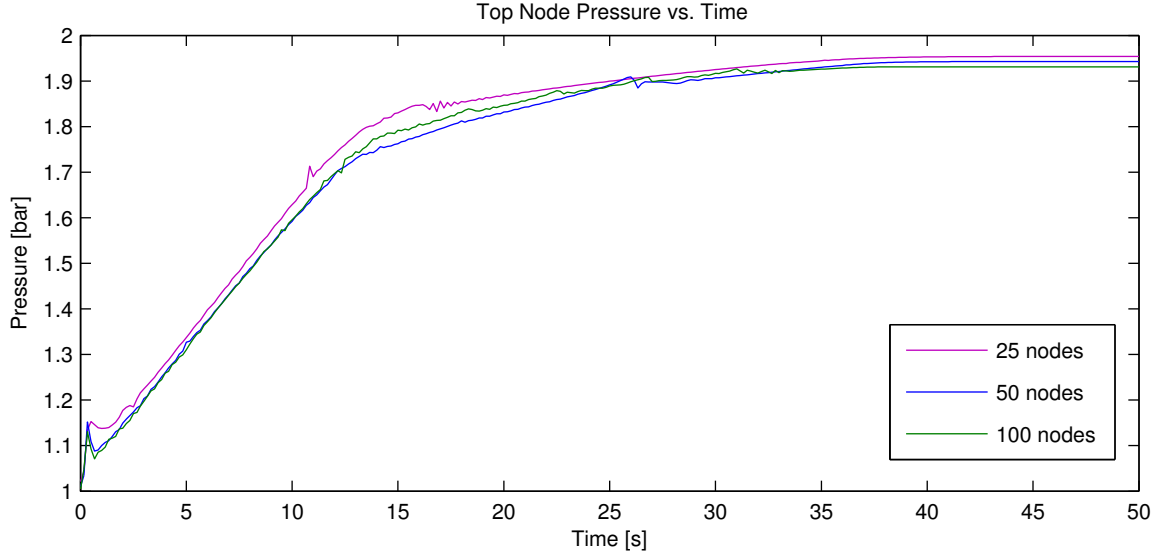


Figure 13.7: Top node pressure versus time for different node settings in transient simulations with SHI slip relation.

13.2 Simulation Node Comparison

It appears that when using SHI slip, the model crashes depending on which node setting is in use. I.e a gas migration simulation with 25 and 100 nodes work fine while one with 50 nodes crashes. This seem to be a problem originating at the top node as the conservative variables suddenly becomes incomputable. This causes the following flux parameters to be incomputable and thus the whole model breaks down. This issue was solved setting a weaker criterion for when single-phase gas and no-slip is present when determining velocities. The new criteria are as follows

$$v_g = \begin{cases} \frac{u_3}{u_2}, & \alpha_g > 0.9999 \\ \frac{u_1 v_d + u_3 C_o \alpha_l}{u_1 (1 - C_o \alpha_g) + u_2 C_o \alpha_l}, & \text{otherwise} \end{cases} \quad v_l = \begin{cases} v_g, & \alpha_g > 0.9999 \\ \frac{u_3 (1 - C_o \alpha_g) - u_2 v_d}{u_1 (1 - C_o \alpha_g) + u_2 C_o \alpha_l}, & \text{otherwise} \end{cases} .$$

When simulating the case with 50 nodes in Figure 13.4 it is observed some oscillations in the pressure, particularly the bottom node pressure after gas has broken through. As it was unclear whether this was a physical or a numerical effect, it was tried simulating the same case for different node settings of 25 and 100 nodes as shown in Figure 13.7 and 13.8. Pressure oscillations seem to increase with the number of nodes being used, indicating that this is a numerical effect, as the use of less nodes will smear out these effects. This appears to be an issue originating at the top, as the oscillations are seen to increase in magnitude towards the bottom node. It is believed that this is an issue related to the somewhat unphysical behavior of the system described in Figure 13.5, whereas the SHI slip relation may cause the drift-flux model fail to remain hyperbolic, as small perturbations in pressures are seen to grow within the system.

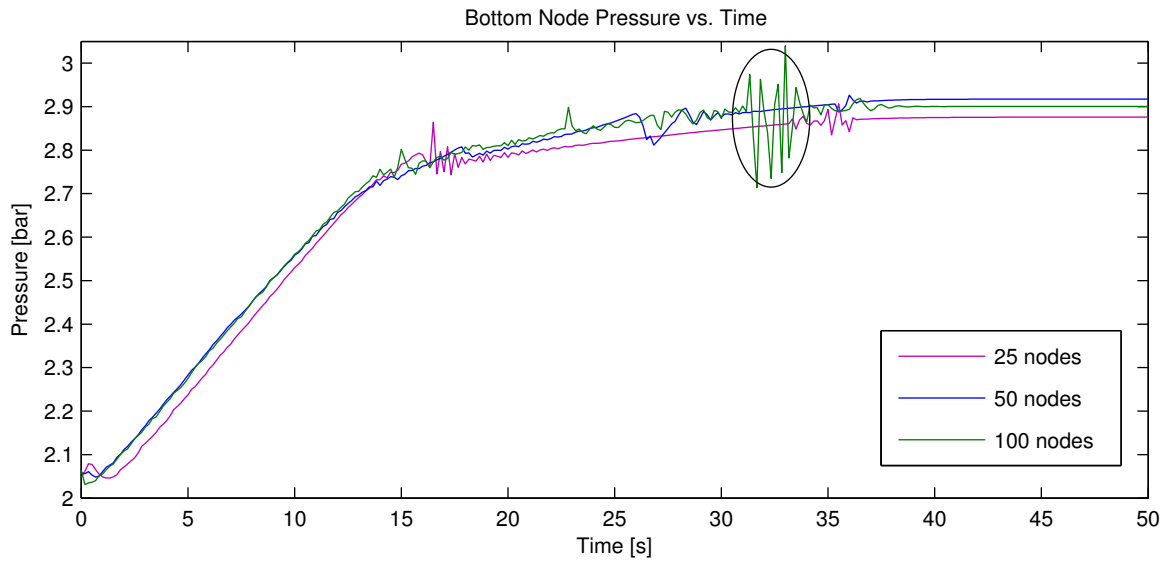


Figure 13.8: Top node pressure versus time for different node settings in transient simulations with SHI slip relation.

13.3 Long Pipe

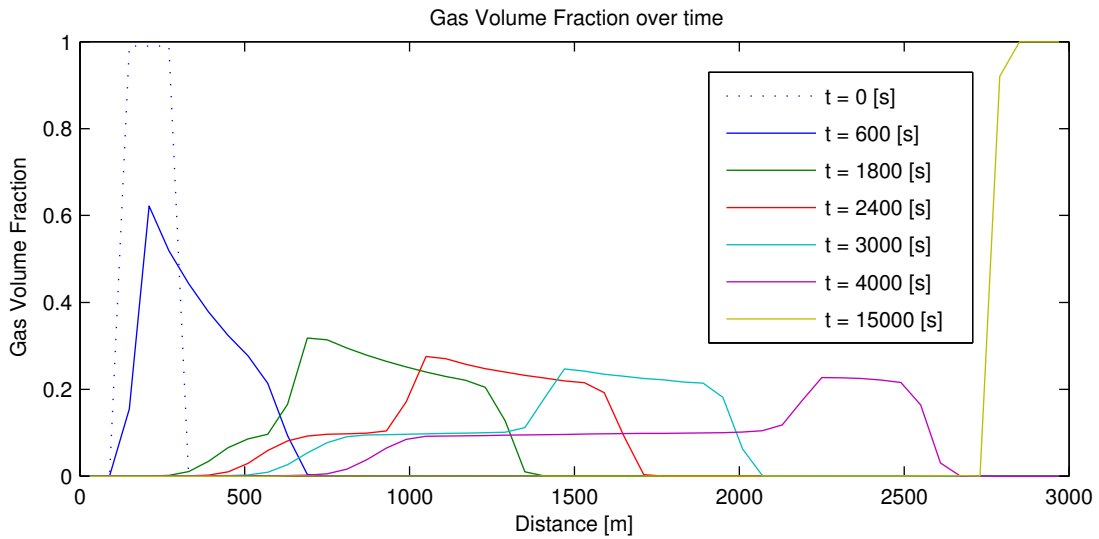


Figure 13.9: Gas volume fraction versus distance in an upscaled case for the migrating gas slug with SHI slip relation.

The transient simulation case using the SHI slip is upscaled to 3000m in length with same pipe diameter, to observe how this upscaling affects the fluid distribution. The gas slug is now placed between 100 and 300 m from bottom. The solutions are stored for the same amount of time steps, $NSTEPS = 300$, and the pipe is divided into 50 nodes. It is seen from Figure 13.9 that the distribution is somewhat similar to that of a short pipe from Figure 13.2, where the front distribution of gas remains higher throughout the simulation. Breakthrough time is seen to occur at $t_{BT} = 4600$ s.

Similar problems as those described in Section 13.2 were also experienced for the upscaled case when gas was starting to accumulate at top. Even more conservative limits for single-phase no-slip flow had to be set.

$$v_g = \begin{cases} \frac{u_3}{u_2}, & \alpha_g > 0.99 \\ \frac{u_1 v_d + u_3 C_o \alpha_l}{u_1 (1 - C_o \alpha_g) + u_2 C_o \alpha_l}, & otherwise \end{cases} \quad v_l = \begin{cases} v_g, & \alpha_g > 0.99 \\ \frac{u_3 (1 - C_o \alpha_g) - u_2 v_d}{u_1 (1 - C_o \alpha_g) + u_2 C_o \alpha_l}, & otherwise \end{cases}.$$

The corresponding pressures of the top- and bottom node can be seen from Figure 13.10 where the perturbations visible in the short pipe are nowhere to be seen. This is most likely a result of the pressures being viewed in a much larger scale, and that both the node- and time stepping is larger. I.e $\Delta x = 60$ m and $\Delta T = 50$ s.

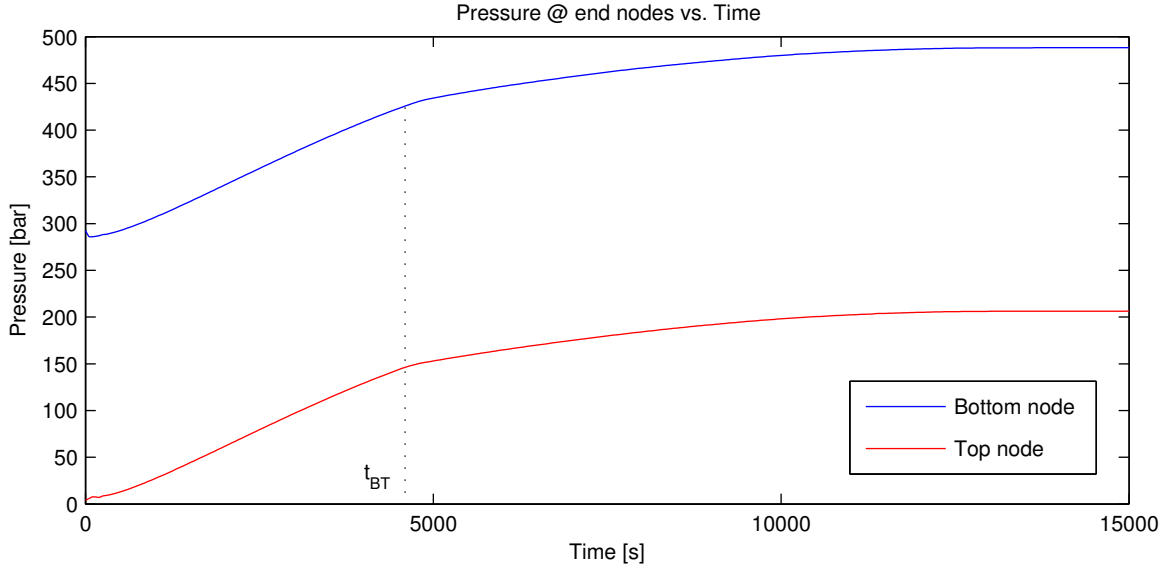


Figure 13.10: Gas volume fraction versus distance in an upscaled case for the migrating gas slug with SHI slip relation.

13.4 Slip Describing Taylor Bubble Flow

Motivation for this was to come up with a slip that affects the gas volume fraction in such a way that it best can be used to represent a Taylor bubble flowing in a short pipe system to atmospheric conditions. The exterior settings are identical to what has been used in transient simulations of a migrating gas slug, in which pipe length $L = 10.9$ m and diameter $D = 15.24$ cm. Initial conditions are the same as being used in gas kick simulations, where a slug ($\alpha_g = 0.99$) is placed near the bottom of the pipe

and then set free. To be able to model the flow of a Taylor bubble in terms of gas distribution, it was desired to have a slip able to let the gas slug maintain much of its initial maximum volume fraction as it is flowing through the pipe. Simulations were carried out for both closed- and open outlets.

When simulating with an open outlet, liquid velocities were found to oscillate between negative and positive velocities in front of the gas slug. Indicating in addition to the counter-current flow taking place as the slug forces liquid behind it, the slug pushes some liquid in front of it for brief moments before surpassing it.

13.4.1 Slug Flow Slip

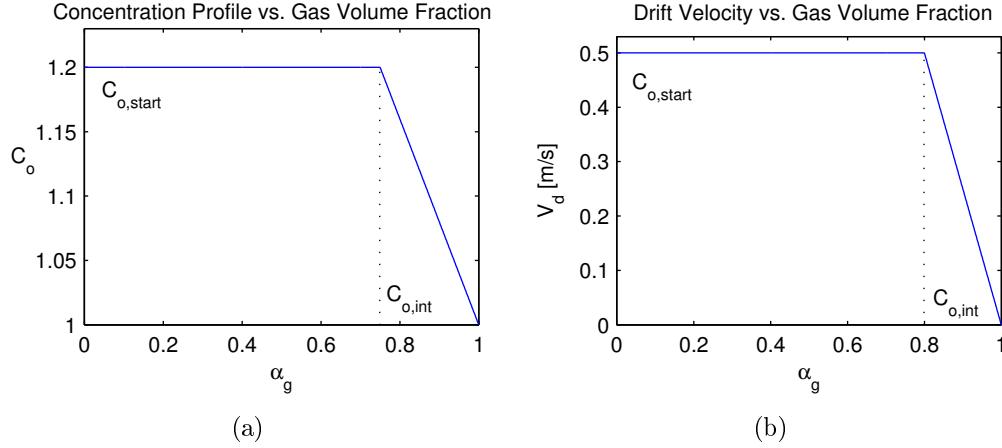


Figure 13.11: Slug flow slip parameters C_o and v_d as functions of the gas volume fraction. See `customslip2.m` in Appendix A.2.

Basis for how this slip would look like were taken in the standard slip parameter determined for bubble/slug flow in small diameter pipes, namely $C_o = 1.2$ and $v_d = 0.5$ m/s. Interpolation limits were then applied to allow for the fluid to have no-slip conditions for when the gas volume fraction goes to unity. This would allow for C_o and v_d to be altered, as well as the corresponding interpolation ranges. See figure 13.11 where these slip parameters are included as functions of the gas volume fraction. The slip parameters used are given in equation

$$\begin{aligned} C_{o,start} &= 1.2 & v_{d,start} &= 0.5 \text{ m/s} \\ C_{o,int} &= 0.75 & v_{d,int} &= 0.8 \end{aligned} \quad (47)$$

From Figure 13.12 it is seen that the basic slug slip parameters given in (47) gives a uniformly distributed gas slug with a gas volume fraction of $\alpha_{g,max} \approx 0.79$. If it is assumed that this resembles the flow of a Taylor bubble, this maximum volume fraction would correspond to a liquid film clinging to the outer edges of the pipe with a thickness⁵ h of 1.69 cm.

Remark (Tuning the slip parameters). It was attempted to vary the tunable parameters within (47). Decreasing $C_{o,start}$ to a value of 1.05 seemed to cause a little bit more spread in distribution ahead and behind the gas slug. Increasing $C_{o,start}$ beyond 1.25 would immediately lead to stability issues

⁵Thickness of an evenly distributed liquid film can be calculated via $h = D(1 - \sqrt{\alpha_g})$

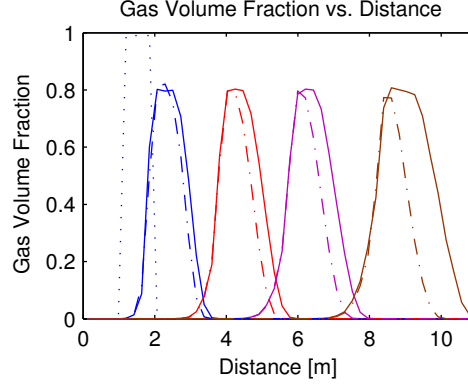


Figure 13.12: Gas volume fraction versus distance for a migrating gas slug when slug flow slip is used. Dashed lines represent simulation with a closed outlet. Times $t = 0, 2, 6, 10, 15$ s have been shown.

with regards to pressure being determined from equation (20), as zero pressure was being determined for the bottom node. Varying the start of interpolation $C_{o,int}$ was found to have little or no effect on the simulation case being studied.

It is suspected that the reason for the model breaking down when $C_{o,start} > 1.25$ is indirectly related to the initial conditions of the fluid. The initial gas fraction is 0.99 with corresponding zero liquid velocity throughout the pipe. As the gas velocity for the next time step can be calculated via the simple expression (when $v_l = 0$) $v_g = \frac{v_d}{1 - \alpha_g C_o}$, it employs a condition for $\alpha_g C_o < 1$ in order to prevent negative gas velocities from being calculated. This leads to the maximum profile parameter within the gas slug to be $C_o < \frac{1}{\alpha_g} = 1.01$. Extrapolating from $C_o(0.99) = 1.01$ and back to $C_{o,int}$ it is found that $C_{o,start} < 1.2525$ must be the condition when having $C_{o,int} = 0.75$.

When increasing the drift velocity $v_{d,start}$, the gas slug was found to move much more rapidly through the pipe yet this seemed to have little impact on the spread in distribution of the slug. Similarly, decreasing the drift velocity $v_{d,start}$ made the slug move much slower yet no impact on the distribution. Altering the interpolation parameter $v_{d,int}$ was found to have a major impact on distribution. When lowering this value to 0 massive spread in distribution ahead of the slug was observed. Increasing $v_{d,int}$ to 0.97 led to the increasing amounts of spread in distribution over time, where mores spread was observed ahead of the slug than behind it.

13.4.2 Taylor Bubble Slip

From Hibiki and Ishii [6], slip parameters used in describing slug flow is given by

$$C_o = 1.2 - 0.2 \sqrt{\frac{\rho_g}{\rho_l}}, \quad v_d = 0.37 \sqrt{\left(gD \frac{\rho_l - \rho_g}{\rho_l} \right)}$$

where the expression for drift velocity is in fact the terminal rise velocity for a Taylor bubble. The constant 0.37 in the drift velocity relation is in fact a parameter depending on the dimensionless Eötvös- and inverse viscosity number, but can be shown for many situations to attain a value of 0.37. Figure 13.13 shows the slug is seen to keep a gas volume fraction of $\alpha_g \sim 0.82$ throughout. This is

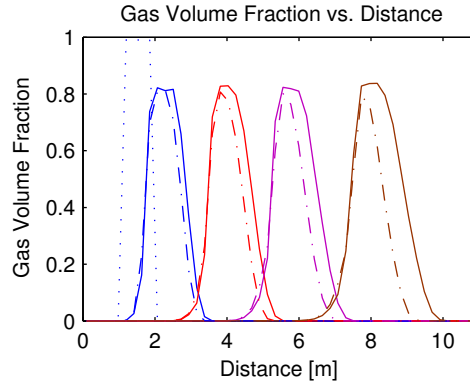


Figure 13.13: Gas volume fraction versus distance for a migrating gas slug when Taylor bubble slip is used. Dashed lines represent simulation with a closed outlet. Times $t = 0, 2, 6, 10, 15$ s have been shown.

slightly higher than what was observed using the more basic slug flow slip in Section 13.4.1 and would with respect to the flow of a Taylor bubble correspond to a liquid film clinging the outer edges of the pipe with a thickness h of about 1.44 cm, about 0.25 cm thinner liquid film than when using the slug flow slip.

Remark. As the slip parameters now indirectly relies on pressure through the respective densities, it was tried reducing the frictional term of equation (11) by a factor of ten to see what impact this would have on the slug behavior. This proved to have no significant effect on the volume fractions as they appeared to remain unaffected.

14 Conclusions and Further Work

The slip model described in [15], referred to in this paper as SHI slip, has been implemented in the MATLAB model via the sub-routine given in Appendix A.1. These slip parameters are found to be rather complex as they rely on the volume fractions, mixture velocity, densities and flow angle (in the case of non-vertical flow). In addition to this, several tuning parameters are implemented, allowing for better fit with experimental observations. Experiments were in [15] carried out in a 10.9 m long 15.24 cm diameter pipe where inlet flow rates were varied, and steady-state holdup was measured.

Ten numerical simulations for steady-state conditions with the optimized slip parameters have been carried out for vertical flow, proving to be consistent with experimental data as a root-mean-square error of only 0.039 was observed. This same set of optimized slip parameters was then directly applied in transient simulation study of a migrating gas slug in a vertical pipe.

It is indicated that slip parameters capable of describing steady state flows, might not be directly applicable in transient settings. When simulating a transient case of a migrating gas slug within the same physical settings as for steady-state simulations, now flowing towards a closed outlet, it was found that the gas concentration at the front diminished over time and an increasing trail of gas was left behind it, flowing at a lower velocity. This seems not to be representative of how a typical Taylor bubble would ascend the pipe.

Using two sets of optimized tuning parameters for the SHI slip model in transient simulations, distinct differences in phase distributions over time was observed. In order to accurately predict pressures in a transient environment, it is necessary to a certain extent to be able to correctly model the evolution in phase distribution. As the two sets of parameters does not coincide with regards to phase distribution, further knowledge of transient behavior is needed. It would therefore be desirable to have experimental data in realistic transient flowing conditions in which transient slip relations can be specifically designed and optimized to fit the observations. Bearing in mind the strong coupling between liquid velocity and the concentration profile parameter C_o , and gas velocity and the drift-velocity v_d , this would seem to be a good starting point for designing such slip relations.

Observations made when the migrating gas slug was accumulating at the top of the pipe, seems to indicate that the SHI slip model is causing the drift-flux model failing to remain hyperbolic for some periods in time. Unphysical oscillations were observed in both the fluid fractions and in the pressures. This effect was seen to increase in magnitude as the number of nodes was increased.

As the SHI slip model seemed unable to describe the migrating gas slug very well, it was attempted to come up with a slip relation better able to describe the typical flow of a Taylor bubble, thus maintaining much of its initial gas volume fraction over time. With basis in well-known slip parameters for slug flow, $C_o = 1.2$ and $v_d = 0.5$ m/s, it was tried varying these as well as the interpolation ranges $C_{o,int}$ and $v_{d,int}$ for when $C_o \rightarrow 1$ and $v_d \rightarrow 0$ m/s for single-phase gas flow. Slip parameters $C_o = 1.2$, $v_d = 0.5$ m/s, $C_{o,int} = 0.75$ and $v_{d,int} = 0.8$ proved to give an average maximum slug volume fraction of $\alpha_{g,max} \approx 0.79$.

Implementing the slip relation from [6] specifically designed to describe the rise velocity of a Taylor bubble, proved to give a slightly higher maximum volume fraction in the gas over time, $\alpha_{g,max} \approx 0.82$. The overall rise velocity of the gas was now seen to be somewhat higher than when using the simple slug flow slip.

Due to time limitations, it was not attempted to expand the drift-flux model beyond that of the two-phase gas-liquid flow setting. In [15], it is described modifications needed to allow for oil-water flows, as well as a tentative modification to allow for three-phase oil-water-gas flows.

Nomenclature

A	Cross-sectional area of pipe
CFL	Criterion for stability in the explicit scheme
χ	Parameter used in the AUSMV splitting scheme
C_o	Concentration profile parameter used in slip relation.
Δt	Time step length
Δx	Node length
ρ	Density
D	Diameter
\hat{D}	Dimensionless diameter
K	Critical Kutateladze number
Re	Dimensionless Reynolds number
λ	Eigenvalue
F	Column vector of flux terms
f	Flux term
g	Gravitational constant
G	Column vector of source-sink terms
σ_{gl}	Interfacial tension between gas and liquid
J	Jacobian matrix
L	Pipe length
\hat{n}	Unit normal vector
ω	Approximate sound velocity
P	Pressure splitting function used in numerical schemes.
$\partial_{\mathcal{O}}$	Partial derivative with regards to property \mathcal{O}
p	Pressure
RHS	Right-hand-side of an equation
a	Single-phase sound velocity
Γ	Source/sink term in mass-balance equations

σ	Stress tensor
0	Constant reference parameter
g	Gas
i	Node coordinate
L	Node to the left of an interface
l	Liquid
R	Node to the right of an interface
s	Superficial
n	Time step
$S(t)$	Control surface
t	Surface tension
t_{BT}	Time of breakthrough
U	Column vector of conservative variables
u	Conservative variable
V	Velocity splitting function used in numerical schemes
v_d	Drift velocity of gas
v	Phase velocity
μ	Viscosity
$V(t)$	Control Volume
α	Phase volume fraction
Q	Volume rate
WC	Water cut

List of Figures

4.1	Pipe cross-section indicating velocity profile for the mixture and concentration profile for the gas. Drawn using Adobe Illustrator CS5.	4
5.1	Flow patterns occurring in vertical two-phase flow. Drawn using Adobe Illustrator CS5.	5
7.1	Pressure versus the conserved variables u_1 and u_2 . Figure b) gives a closer view of the linear trend in a) when $u_1 > 999.9 \text{ kg/m}^3$ for $u_2 = 0 \text{ kg/m}^3$. Drawn using p_u1_u2.m in Appendix A.10.	13
7.2	Sound velocity for a stagnant fluid under atmospheric conditions as a function of gas volume fraction in a). Zoomed in on limiting sound velocities in b) and c). Drawn using sound_velocity.m in Appendix A.5.	15
7.3	Comparison of “approximate” sound velocity from eq. (24) with “real” sound velocity from eq. (23) as functions of gas volume fraction. Drawn using sound_velocity.m in Appendix A.5.	16
8.1	Illustration of the computational grid used in Matlab when computing a numerical solution of the drift-flux model. Drawn using Adobe Illustrator CS5.	17
8.2	Mach splitting function versus mach number used in FVS. Drawn using vsplit_plot.m in Appendix A.3.	20
8.3	Mach split used in AUSMV versus Mach number. Drawn using vsplit_plot.m in Appendix A.3.	21
9.1	Flowcharts describing the work flow in which the MATLAB model operates.	25
10.1	Plot of slip parameters C_o and V_d as functions of gas volume fraction for parameters given in Table 10.2. Drawn using c1_c2.m in Appendix A.6.	27
10.2	Gas velocity vs. volume fraction of gas for zero liquid velocity using SHI slip. Drawn using c1_c2.m in Appendix A.6.	29
10.3	Sensitivity runs on profile parameter and drift velocity as functions of gas volume fraction, with basis in base case from Table 10.2. In a) it is noted that $C_o(A = 1) = 1$ for all α_g . Drawn using SHI_c1_c2_ex.m in Appendix A.8.	30
10.4	3D plot of gas volume fraction vs. time and distance for flooding and steady state conditions using SHI slip with $Q_g = 61 \text{ [m}^3/\text{hr}]$ and $WC = 0.04$	31
10.5	Simulated steady state holdup data versus experimental data from from H.Shi et.Al, [15]. Slip parameters used are $A = 1.4$, $B = 0.0$, $a_1 = 0.1$ and $a_2 = 0.18$. The figure is plotted using holdup_results.m in Appendix A.7.	34
10.6	Simulated steady state holdup data versus experimental data from from H.Shi et.Al, [15]. Slip parameters used are $A = 1.4$, $B = 0.0$, $a_1 = 0.1$ and $a_2 = 0.18$. The figure is plotted using MATLAB routine holdup_results.m.	35
10.7	Gas volume fraction versus distance for steady state simulations with inlet gas volume rate $Q_g = 61 \text{ m}^3/\text{hr}$ and water cut $WC = 0.04$ using SHI slip relation.	36
10.8	Simulation run for steady state simulations with inlet gas volume rate $Q_g = 61 \text{ m}^3/\text{hr}$ and water cut $WC = 0.04$ using SHI slip relation for times $t = 0, 6, 8, 10, 30\text{s}$	38
10.9	Case study of pressure vs. time for three cases. Case of standard friction term and varying mass rates (1fric), case of 3 times the standard friction term and varying mass rates (3fric), and case of standard friction term and constant mass rates (1fric, constmassflux).	39

10.10	Case study of mass flow rates vs. time in steady-state simulations for three cases. Case of standard friction term and varying mass rates (1fric), case of 3 times the standard friction term and varying mass rates (3fric), and case of standard friction term and constant mass rates (1fric, constmassflux).	40
12.1	3D plot of gas volume fraction versus time and distance for a migrating gas slug using the simple slip relation.	41
12.2	Gas volume fraction versus distance in a transient simulation of a migrating gas slug using the simple slip relation.	42
12.3	Simulation parameters for a migrating gas slug using the simple slip relation. It is the times $t = 0, 6, 8, 10, 30$ s that have been shown.	43
12.4	Pressure at the end nodes versus time in a transient simulation of a migrating gas slug, where the simple slip relation has been used.	44
13.1	Three-dimensional plot of gas volume fraction versus time and distance for a migrating gas slug towards a closed outlet, where the SHI slip relation has been used.	45
13.2	Gas volume fraction versus distance for a migrating gas slug using SHI slip relation.	46
13.3	Simulation parameters for a migrating gas slug using SHI slip relation. The times $t = 0, 2, 4, 6, 8, 10, 50$ s are shown.	47
13.4	Pressure at top- and bottom node versus distance for transient gas migration simulation using SHI slip relation.	48
13.5	Gas volume fraction versus distance in a transient simulation with the SHI slip relation. Illustration of an unphysical behavior using SHI slip as increasing amounts of gas is accumulating at the top, where times $t = 14, 15, 16, 17, 22, 25$ s have been selected for this purpose.	48
13.6	Comparison of gas volume fraction versus distance at different times for different set of SHI slip tuning parameters. Solid lines have $A = 1.4, B = 0.0, m = 1.0, a_1 = 0.1$ and $a_2 = 0.18$ while dashed lines have $A = 1.2, B = 0.6, m = 1.28, a_1 = 0.05$ and $a_2 = 0.13$,	49
13.7	Top node pressure versus time for different node settings in transient simulations with SHI slip relation.	50
13.8	Top node pressure versus time for different node settings in transient simulations with SHI slip relation.	51
13.9	Gas volume fraction versus distance in an upscaled case for the migrating gas slug with SHI slip relation.	51
13.10	Gas volume fraction versus distance in an upscaled case for the migrating gas slug with SHI slip relation.	52
13.11	Slug flow slip parameters C_o and v_d as functions of the gas volume fraction. See customslip2.m in Appendix A.2.	53
13.12	Gas volume fraction versus distance for a migrating gas slug when slug flow slip is used. Dashed lines represent simulation with a closed outlet. Times $t = 0, 2, 6, 10, 15$ s have been shown.	54
13.13	Gas volume fraction versus distance for a migrating gas slug when Taylor bubble slip is used. Dashed lines represent simulation with a closed outlet. Times $t = 0, 2, 6, 10, 15$ s have been shown.	55

References

- [1] BUTTERWORTH, D., AND HEWITT, G. F., Eds. *Two-Phase Flow and Heat Transfer*. Harwell Series. Oxford University Press, 1977.
- [2] EVJE, S., AND FJELDE, K. K. Hybrid flux-splitting schemes for a two-phase flow model. *Journal of Computational Physics* 175, 2 (2002), 674 – 701.
- [3] FINNEMORE, E. J., AND FRANZINI, J. B. *Fluid Mechanics with Engineering Applications*, 10 ed. McGraw-Hill, 2002.
- [4] HARMATHY, T. Z. Velocity of large drops and bubbles in media of infinite or restricted extent. *AIChE Journal* 6, 2 (1960), 281–288.
- [5] HASAN, A. R., AND KABIR, C. S. Predicting multiphase flow behavior in a deviated well. *SPE Production Engineering Volume 3, Number 4* (1988), 474–482.
- [6] HIBIKI, T., AND ISHII, M. One-dimensional drift-flux model for two-phase flow in a large diameter pipe. *International Journal of Heat and Mass Transfer* 46, 10 (2003), 1773 – 1790.
- [7] HOLMES, J. A., BARKVE, T., AND LUND, Å. Application of a multisegment well model to simulate flow in advanced wells. *SPE 50646* (1998).
- [8] LEVEQUE, R. J. *Finite volume methods for hyperbolic problems*. Cambridge University Press, Cambridge, 2002.
- [9] LIOU, M.-S., AND STEFFEN, JR., C. J. A new flux splitting scheme. *Journal of Computational Physics* 107 (July 1993), 23–39.
- [10] ODDIE, G., SHI, H., DURLOFSKY, L. J., AZIZ, K., PFEFFER, B., AND HOLMES, J. A. Experimental study of two and three phase flows in large diameter inclined pipes. *International Journal of Multiphase Flow* 29, 4 (2003), 527 – 558.
- [11] PAPANZACOS, P. Mathematical modeling. *University of Stavanger* (1991).
- [12] ROMATE, J. E. An approximate riemann solver for a two-phase flow model with numerically given slip relation. *Computers & Fluids* 27, 4 (1998), 455 – 477.
- [13] SCHLUMBERGER. *Eclipse Reference Manual*, 2010.1 ed.
- [14] SCHLUMBERGER. *Eclipse Technical Description*, 2010.2 ed.
- [15] SHI, H., HOLMES, J. A., DURLOFSKY, L. J., AZIZ, K., DIAZ, L. R., ALKAYA, B., AND ODDIE, G. Drift-flux modeling of multiphase flow in wellbores. *SPE 84228* (2003).
- [16] SHI, H., HOLMES, J. A., DURLOFSKY, L. J., AZIZ, K., DIAZ, L. R., ALKAYA, B., AND ODDIE, G. Drift-flux modeling of two-phase flow in wellbores.
- [17] Chapter 3. balance equations. In *Fluid Mechanics for Petroleum Engineers*, E. Bobok, Ed., vol. 32 of *Developments in Petroleum Science*. Elsevier, 1993, pp. 35 – 58.
- [18] TAITEL, Y., BARNEA, D., AND DUKLER, A. Modelling flow pattern transitions for steady upward gas-liquid flow in vertical tubes. *AIChE Journal* 26, 3 (1980), 345–354.

- [19] WADA, Y., AND LIOU, M.-S. An accurate and robust flux splitting scheme for shock and contact discontinuities. *SIAM J. Sci. Comput.* 18 (May 1997), 633–657.
- [20] WALLIS, G. B. One-dimensional two-phase flow. *McGraw-Hill* (1969).
- [21] WALLIS, G. B., AND MAKKENCHERY, S. The hanging film phenomenon in vertical annular two-phase flow. *Journal of Fluids Engineering* 96, 3 (1974), 297–298.
- [22] ZUBER, N., AND FINDLAY, J. Average volumetric concentration in two-phase flow systems. *Trans ASME J. Heat Transfer* (1965), 453–468.

A MATLAB Model Files

A.1 SHIslip2.m

```

function [c1,c2,vg] = SHIslip2(alpG,Vm_pre,diam,rhoL,rhoG)
%Slip parameters defined in SPE 84228
%Outputs c1 and c2 to be used in classical slip definition
% vG=c1*Vm+c2

%%%%%%%%%%%%%%%%%%%%%%%%%%%%%%%%%%%%%%%%%%%%%%%%%%%%%%%%%%%%%%%%%%%%%%%%
% Tuning Parameters %
%%%%%%%%%%%%%%%%%%%%%%%%%%%%%%%%%%%%%%%%%%%%%%%%%%%%%%%%%%%%%%%%%%%%%%%%

Fv=1; %Tuning parameter default 1.0
A=1.4; %Profile parameter default 1.2
B=0.0; %Tuning parameter default 0.3
aa1=0.1; %Tuning parameter for transition from bubble flow regime default 0.2
aa2=0.18; %Tuning parameter for transition from bubble flow regime default 0.4

grav=9.81; %Gravitational constant
sigmagl=0.072; %Interfacial tension gas and liquid [N/m]

%%%%%%%%%%%%%%%%%%%%%%%%%%%%%%%%%%%%%%%%%%%%%%%%%%%%%%%%%%%%%%%%%%%%%%%%
% Start Program %
%%%%%%%%%%%%%%%%%%%%%%%%%%%%%%%%%%%%%%%%%%%%%%%%%%%%%%%%%%%%%%%%%%%%%%%%

n = length(alpG);

Vc = zeros(1,n);
Ddim = zeros(1,n);
Kud = zeros(1,n);
vGsf = zeros(1,n);
bcond1 = zeros(1,n);
bcond2 = zeros(1,n);
gam = zeros(1,n);
beta = zeros(1,n);
c1 = zeros(1,n);
c2 = zeros(1,n);
Kal = zeros(2,n);
Kalphag = zeros(1,n);
vg = zeros(1,n);

if B>=(2-A)/A,
    B=nan;
    fprintf('Stability criterion for B is not met')
end

```

```

Vc=(sigmagl*grav*(rhoL-rhoG)./(rhoL.^2)).^(1/4); %Characteristic velocity

Ddim_val=[2 4 10 14 20 28 50]; %table for determining critical kudladze number
Kude=[0 1 2.1 2.5 2.8 3.0 3.2]; %table for determining critical kudladze number

Ddim=sqrt((grav*(rhoL-rhoG)./sigmagl))*diam; %Dimensionless diameter

for i=1:length(alpG)

if Ddim(i)<2
    Kud(i)=0;
elseif 2<=Ddim(i) & Ddim(i)<=50
    Kud(i)=interp1(Ddim_val,Kude,Ddim(i)); %interpolation
else
    Kud(i)=3.2;
end

end

vGsf=Kud.*sqrt(rhoL./rhoG).*Vc; %Gas flooding velocity

bcond1 = Fv*alpG.*abs(Vm_pre)./vGsf;
bcond2 = alpG;
beta=max(bcond1,bcond2);

gam=(beta-B)./(1-B);

for i=1:length(gam)

if gam(i)<0
    gam(i) = 0;
elseif gam(i)>1
    gam(i) = 1;
end

end

c1=A./(1+(A-1)*gam.^2); %Profile parameter used to describe slip

aa=[aa1 aa2];

for i=1:length(alpG)

if alpG(i)<=aa1
    Kalphag(i)=1.53./c1(i);

```

```

elseif aa1<alpG(i) & alpG(i)<aa2
    Kal1=[1.53./c1(i) Kud(i)];
    Kalphag(i)=interp1(aa,Kal1,alpG(i));

elseif alpG(i)>=aa2
    Kalphag(i)=Kud(i);

end

end

c2 = (1-alpG.*c1).*c1.*Kalphag.*Vc./(alpG.*c1.*sqrt(rhoG./rhoL)+1-alpG.*c1);
c2_diff = c1.*Kalphag.*Vc./(alpG.*c1.*sqrt(rhoG./rhoL)+1-alpG.*c1);

vg = c2./(1-alpG.*c1);
vg(1,n) = c2_diff(1,n);

```

A.2 *customslip2.m*

```

function [c1,c2] = customslip2(alpG,rhoG,rhoL)

%alpG = linspace(0,1,1000);

n = length(alpG);
c1 = zeros(1,n);
c2 = zeros(1,n);
sigmagl = 0.072;

%%%%%%%%%%%%%%%%%%%%%%%%%%%%%%%%%%%%%%%%%%%%%%%%%%%%%%%%%%%%%%%%%%%%%%%%
% Tuning Parameters %
%%%%%%%%%%%%%%%%%%%%%%%%%%%%%%%%%%%%%%%%%%%%%%%%%%%%%%%%%%%%%%%%%%%%%%%%

c1_start = 1.2; % c1 base value
c1_int = 0.75; % alpG value interpolation in c1
c2_start = 0.5; % c2 base value
c2_int = 0.8; % alpG value interpolation in c2

%%%%%%%%%%%%%%%%%%%%%%%%%%%%%%%%%%%%%%%%%%%%%%%%%%%%%%%%%%%%%%%%%%%%%%%%

%c1(:) = c1_start;
%c2(:) = c2_start;

drho = rhoL-rhoG;
g = 9.81;
d = 0.152;
%c1(:) = c1_start - 0.2*sqrt(rhoG./rhoL); % Churn

```

```

%c2(:) = 2*sqrt(2)*(g*sigmagl*drho./rhoL.^2).^^(1/4); % Churn
c1(:) = 1.2-0.2*(rhoG/rhoL)^0.5;
c2(:) = 0.37*(g*d*drho./rhoL).^0.5;

a1 = (1-c1_start)/(1-c1_int);
a2 = (0-c2_start)/(1-c2_int);

for i = 1:n
    if ((alpG(i) >= c1_int) && (alpG(i) <= 1.0))
        c1(i) = c1_start + a1*(alpG(i)-c1_int); % Linear
        %c1(i) = c1_start - (c1_start-1)*(alpG(i)-c1_int)^(0.4*(1-alpG(i))); % Non-linear
    end

    if ((alpG(i) >= c2_int) && (alpG(i) <= 1.0))
        c2(i) = c2_start + a2*(alpG(i)-c2_int); % Linear
        %c2(i) = c2_start - c2_start*(alpG(i)-c2_int)^(30*(0.5-0.5*alpG(i))); % Non-linear
    end
end
%subplot(2,1,1)
%plot(alpG,c1)

%subplot(2,1,2)
%plot(alpG,c2)

```

A.3 vsplit_plot.m

```

function vsplit_plot

clear
clf
clc

set(gcf,'defaultaxesfontsize',8)
set(gcf,'defaulttextfontsize',8)

chi = [0 0.5 1.0]; %input 3 chi variables
omega = 20; % Sound velocity. Not important when relative velocities are plotted

for i = 1:length(chi)
    leg{i} = sprintf('\chi = %0.2g',chi(i));
end
ind = 1:length(chi);

[~,Vausm_div1,~] = vsplit_chi(chi(1),omega);
[~,Vausm_div2,~] = vsplit_chi(chi(2),omega);
[v_div,Vausm_div3,~] = vsplit_chi(chi(3),omega);

```



```

plot(v_div,Vausm_div1(1,:), 'b',v_div,Vausm_div2(1,:), 'r',v_div,Vausm_div3(1,:), 'm')
hold on
plot(v_div,Vausm_div1(2,:), 'b', 'HandleVisibility', 'off')
plot(v_div,Vausm_div2(2,:), 'r',v_div,Vausm_div3(2,:), 'm')
ad_origo
xlabel('v/c')
ylabel('$\tilde{V}^{\pm}$ / c', 'rot', 0, 'Interpreter', 'Latex')
legend('Location', 'best')
text(0.1,0.5, '$\tilde{V}^{+}$ / c', 'Interpreter', 'Latex')
text(0.1,-0.5, '$\tilde{V}^{-}$ / c', 'Interpreter', 'Latex')
title('Velocity Splitting in AUSMV')

```

A.4 vsplit_chi.m

```

function [v_div,Vausm_div,Vfvs_div] = vsplit_chi(chi,omega)
% Plotting of velocity splitting functions used
% in FVS and AUSM.

c=omega; %approximate sound velocity

%%%%%%%%%%%%%%%%%%%%%%%%%%%%%%%%%%%%%%%%%%%%%%%%%%%%%%%%%%%%%%%%%%%%%%%%
% Subsonic %
%%%%%%%%%%%%%%%%%%%%%%%%%%%%%%%%%%%%%%%%%%%%%%%%%%%%%%%%%%%%%%%%%%%%%%%%

v_div = -1:0.001:1;
v = v_div*abs(c);

Vp=c/4*(v_div+1).^2; %V+ FVS
Vm=-c/4*(v_div-1).^2; %V- FVS
Vpausm=chi*Vp+(1-chi)*(v+abs(v))/2; %V+ ausm
Vmausm=chi*Vm+(1-chi)*(v-abs(v))/2; %V- ausm

v_div = [v_div,NaN];
Vp=[Vp,NaN];
Vm=[Vm,NaN];
Vpausm=[Vpausm,NaN];
Vmausm=[Vmausm,NaN];

%%%%%%%%%%%%%%%%%%%%%%%%%%%%%%%%%%%%%%%%%%%%%%%%%%%%%%%%%%%%%%%%%%%%%%%%
% Supersonic + %
%%%%%%%%%%%%%%%%%%%%%%%%%%%%%%%%%%%%%%%%%%%%%%%%%%%%%%%%%%%%%%%%%%%%%%%%

v1_div = 1:0.001:1.2;
v_div = [v_div,v1_div];
v1 = v1_div*c;

```

```

Vp=[Vp,(1/2)*(v1+abs(v1))];
Vm=[Vm,(1/2)*(v1-abs(v1))];
Vpausm=[Vpausm,(1/2)*(v1+abs(v1))];
Vmausm=[Vmausm,(1/2)*(v1-abs(v1))];

v_div = [NaN,v_div];
Vp = [NaN,Vp];
Vm = [NaN,Vm];
Vpausm = [NaN,Vpausm];
Vmausm = [NaN,Vmausm];

%%%%%%%%%%
% Supersonic - %
%%%%%%%%%%

v2_div = -1.2:0.001:-1.0;
v_div = [v2_div,v_div];
v2 = v2_div*c;

Vp=[(1/2)*(v2+abs(v2)),Vp];
Vm=[(1/2)*(v2-abs(v2)),Vm];
Vpausm=[(1/2)*(v2+abs(v2)),Vpausm];
Vmausm=[(1/2)*(v2-abs(v2)),Vmausm];

V(1,:) = Vp;
V(2,:) = Vm;
Vausm(1,:) = Vpausm;
Vausm(2,:) = Vmausm;

Vfvs_div = V/c; % Relative FVS velocity splitting
Vausm_div = Vausm/c; % Relative AUSMV velocity splitting

```

A.5 sound_velocity.m

```

function sound_velocity
clear
clc

%Sound velocity for a no-slip case in which
%fluid mixture of gas and liquid are at a
%stand-still. I.e v=0.

syms u1 u2 rho1o plo al ag

B=al^2*(rho1o-plo/(al^2)-u1-u2*(ag/al)^2);

```

```
C=-u2*ag^2*al^2*(rho1o-p1o/(al^2));

p=simplify((-B+sqrt(B^2-4*C))/2);

p_1=diff(p,u1);
p_2=diff(p,u2);

p=1*10^5; %Pascal

ag=316; %m/s
al=1000; %m/s
rho1o=1000; %kg/m3
p1o=1*10^5; %Pascal

rho2=p/ag^2;
rho1=rho1o+(p-p1o)/al^2;

alphag=linspace(0.00,1.00,1000);
lambda=zeros(1,1000);
approx=zeros(1,1000);

u1=(1-alphag)*rho1;
u2=alphag*rho2;

P_1=subs(p_1);
P_2=subs(p_2);

i=1;

for i=1:1000,
lambda(i)=sqrt(1/(u1(i)+u2(i))*(u2(i).*P_2(i)+u1(i).*P_1(i)));
approx(i)=sqrt(p/(alphag(i)*rho1*(1-alphag(i))));
end

omega(1,:)=lambda;
omega(2,:)=approx;

plot(alphag,lambda)
axis([0 1 0 200])
xlabel('Gas Volume Fraction')
ylabel('Sound Velocity [m/s]')

figure;
plot(alphag,lambda)
hold on
```

```

plot(0,lambda(1),'s','MarkerFaceColor','b')
text(0.05,1000,'sound velocity liquid')
axis([0 0.001 950 1020])
xlabel('Gas Volume Fraction')
ylabel('Sound Velocity [m/s]')

figure;
plot(alphag,lambda)
hold on
plot(1,lambda(length(lambda)),'s','MarkerFaceColor','b')
text(0.9995,316,'sound velocity gas')
axis([0.9985 1.0 300 322])
xlabel('Gas Volume Fraction')
ylabel('Sound Velocity [m/s]')

figure;
plot(alphag,omega)
axis([0 1 0 100])
title('Sound Velocity vs. Gas Volume Fraction')
legend('Real Sound Velocity', 'Approximate Sound Velocity')
xlabel('Gas Volume Fraction')
ylabel('Sound Velocity [m/s]')
end

```

A.6 c1_c2.m

```

function c1_c2

clear
clc

alpG = 0:0.001:1;
Vm_pre = 3;
diam = 0.152;
rhoL = 1000;
rhoG = 20;

c11 = zeros(1,length(alpG));
c22 = zeros(1,length(alpG));
vgg = zeros(1,length(alpG));

for i=1:length(alpG)
    [c1,c2,vg] = SPEslip2_ex(alpG(i),Vm_pre,diam,rhoL,rhoG);
    c11(i) = c1;

```

```
        c22(i) = c2;
        vgg(i) = vg;
end

X = [0 1];
Y = [vgg(1) vgg(length(vgg))];

h = [1 2 3];

clf

plot(alpG,c11)
title('Concentration Profile Parameter')
xlabel('\alpha_g')
ylabel('C_o')
axis([0 1 1 1.25])

figure;
plot(alpG,c22)
title('Drift Velocity')
xlabel('\alpha_g')
ylabel('V_d [m/s]')
axis([0 1 0 0.6])

figure;
plot(alpG,vgg)
hold on
title('v_g(v_l = 0)')
plot(X,Y,'s','MarkerFaceColor','b')
text(0.01,0.1,'bubble rise velocity')
text(0.75,3.6,'flooding velocity')
xlabel('\alpha_g')
ylabel('Gas Velocity [m/s]')
axis([0 1 0 4])
```

A.7 holdup_results.m

```
%function holdup_results
%Compares simulated with experimental data

clear
clc
```

```

alpW_exp = [0.82 0.83 0.88 0.9 0.68 0.71 0.78 0.49 0.51 0.60]; % Experimental data
alpW_simQ = [0.78 0.81 0.86 0.91 0.60 0.65 0.75 0.45 0.50 0.60]; % Simulated data, const. Q.
alpW_simM = [0.75 0.79 0.85 0.9 0.55 0.60 0.72 0.37 0.42 0.57]; % Simulated data, const. masflux.

alpG_exp = zeros(1,length(alpW_exp));
alpG_simQ = zeros(1,length(alpW_simQ));
alpG_simM = zeros(1,length(alpW_simM));

for i=1:length(alpW_exp)
alpG_exp(i) = 1 - alpW_exp(i);
alpG_simQ(i) = 1 - alpW_simQ(i);
alpG_simM(i) = 1 - alpW_simM(i);
end

alp = linspace(0,1,101);
unity = alp;
unity10_min = 0.9*alp;
unity10_max = 1.1*alp;
unity20_min = 0.8*alp;
unity20_max = 1.2*alp;

RMSE_Q = rmse(alpW_exp,alpW_simQ);
RMSE_M = rmse(alpW_exp,alpW_simM);
rmsQ = sprintf('root mean square error = %0.2g',RMSE_Q);
rmsM = sprintf('root mean square error = %0.2g',RMSE_M);

figure;
plot(alp,unity,alp,unity10_min,'--g',alp,unity20_min,':r',alp,unity10_max,'--g',...
      alp,unity20_max,':r',alpG_exp,alpG_simQ,'+b')
text(0.05,0.9,rmsQ)
axis([0 1 0 1])
legend('1:1','\pm 10%','\pm 20%','Location','Best')
title('Steady State Holdup - Constant Volume Rate')
xlabel('Experimental Gas Holdup, \alpha_{g,e_x_p}')
ylabel('Simulated Gas Holdup, \alpha_{g,s_i_m}')

figure;
plot(alp,unity,alp,unity10_min,'--g',alp,unity20_min,':r',alp,unity10_max,'--g',...
      alp,unity20_max,':r',alpG_exp,alpG_simM,'+b')
text(0.05,0.9,rmsM)
axis([0 1 0 1])
legend('1:1','\pm 10%','\pm 20%','Location','Best')
title('Steady State Holdup - Constant Mass Flux')
xlabel('Experimental Gas Holdup, \alpha_{g,e_x_p}')
ylabel('Simulated Gas Holdup, \alpha_{g,s_i_m}')

```

A.8 SHI_c1_c2_ex.m

```

function SHI_c1_c2_ex

clear
clc

set(gcf,'defaultaxesfontsize',8)
set(gcf,'defaulttextfontsize',8)

alpG = (0:0.01:1);
n = length(alpG);

Vm_pre = 1.0*ones(1,n);
diam = 0.1524;
rhoL = 1000*ones(1,n);
rhoG = 15*ones(1,n);

Fv = 1;      %Tuning parameter
A=1.2;      %Profile parameter
B=0.3;      %Tuning parameter
aa1=0.2;    %Tuning parameter for transition from bubble flow regime
aa2=0.4;    %Tuning parameter for transition from bubble flow regime

%%%%%%%%%%%%%%%%%%%%%%%%%%%%%%%%%%%%%%%%%%%%%%%%%%%%%%%%%%%%%%%%%%%%%%%%
% 3x Varying Parameters %
%%%%%%%%%%%%%%%%%%%%%%%%%%%%%%%%%%%%%%%%%%%%%%%%%%%%%%%%%%%%%%%%%%%%%%%%

Fv_var= [0.8 1 1.2];
A_var = [1 1.2 1.3];
B_var = [0.1 0.3 0.66];
aa1_var = [0.1 0.2 0.3];
aa2_var = [0.3 0.4 0.5];

%%%%%%%%%%%%%%%%%%%%%%%%%%%%%%%%%%%%%%%%%%%%%%%%%%%%%%%%%%%%%%%%%%%%%%%%

for i = 1:length(Fv_var)
    legFv{i} = sprintf('F_v = %0.2g',Fv_var(i));
    legA{i} = sprintf('A = %0.2g',A_var(i));
    legB{i} = sprintf('B = %0.2g',B_var(i));
    legaa1{i} = sprintf('a_1 = %0.2g',aa1_var(i));
    legaa2{i} = sprintf('a_2 = %0.2g',aa2_var(i));
end
ind = 1:length(Fv_var);

c1_Fv = zeros(3,n);
c2_Fv = zeros(3,n);

```

```

c1_A = zeros(3,n);
c2_A = zeros(3,n);
c1_B = zeros(3,n);
c2_B = zeros(3,n);
c1_aa1 = zeros(3,n);
c2_aa1 = zeros(3,n);
c1_aa2 = zeros(3,n);
c2_aa2 = zeros(3,n);

Kalphag_Fv = zeros(3,n);
Kalphag_A = zeros(3,n);
Kalphag_B = zeros(3,n);
Kalphag_aa1 = zeros(3,n);
Kalphag_aa2 = zeros(3,n);

for (i = 1:3)

    [c1,c2,Kalphag] = SHIslip2_sens(alpG,Vm_pre,diam,rhoL,rhoG,Fv_var(i),A,B,aa1,aa2);
    c1_Fv(i,:) = c1;
    c2_Fv(i,:) = c2;
    Kalphag_Fv(i,:) = Kalphag;

    [c1,c2,Kalphag] = SHIslip2_sens(alpG,Vm_pre,diam,rhoL,rhoG,Fv,A_var(i),B,aa1,aa2);
    c1_A(i,:) = c1;
    c2_A(i,:) = c2;
    Kalphag_A(i,:) = Kalphag;

    [c1,c2,Kalphag] = SHIslip2_sens(alpG,Vm_pre,diam,rhoL,rhoG,Fv,A,B_var(i),aa1,aa2);
    c1_B(i,:) = c1;
    c2_B(i,:) = c2;
    Kalphag_B(i,:) = Kalphag;

    [c1,c2,Kalphag] = SHIslip2_sens(alpG,Vm_pre,diam,rhoL,rhoG,Fv,A,B,aa1_var(i),aa2);
    c1_aa1(i,:) = c1;
    c2_aa1(i,:) = c2;
    Kalphag_aa1(i,:) = Kalphag;

    [c1,c2,Kalphag] = SHIslip2_sens(alpG,Vm_pre,diam,rhoL,rhoG,Fv,A,B,aa1,aa2_var(i));
    c1_aa2(i,:) = c1;
    c2_aa2(i,:) = c2;
    Kalphag_aa2(i,:) = Kalphag;
end

%%%%%%%%%%
% PLOTS %
%%%%%%%%%%

```



```
clf
subplot(4,2,1)
plot(alpG,c1_Fv)
title('Concentration Profile vs. Gas Volume Fraction')
axis([0 1 1 1.25])
ylabel('Co', 'Rotation', 0)
xlabel('\alpha_{g}')
legend(legFv{ind})

subplot(4,2,2)
plot(alpG,c2_Fv)
title('Drift Velocity vs. Gas Volume Fraction')
ylabel('Vd [m/s]')
xlabel('\alpha_{g}')
legend(legFv{ind})

subplot(4,2,3)
plot(alpG,c1_A)
title('Concentration Profile vs. Gas Volume Fraction')
axis([0 1 1 1.35])
ylabel('Co', 'Rotation', 0)
xlabel('\alpha_{g}')
legend(legA{ind})

subplot(4,2,4)
plot(alpG,c2_A)
title('Drift Velocity vs. Gas Volume Fraction')
ylabel('Vd [m/s]')
xlabel('\alpha_{g}')
legend(legA{ind})

subplot(4,2,5)
plot(alpG,c1_B)
title('Concentration Profile vs. Gas Volume Fraction')
axis([0 1 1 1.25])
ylabel('Co', 'Rotation', 0)
xlabel('\alpha_{g}')
legend(legB{ind})

subplot(4,2,6)
plot(alpG,c2_B)
title('Drift Velocity vs. Gas Volume Fraction')
ylabel('Vd [m/s]')
xlabel('\alpha_{g}')
legend(legB{ind})
```

```

subplot(4,2,7)
plot(alpG,c2_aa1)
title('Drift Velocity vs. Gas Volume Fraction')
ylabel('Vd [m/s]')
xlabel('\alpha_{g}')
legend(legaa1{ind})

subplot(4,2,8)
plot(alpG,c2_aa2)
title('Drift Velocity vs. Gas Volume Fraction')
ylabel('Vd [m/s]')
xlabel('\alpha_{g}')
legend(legaa2{ind})

```

A.9 SHIslip2_sens.m

```

function [c1,c2,vg] = SHIslip2_sens(alpG,Vm_pre,diam,rhoL,rhoG,Fv,A,B,aa1,aa2)
%Slip parameters defined in SPE 84228
%Outputs c1 and c2 to be used in classical slip definition
% vG=c1*Vm+c2

%%%%%%%%%%%%%%%%%%%%%%%%%%%%%%%%%%%%%%%%%%%%%%%%%%%%%%%%%%%%%%%%%%%%%%%%
% Tuning Parameters %
%%%%%%%%%%%%%%%%%%%%%%%%%%%%%%%%%%%%%%%%%%%%%%%%%%%%%%%%%%%%%%%%%%%%%%%%

grav=9.81; %Gravitational constant
sigmagl=0.072; %Interfacial tension gas and liquid [N/m]

%%%%%%%%%%%%%%%%%%%%%%%%%%%%%%%%%%%%%%%%%%%%%%%%%%%%%%%%%%%%%%%%%%%%%%%%
% Start Program %
%%%%%%%%%%%%%%%%%%%%%%%%%%%%%%%%%%%%%%%%%%%%%%%%%%%%%%%%%%%%%%%%%%%%%%%%

n = length(alpG);

Vc = zeros(1,n);
Ddim = zeros(1,n);
Kud = zeros(1,n);
vGsf = zeros(1,n);
bcond1 = zeros(1,n);
bcond2 = zeros(1,n);
gam = zeros(1,n);
beta = zeros(1,n);
c1 = zeros(1,n);
c2 = zeros(1,n);

```

```

Kal = zeros(2,n);
Kalphag = zeros(1,n);
vg = zeros(1,n);

if B>=(2-A)/A,
    B=nan;
    fprintf('Stability criterion for B is not met')
end

Vc=(sigmagl*grav*(rhoL-rhoG)./(rhoL.^2)).^(1/4); %Characteristic velocity

Ddim_val=[2 4 10 14 20 28 50]; %table for determining critical kudeladze number
Kude=[0 1 2.1 2.5 2.8 3.0 3.2]; %table for determining critical kudeladze number

Ddim=sqrt((grav*(rhoL-rhoG)./sigmagl)*diam); %Dimensionless diameter

for i=1:length(alpG)

if Ddim(i)<2
    Kud(i)=0;
elseif 2<=Ddim(i) & Ddim(i)<=50
    Kud(i)=interp1(Ddim_val,Kude,Ddim(i)); %interpolation
else
    Kud(i)=3.2;
end

end

vGsf=Kud.*sqrt(rhoL./rhoG).*Vc; %Gas flooding velocity

bcond1 = Fv*alpG.*abs(Vm_pre)./vGsf;
bcond2 = alpG;
beta=max(bcond1,bcond2);

gam=(beta-B)./(1-B);

for i=1:length(gam)

if gam(i)<0
    gam(i) = 0;
elseif gam(i)>1
    gam(i) = 1;
end

end

```

```

c1=A./(1+(A-1)*gam.^2); %Profile parameter used to describe slip

aa=[aa1 aa2];

for i=1:length(alpG)

if alpG(i)<=aa1
    Kalphag(i)=1.53./c1(i);

elseif aa1<alpG(i) & alpG(i)<aa2
    Kal1=[1.53./c1(i) Kud(i)];
    Kalphag(i)=interp1(aa,Kal1,alpG(i));

elseif alpG(i)>=aa2
    Kalphag(i)=Kud(i);

end

end

c2 = (1-alpG.*c1).*c1.*Kalphag.*Vc./(alpG.*c1.*sqrt(rhoG./rhoL)+1-alpG.*c1);
c2_diff = c1.*Kalphag.*Vc./(alpG.*c1.*sqrt(rhoG./rhoL)+1-alpG.*c1);

vg = c2./(1-alpG.*c1);
vg(1,n) = c2_diff(1,n);

```

A.10 p_u1_u2.m

```

clear
clc

rhoLo=1000; %kg/m3
plo=100000; %Pa
al=1000; %m/s
ag=316; %m/s

syms u1 u2

B=al^2*(rhoLo-(plo/al^2)-u1-u2*(ag/al)^2);
C=-u2*(ag*al)^2*(rhoLo-(plo/al^2));

p=(-B+sqrt(B^2-4*C))/2*10^-5; % [bar]

U1=linspace(960,1100,30);
n1 = length(U1);
U2=linspace(0,30,50);

```

```
n2 = length(U2);

[u1,u2]=meshgrid(U1,U2);

P=subs(p);

surf(u1,u2,P)
axis([U1(1) U1(n1) U2(1) U2(n2) 0 1500])
xlabel('u_1 [kg/m^3]')
ylabel('u_2 [kg/m^3]')
zlabel('p [bar]')
title('Pressure vs. Conservative Variables u_1 and u_2')
```